

## Probing the Molecular Hearts of Extreme Bipolar Planetary Nebulae with ALMA

PAULA MORAGA BAEZ,<sup>1</sup> JOEL H. KASTNER,<sup>2</sup> JESSE BUBLITZ,<sup>3</sup> JAVIER ALCOLEA,<sup>4</sup>  
MIGUEL SANTANDER-GARCIA,<sup>4</sup> THIERRY FORVEILLE,<sup>5</sup> PIERRE HILY-BLANT,<sup>5</sup> BRUCE BALICK,<sup>6</sup> AND  
RODOLFO MONTEZ, JR.<sup>7</sup>

<sup>1</sup>*School of Physics and Astronomy and Laboratory for Multiwavelength Astrophysics, Rochester Institute of Technology, Rochester, NY 14623, USA*

<sup>2</sup>*Chester F. Carlson Center for Imaging Science and Laboratory for Multiwavelength Astrophysics, Rochester Institute of Technology, 54 Lomb Memorial Drive, Rochester, NY 14623, USA*

<sup>3</sup>*Green Bank Observatory, Green Bank, WV, USA*

<sup>4</sup>*Observatorio Astronómico Nacional, C/ Alfonso XII 365, E-28014 Madrid, Spain*

<sup>5</sup>*Institut de Planetologie et d'Astrophysique de Grenoble, France*

<sup>6</sup>*Department of Astronomy, University of Washington, Seattle, WA 98195, USA*

<sup>7</sup>*Harvard-Smithsonian Center for Astrophysics, 60 Garden Street, Cambridge, MA 02138, USA*

### Abstract

We present results from a program of Atacama Large Millimeter Array (ALMA) 1.3 mm (Band 6) molecular line mapping of a sample of nearby, bipolar/pinched-waist, molecule-rich PNe (NGC 6302, Hubble 5, NGC 2440, NGC 6445, NGC 2899, and NGC 2818). Maps of <sup>12</sup>CO(2–1) and <sup>13</sup>CO(2–1) emission as well as emission lines of HCN, HNC, HCO<sup>+</sup>, CN, and CS – many of these detected in these PNe for the first time – reveal the molecular mass distributions, compositions, and velocity fields of the equatorial and, in some cases, polar regions of the sample PNe. In each case, the bulk of the molecular gas traces an expanding equatorial torus, with torus expansion velocities ranging from  $\sim 15$  to  $\sim 50$  km s<sup>−1</sup> and molecular masses from  $\sim 0.002$  to  $\sim 0.1 M_{\odot}$ . The inferred molecular torus dynamical ages, which span the range  $\sim 500$  yr (Hb 5) to  $\sim 11000$  yr (NGC 2818), provide support for a model wherein molecular torus ejection precedes bipolar lobe formation. Collectively, these ALMA survey results provide insight into the rapid structural evolution as well as the zones of irradiated molecular gas within bipolar PNe that are descended from relatively massive progenitors, likely residing in interacting binary systems, over  $\sim 10$  kyr of the post-AGB evolution of such systems.

*Keywords:* Planetary nebulae (1249), Stellar mass loss (1613), Circumstellar matter (241), Molecular gas (1073), Interferometry (808)

### 1. INTRODUCTION

The standard model of the formation of planetary nebulae (PNe) describes their origin in terms of asymptotic giant branch (AGB) stars that eject their dusty envelopes, which are then shaped and ionized by fast winds and UV radiation from their remnant hot cores (Kwok et al. 1978; Höfner & Olofsson 2018, and references therein). This process generates strong shocks, nominally producing dense quasi-spherical or ellipsoidal swept-up shells with rarified interior hot bubbles that are diffuse X-

ray emission sources (Kastner et al. 2012). A subset of PNe display bipolar or asymmetric geometries that are theorized to be formed by fast, collimated outflows or jets during post-AGB evolution (Balick & Frank 2002). The physical mechanisms that are responsible for these collimated PN outflows, and how collimated outflows interact with and shape the ejected AGB envelope, remain open problems. Models proposed to explain the origin of collimated outflows include outflow launching by a binary companion’s accretion disk (e.g., De Marco & Izzard 2017, and references therein) as well as common envelope (CE) binary evolution (García-Segura et al. 2018). Hybrid models, such as repeated close binary encounters leading to an Intermediate-Luminosity Optical Transient (ILOT) (Soker & Kashi 2012), have also been invoked for the formation of PNe that are too complex in shape to be explained by CE events or continuous collimated flows. A prime example of such an object is the extreme bipolar PN NGC 6302, whose array of outflows, covering a range of dynamical ages, cannot be accounted for by isotropic AGB mass loss followed by collimated but steady post-AGB mass ejection (Balick et al. 2023).

Many if not most “classical,” pinched-waist, butterfly or hourglass-shaped bipolar PNe, like NGC 6302, also harbor large masses of molecular gas. Indeed, the presence of bright near-IR  $\text{H}_2$  and mm-wave CO emission from these molecular gas reservoirs is among the defining features of bipolar PNe — which, furthermore, are likely the descendants of relatively massive ( $\gtrsim 2 M_\odot$ ) progenitor stars (Corradi & Schwarz 1995; Kastner et al. 1996; Huggins et al. 2005). These molecule-rich regions can be studied to probe the kinematics and chemistry of highly structured PNe. For decades, millimeter-wave CO emission lines have been used as probes of the molecular gas components of planetary nebulae (e.g., Huggins & Healy 1989). Measurements of  $^{12}\text{CO}$  and  $^{13}\text{CO}$  line intensities allow mass and optical depth measurements of the molecular gas (Cox et al. 1992; Huggins et al. 1996). Subsequent to the early single-dish CO surveys of PNe, single-dish mm-wave molecular line surveys detected  $\text{HCO}^+$ , HNC, HCN, CN, CS, and other molecules that serve as probes of molecular chemistry and irradiation (e.g., Huggins et al. 2000; Edwards & Ziurys 2013; Edwards et al. 2014; Bublitz et al. 2019; Schmidt et al. 2022). The molecular ions  $\text{HCO}^+$ ,  $\text{N}_2\text{H}^+$  and  $\text{CO}^+$  provide tracers of X-ray ionization and UV irradiation of the nebular material (Deguchi et al. 1990; Zhang et al. 2008; Bublitz et al. 2023), while the HNC/HCN ratio represents a potent yet underutilized diagnostic of incident UV flux (Bublitz et al. 2022).

Interferometric mm-wave molecular-line mapping observations of PNe, which have been fewer and farther between, facilitate studies of the kinematics and masses of their dense equatorial regions (e.g., Zweigle et al. 1997; Peretto et al. 2007; Dinh-V-Trung et al. 2008a; Santander-García et al. 2017; Kastner et al. 2024, 2025b), in addition to spatially resolving their molecular irradiation zones (Bublitz et al. 2023). In this work, we present new interferometric Atacama Large Millimeter Array (ALMA) Band 6 (1.3 mm) observations of a sample of a half-dozen objects that are representative of the class of molecule-rich, high-excitation, bipolar PNe: PN Hb 5 (hereafter Hubble 5), NGC 2440, NGC 6302, NGC 6445, NGC 2818, and NGC 2899. The aim of our survey is to better constrain and understand the progenitor star systems, shaping histories, and irradiation geometries of these PNe. The velocity-resolved line images (data cubes) allow the analysis of molecular chemistry and nebular kinematics, while mm-wave continuum imaging reveals high-density ionized gas within the PNe. The main goals of this ALMA molecular-line mapping survey of pinched-waist, bipolar PNe are twofold:

- (1) Use velocity-resolved mm-wave molecular line mapping to pinpoint the locations and study the

structures and kinematics of the regions of cold, dense molecular gas within high-excitation bipolar PNe, so as to investigate the structural evolution of bipolar PNe that are descended from relatively massive progenitor stars.

(2) Ascertain the effects of UV vs. X-ray irradiation from PN central stars on the composition and heating of PN molecular gas.

This paper presents the survey data and initial survey results, focusing on the molecular species and transitions detected, molecular morphology and its spatial relation to the nebula’s ionized gas, and the molecular gas kinematics and masses of the sample PNe. The paper is structured as follows. In §2, we describe the selection and characteristics of the target PN sample. In §3, we outline the ALMA Band 6 program observations. The resulting molecular line detections for our target PN sample are described in §4. In §5 and §6 we present dynamical age measurements and molecular mass estimates, respectively. We summarize our results and conclusions in §7.

## 2. SAMPLE: HIGH-EXCITATION, MOLECULE-RICH, BIPOLAR PNE

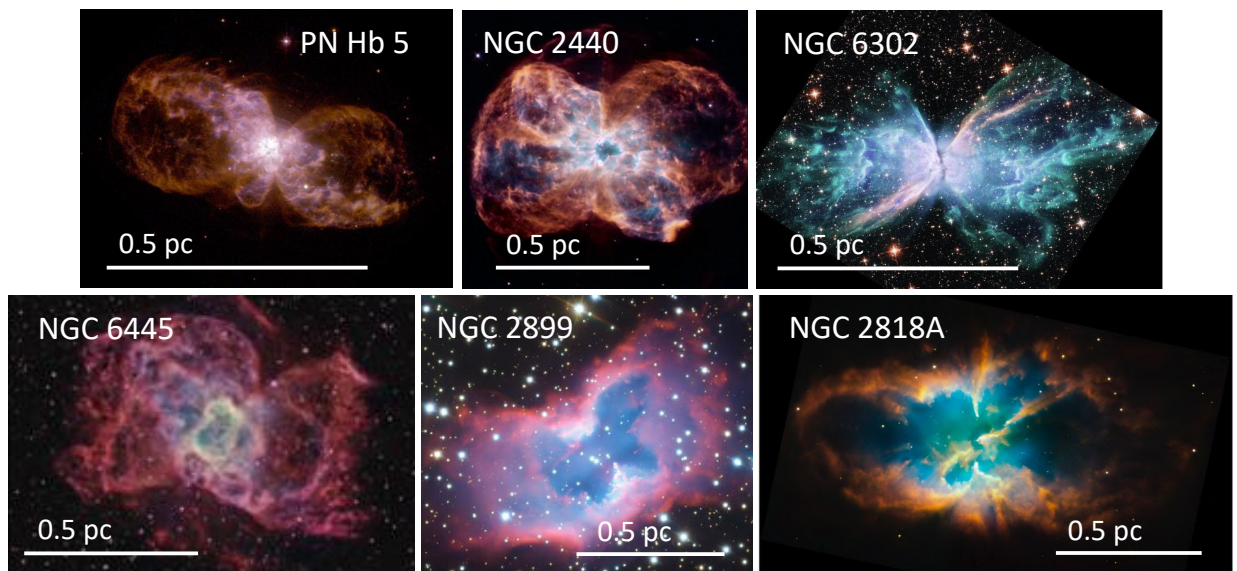


**Figure 1.** PNe observed in our ALMA Band 6 program. The fiducial 0.5 pc marker is based on the image field of view given the PN distances adopted here (see §2.7). The image of PN Hb 5 was obtained from a Dec. 17, 1997 NASA/ESA/Hubble press release; the image of NGC 6302 was obtained from June 18, 2020 NASA/ESA press release; the image of NGC 6445 was obtained from Fang et al. (2018); the image of NGC 2440 was obtained from a Feb. 13, 2007 NASA/ESA/STScI press release; the image of NGC 2818 was obtained from a Jan. 28, 2009 NASA/ESA and Hubble Heritage Team (STScI/AURA) press release; the image for NGC 2899 was obtained from a Jan. 15, 2021 ESO/VLT press release through Scientific American.

Figure 1 presents optical images of the six PNe included in our ALMA Band 6 molecular line mapping study. These objects were selected from catalogs of solar neighborhood PNe (e.g., Frew et al. 2016) on the basis of (a) particularly pronounced bi-lobed and pinch-waisted morphologies, (b) large masses of molecular gas, as evidenced by detections of bright near-IR H<sub>2</sub> (Kastner et al. 1996) and mm-wave CO (Huggins et al. 1996, 2005), (c) exceedingly hot central stars ( $T_{\text{eff}} \gtrsim 150$  kK), (d) large N abundances, and (e) literature distances of  $\lesssim 2$  kpc. Criteria (a)–(d) are indicative of progenitor stars of mass  $\gtrsim 2 M_{\odot}$  (Corradi & Schwarz 1995; Kastner et al. 1996; Karakas & Lugaro

2016; Henry et al. 2018), providing a sample with which to investigate the structural evolution of bipolar PNe descended from relatively massive progenitors. Among these PNe, only NGC 6302 had previously been observed interferometrically in the mm-wave regime (Peretto et al. 2007; Dinh-V-Trung et al. 2008a; Santander-García et al. 2017) prior to the ALMA observations presented here.

In the following, we summarize some important properties and characteristics of each of the sample PNe and their central stars, in approximate order of PN lobe dynamical ages.

### 2.1. *Hubble 5*

Hubble 5 (SIMBAD designation PN Hb 5) is characterized by two main, large lobes that stretch almost  $60''$  across the sky, with projected lobe expansion velocities of  $\sim 250 \text{ km s}^{-1}$  (Corradi & Schwarz 1993; Stanghellini et al. 2008; Ortiz et al. 2011; López et al. 2012). Additional, smaller lobes are also apparent in the central region of the nebula. In an Infrared Space Observation (ISO) far-IR spectral modeling study, the central star of Hubble 5 was found to have an intrinsic luminosity of  $6800 L_{\odot}$  and an effective temperature of  $\sim 170 \text{ kK}$ , suggesting a progenitor mass of  $> 4 M_{\odot}$  (Pottasch & Surendiranath 2007). Diffuse X-ray emission with a luminosity of  $0.04 L_{\odot}$  was detected in Hubble 5, indicative of the presence of strong shocks (Montez et al. 2009; Freeman et al. 2014). On the basis of morpho-kinematic modeling of Hubble 5, López et al. (2012) determined the PN to be  $\sim 1500$  yrs old and to contain  $0.0015 M_{\odot}$  of ionized gas. Steffen et al. (2013) used a hydrodynamical model to confirm that the model formulated by López et al. (2012) is indeed a plausible formation scenario for Hubble 5, and estimated the mass of its progenitor star as  $> 5 M_{\odot}$ .

Single-dish radio observations have detected  $^{12}\text{CO}$ , HCN, HNC,  $\text{HCO}^+$ , and CCH (Schmidt & Ziurys 2016, 2017a,b), indicating that Hubble 5 is C-rich. These molecular line studies yield an estimate of the  $\text{H}_2$  density within the central region of Hubble 5 of a few  $\times 10^5 \text{ cm}^{-3}$ .

### 2.2. *NGC 2440*

The morphology of NGC 2440 has been described as multi-polar, with its main, bubble-like ionized lobes oriented approximately E–W and a secondary pair of lobe structures oriented more nearly NE–SW (López et al. 1998, and references therein). Estimates of the effective temperature and luminosity of the central star of NGC 2440 obtained from modeling of nebular spectra (Miller et al. 2019, and references therein) range from  $\sim 170$  to  $\sim 210 \text{ kK}$  and  $\sim 500$  to  $\sim 3000 L_{\odot}$ , respectively. Miller et al. (2019) estimated progenitor and present-day central star masses of  $\sim 2.8 M_{\odot}$  and  $\sim 0.7 M_{\odot}$ , respectively; the latter is in good agreement with the estimate by Wolff et al. (2000).

Wang et al. (2008) obtained a single-dish map of  $^{12}\text{CO}(3-2)$  emission from the nebula that revealed CO within its core region as well as two knot-like structures located at the tips of the secondary lobes; these investigators estimated that the nebula contains a total molecular mass of  $\sim 0.01 M_{\odot}$ . Other molecules that have been detected near the core nebular region include  $^{13}\text{CO}$ ,  $\text{H}^{12}\text{CN}$ ,  $\text{H}^{13}\text{CN}$ , and  $\text{HCO}^+$  (Schmidt & Ziurys 2016; Ziurys et al. 2020). On the basis of HCN emission flux being much higher than that of  $\text{HCO}^+$  emission, Schmidt & Ziurys (2016) concluded that NGC 2440 is abundant N.

### 2.3. *NGC 6302*

Characterized by its bright and highly-excited bipolar lobes, NGC 6302 is known as the classic example of the class of bilobed, pinched-waist PNe (Aller et al. 1981). The bipolar lobes display velocities of  $\sim 600 \text{ km s}^{-1}$ , which indicate lobe dynamical ages of  $\sim 2000$  yrs (Meaburn et al. 2005,

2008; Szyszka et al. 2011). The nebular core is known to harbor one of the hottest central stars of any PN, with  $T_{eff}$  estimates ranging from 220–400 kK (Casassus et al. 2000; Wright et al. 2011; Ashley & Hyland 1988). Comparison of [N II] images obtained with WFC3 roughly a decade apart demonstrates that various structures and clumps within the lobes span a large range of dynamical ages, from  $\sim 300$ –2300 yr, indicating non-homologous expansion or perhaps multiple mass ejection events (Balick et al. 2023).

Within the dusty central torus of NGC 6302, C and O bearing molecules as well as PAHs, crystalline silicates, and H<sub>2</sub>O ice have been detected (Molster et al. 2001; Kemper et al. 2002; Santander-García et al. 2017). Emission from CO has been observed in NGC 6302 beginning in the late 1980s (Huggins & Healy 1989), and it is the only Fig. 1 object that has been the subject of interferometric mapping of CO (Peretto et al. 2007). Only recently, however, did ALMA CO mapping reveal the emission as tracing the nebula’s dense, dusty molecular torus and the inner lobe regions near the waist of the nebula (Santander-García et al. 2017). The equatorial torus shows slow expansion at  $\sim 8$  km s<sup>-1</sup>, indicating a dynamical age of  $\sim 5000$  – 7500 yrs (Peretto et al. 2007; Santander-García et al. 2017), much larger than the dynamical age range of the bipolar lobes.

#### 2.4. NGC 6445

NGC 6445 was first characterized by its bright elliptical center (Aller et al. 1973). Its faint lobes were later captured in deeper H $\alpha$  images, and H<sub>2</sub> emission was detected near its core, cementing its classification as a bipolar PN (Balick 1987; Schwarz et al. 1992; Kastner et al. 1996; Cuesta & Phillips 1999). van Hoof et al. (2000) conducted a UV and far-IR study and determined the effective temperature of the central star of the planetary nebula (CSPN) to be  $\sim 188$  kK, with a final mass of 0.625–0.696 M<sub>⊙</sub>, and a nebular dynamical age of approximately 3300 yrs if a distance of 1.5 kpc is assumed (Phillips & Mampaso 1988). NGC 6445 displays point-source X-ray emission at the position of the central star that may be due either to circumstellar shocks or coronal activity of a main-sequence companion (Montez et al. 2015).

Molecules were first detected in NGC 6445 by Huggins & Healy (1989) in their early survey of <sup>12</sup>CO(2–1) emission from PNe. Subsequently, <sup>13</sup>CO, OH, OH<sup>+</sup>, HCN, HNC, and HCO<sup>+</sup> have been detected in various single-dish line surveys (Aleman et al. 2014; Bublitz et al. 2019; Schmidt et al. 2022).

#### 2.5. NGC 2899

NGC 2899 rivals NGC 2818 as the most evolved PN in our ALMA survey, given its large angular extent ( $\sim 145''$ ). Although this nebula has been included in multiple surveys dating back five decades (Greig 1972; Bohuski & Smith 1974; Pottasch et al. 1984), there are few dedicated studies of the PN. NGC 2899 is characterized by its large, open bipolar lobes and filamentary structures that appear along its pinched-waist minor axis. Via long-slit echelle spectroscopy, the nebular ionized regions were found to have expansion velocities of  $\sim 50$  km s<sup>-1</sup>, with high-velocity structures reaching  $\sim 110$  – 130 km s<sup>-1</sup> (Lopez et al. 1991). The effective temperature of the CSPN is evidently extremely high, with literature estimates ranging between  $\sim 215$ –255 kK (Kaler & Jacoby 1989; Lopez et al. 1991; Drew et al. 2014). Thus, while the central star’s initial mass has been estimated as  $\sim 1.2$  M<sub>⊙</sub> (Kaler & Jacoby 1989), NGC 2899 is likely the product of a much more massive progenitor.

The new ALMA data presented here for NGC 2899 constitute the first mm-wave molecular line observations of the PN since its detection in CO by Huggins et al. (1996).

**Table 1.** ALMA TARGET DISTANCES

PN G	Name	BS2023 $D^a$ (kpc)	Lit. $D_{lower}$ (kpc)	Lit. $D_{upper}$ (kpc)	Adopted $D^b$ (kpc)	References <sup>c</sup>
359.3-00.9	PN Hb 5	$0.9^{+0.1}_{-0.1}$	1.7	2.0	$0.9^{+0.1}_{-0.1}$	SH10, S86
234.8+02.4	NGC 2440	$1.0^{+0.1}_{-0.1}$	0.8	2.2	$1.0^{+0.1}_{-0.1}$	G97, W08
349.5+01.0	NGC 6302	$0.5^{+0.1}_{-0.1}$	0.8	1.17	$1.0^{+0.1}_{-0.1}$	L19, M08
008.0+3.9	NGC 6445	$1.1^{+0.1}_{-0.1}$	1.4	1.5	$1.1^{+0.1}_{-0.1}$	S08, SH10
277.1-03.8	NGC 2899	$0.8^{+0.2}_{-0.2}$	0.9	1.4	$0.8^{+0.2}_{-0.2}$	D82, R99
261.9+08.5	NGC 2818	$1.5^{+0.1}_{-0.1}$	3.1	4.2	$3.3^{+0.1}_{-0.1}$	P21, BJ21

NOTES: (a) Gaia DR3 statistically-calibrated distances from [Bucciarelli & Stanghellini \(2023\)](#). (b) Distances adopted for this work. (c) References for literature distances (columns Lit.  $D_{lower}$  and Lit.  $D_{upper}$ ): S08 ([Stanghellini et al. 2008](#)), SH10 ([Stanghellini & Haywood 2010](#)), G97 ([Gorny et al. 1997](#)), W08 ([Wang et al. 2008](#)), P21 ([Poggio et al. 2021](#)), BJ21 ([Bailer-Jones et al. 2021](#)), D82 ([Daub 1982](#)), R99 ([Rauch et al. 1999](#)), L19 ([Lago et al. 2019](#)), M08 ([Meaburn et al. 2008](#)), S86 ([Sabbadin 1986](#)).

## 2.6. NGC 2818A

NGC 2818A (hereafter NGC 2818) is highly unusual among PNe for its apparent association with an open cluster, which actually carries the official designation NGC 2818 ([Tifft et al. 1972](#); [Kohoutek et al. 1986](#); [Bonatto et al. 2008](#); [Rani et al. 2023](#); [Fragkou et al. 2025](#)). In  $H\alpha$ , the morphology of the PN NGC 2818 consists of two distinct lobes with a diameter of nearly  $110''$ , and what appears to be the remnants of a torus at its center. NGC 2818 is one of the more evolved PN in our target group, with kinematical age measurements ranging from 6500–12300 yr ([Vázquez 2012](#); [Derlopa et al. 2024](#)). The initial and present-day mass of the nebula’s central star have been estimated as  $\sim 2 M_{\odot}$  and  $\sim 0.6 M_{\odot}$ , respectively ([Dufour 1984](#); [Derlopa et al. 2024](#); [Fragkou et al. 2025](#)). Estimates of the central star temperature range from  $\sim 130$  kK ([Fragkou et al. 2025](#)) to  $\sim 160$  kK ([Vázquez 2012](#); [Mata et al. 2016](#)). A recent study of the 3D kinematics of the ionized lobes of NGC 2818 by [Derlopa et al. \(2024\)](#) indicates the lobes contain filamentary arms that are expanding at  $180 \text{ km s}^{-1}$ . Its central torus was modeled as an equatorial structure expanding at  $70 \text{ km s}^{-1}$  with an inclination angle of  $80\text{--}70$  deg with respect to the plane of the sky ([Derlopa et al. 2024](#)).

Like NGC 2899, the PN NGC 2818 was detected in the [Huggins et al. \(1996\)](#) single-dish CO survey but, prior to the ALMA mapping presented here, had not been the subject of subsequent mm-wave molecular line observations.

## 2.7. Distances to ALMA targets

The basis for the adopted distance to each ALMA Band 6 target PN is summarized in Table 1, with individual cases discussed below. As is apparent from the Table — and as is typical for PNe whose central stars lack Gaia parallaxes — previously derived distances vary widely for most of the sample objects. Recent analysis of Gaia Data Release 3 (DR3) data has yielded a distance scale based on a far larger set of calibrators ([Bucciarelli & Stanghellini 2023](#)), and provides revised distance estimates for all of our sample PNe. These Gaia DR3 statistically-calibrated distances — which are not to be confused with Gaia DR3 parallax distances to the PN central stars — are listed in Table 1 in column “BS2023  $D$ ”. We adopted these distances and distance uncertainties for all PNe except NGC 2818 and NGC 6302. Given that recent analyses have placed the association of NGC

2818 with the open cluster NGC 2818 on more solid footing (Rani et al. 2023; Fragkou et al. 2025), we follow Fragkou et al. (2025) and adopt the Gaia-DR3-based distance to the cluster, 3.3 kpc, as the distance to the PN. In the case of NGC 6302, the Bucciarelli & Stanghellini (2023) DR3-based distance calibration places this nebula at  $\sim 0.545$  kpc, a factor  $\sim 2$  closer than estimates based on detailed morpho-kinematic modeling (e.g., Meaburn et al. 2008; Lago et al. 2019; Gómez-Gordillo et al. 2020). Hence, instead of adopting the Bucciarelli & Stanghellini (2023) distance, we take the mean of these reliable literature distances. Although the Bucciarelli & Stanghellini (2023) distances to Hb 5 and NGC 6445 are also significantly smaller than the minimum literature distances, most of these previous literature estimates were obtained via pre-Gaia parallax-based statistical methods; we hence adopt the Bucciarelli & Stanghellini (2023) Gaia DR3 statistically-calibrated distances for these two PNe.

The distances adopted for purposes of the analysis in this paper are listed in column “Adopted  $D$ ” of Table 1.

### 3. OBSERVATIONS

Our ALMA Band 6 survey, conducted under ALMA programs 2021.1.00456.S, 2021.2.00004.S, and 2022.1.00401.S, used both the 12-meter telescope array and the Atacama Compact (7-meter telescope) Array (hereafter referred to as 12-m and ACA, respectively). We configured the 12-m and ACA spectrometers in a half-dozen spectral setups in the 220–270 GHz frequency range to target emission lines of CO, CN, HCN, HNC, HCO<sup>+</sup>, CO<sup>+</sup>, CS, SO, and isotopologues of CO, HCN, and HCO<sup>+</sup> in the sample PNe. Details of the science goal (spectrometer) setups, including targeted emission lines, velocity resolution, and bandwidths, are listed in Table 2. The combination of 12-m array and ACA observations facilitates mapping of molecular gas structures over a wide range of nebular angular size scales and, in some cases, confirms the detection of weak emission lines that appear only in finer structures (resolved with the 12-m array) or extended, diffuse structures (mapped with ACA). Array configurations used in this work are Band 6 ACA (angular resolution of 5.45”), Band 6 12-m C43-1 (1.47”), Band 6 12-m C43-3 (0.62”), and Band 6 12-m C43-4 (0.40”) (see ALMA Cycle 11 Technical Handbook; Cortes 2024). The velocity resolution for each spectral window ranges from 0.163 to 1.40 km s<sup>-1</sup> for the targeted emission lines.

A total of 43 observations were made using these ACA, C43-1, C43-3, and C43-4 configurations. Integration times varied between  $\sim 5$ –46 minutes depending on the configuration that was being used, with ACA and 12-m configurations of typical duration  $\geq 19$  minutes and  $\leq 12$  minutes, respectively. Table 3 lists details of the ALMA arrays and data processing, including the acquisition dates, number of antennas, time elapsed during observations, baselines for each configuration, angular resolution, maximum recoverable scale (MRS), and phase and flux calibrators.

Data presented and analyzed here were obtained directly from the ALMA pipeline, run with the Common Astronomy Software Applications (CASA)<sup>1</sup> package version 6.2.1.7 for programs 2021.1.00456.S and 2021.2.00004.S, and CASA version 6.4.1.12 for program 2022.1.00401.S. Cleaning was performed with `tclean` using a Briggs-tapered weighting (`briggsbw taper`) for emission lines with

<sup>1</sup> CASA (<https://casa.nrao.edu/>) is the primary data processing software for the Atacama Large Millimeter/submillimeter Array (ALMA) and NSF’s Karl G. Jansky Very Large Array (VLA), and is also frequently used for other radio telescopes. CASA software can process data from both single-dish and aperture-synthesis telescopes, and one of its core functionalities is to support the data reduction and imaging pipelines for ALMA, VLA and the VLA Sky Survey (VLASS). CASA is being developed by an international team of scientists based at the National Radio Astronomical Observatory (NRAO), the European Southern Observatory (ESO), and the National Astronomical Observatory of Japan (NAOJ), under the guidance of NRAO. For more information see CASA Team et al. 2022

**Table 2.** ALMA BAND 6 SCIENCE GOAL SPECTROMETER SETUPS

Setup	Center Freq. (GHz)	Line Targets	Resolution (km s <sup>-1</sup> )	Bandwidth (MHz)
B6-1	213.000	Continuum	43.979	1875.00
	226.697	CN $N=2-1$ , $J=3/2-1/2$ , $F=3/2-1/2$	0.747	937.50
	226.874	CN $N=2-1$ , $J=5/2-3/2$ , $F=7/2-5/2$	0.747	937.50
	230.538	<sup>12</sup> CO $J=2-1$	0.734	937.50
	241.016	C <sup>34</sup> S $J=5-4$	1.400	1875.00
	244.936	CS $J=5-4$	1.382	1875.00
B6-2	250.500	Continuum	37.395	1875.00
	251.857	SO $3\Sigma N_J = 5_6 - 4_5$	0.672	468.75
	265.886	HCN $J=3-2$	0.550	937.50
	267.557	HCO <sup>+</sup> $J=3-2$	0.632	937.50
B6-3	256.302	H(29) $\alpha$	0.165	117.19
	259.011	H <sup>13</sup> CN $J=3-2$	0.163	117.19
	260.255	H <sup>13</sup> CO <sup>+</sup> $J=3-2$	0.163	117.19
	271.981	HNC $J=3-2$	0.622	937.50
B6-4	219.560	C <sup>18</sup> O $J=2-1$	0.771	468.75
	219.949	SO $3\Sigma N_J = 6_5 - 5_4$	0.769	468.75
	220.398	<sup>13</sup> CO $J=2-1$	0.768	937.50
	231.901	H(30) $\alpha$	0.730	937.50
	233.500	Continuum	40.118	1875.00
	235.789	CO <sup>+</sup> $J=2-1$ $F=3/2-1/2$	0.718	468.75

a 0.5 robust parameter. Briggs-weighting and a robust parameter of 0.5 were used for continuum images. The resulting molecular line spatial-spectral data cubes, spanning the full spectrometer bandwidths, were then processed via the ALMA Data Mining Toolkit (ADMIT)<sup>2</sup> software package to identify molecular emission lines and extract spatial-spectral data subcubes isolating the line emission, as well as to generate velocity-integrated (“moment 0”) as well as velocity-weighted (“moment 1”) emission-line images. In cases of non-detections of targeted lines (i.e., no detection during ADMIT processing), spectral windows were examined visually to verify that no emission is present above the noise, with the detected <sup>12</sup>CO(2–1) emission defining the velocity range over which to search for signal.

#### 4. RESULTS

Details of the detections and nondetections of molecular species and lines for each PN are listed in Table 4, including molecule names, frequencies, and the correlator setup to which the detection belongs. Tables listing molecular line detections, quantum numbers, Einstein coefficients, energy upper limits for their quantum states, and integrated line fluxes for individual PNe, as well as the PN systemic velocities ( $V_{LSR}$ ) and molecular line velocity half-widths at half-power ( $\Delta V_{1/2}$ ) obtained

<sup>2</sup> The ADMIT package products and usage guide are located at <https://admit.astro.umd.edu>.

**Table 3.** DETAILS OF BAND 6 OBSERVATIONS

Setup	Target	Date	Configuration	No. Ant.	Int. (min.)	Baselines (meters)	Res. ( $''$ )	MRS ( $''$ )	Phase Cal.	Flux Cal.
B6-1	PN Hb 5	Oct 25, 2022	12-m C43-1	43	5	14–312	1.47	12.4	J1820–2528	J1924–2914
		Dec 28, 2022	ACA	8	37	9–47	5.45	29.0	J1820–2528	J1617–5848
		Mar 19, 2023	12-m C43-4	36	12	15–918	0.40	4.89	J1820–2528	J1924–2914
	NGC 2440	Apr 03, 2022	ACA	10	19	8–44	5.45	29.0	J0730–1141	J0538–4405
		Jan 15, 2023	12-m C43-4	46	6	15–783	0.40	4.89	J0748–1639	J0750+1231
	NGC 6302	Aug 31, 2022	12-m C43-4	44	11	15–783	0.62	7.02	J1717–3342	J1617–5848
		Jan 01, 2023	ACA	9	19	8–48	5.45	29.0	J1717–3342	J1427–4206
	NGC 6445	Oct 25, 2022	12-m C43-1	43	5	14–312	1.47	12.4	J1820–2528	J1924–2914
		Dec 28, 2022	ACA	8	37	9–47	5.45	29.0	J1820–2528	J1617–5848
		Mar 19, 2023	12-m C43-4	36	12	15–918	0.40	4.89	J1820–2528	J1924–2914
	NGC 2899	Apr 24, 2022	ACA	10	42	8–44	5.45	29.0	J0940–6107	J1058+0133
		Jan 10, 2023	12-m C43-4	46	6	15–783	0.40	4.89	J0852–5755	J1058+0133
	NGC 2818	Mar 28, 2023	ACA	10	19	8–44	5.45	29.0	J0922–3959	J1058+0133
		Jan 15, 2023	12-m C43-4	46	6	15–783	0.40	4.89	J0922–3959	J0854+2006
B6-2	PN Hb 5	Jan 01, 2023	ACA	9	19	8–48	5.45	29.0	J1717–3342	J1517–2422
	NGC 2440	Dec 25, 2022	12-m C43-3	42	9	15–500	0.62	7.02	J0748–1639	J0750+1231
		Mar 23, 2023	ACA	9	19	8–44	5.45	29.0	J0730–1141	J0538–4405
	NGC 6302	Aug 29, 2022	12-m C43-3	43	11	15–783	0.40	4.89	J1717–3342	J1617–5848
		Jan 12, 2023	ACA	10	28	8–48	5.45	29.0	J1717–3342	J2258–2758
	NGC 2899	Apr 28, 2022	ACA	9	48	8–44	5.45	29.0	J0940–6107	J1058+0133
		Jan 07, 2023	12-m C43-3	43	11	15–650	0.62	7.02	J0852–5755	J1107–4449
	NGC 2818	Apr 22, 2022	ACA	10	28	8–44	5.45	29.0	J0922–3959	J0854+2006
		Dec 24, 2022	ACA	10	28	8–48	5.45	29.0	J0922–3959	J1058+0133
	Jan 10, 2023	12-m C43-3	46	9	15–783	0.62	7.02	J0922–3959	J1037–2934	
B6-3	PN Hb 5	Dec 29, 2022	12-m C43-3	36	9	15–500	0.62	7.02	J1744–3116	J1427–4206
	NGC 2440	Mar 23, 2022	ACA	9	19	8–44	5.45	29.0	J0730–1141	J0538–4405
		Dec 24, 2022	12-m C43-3	41	9	15–500	0.62	7.02	J0748–1639	J0750+1231
	NGC 6302	Aug 30, 2022	12-m C43-4	46	11	15–783	0.62	7.02	J1717–3342	J1517–2422
		Jan 01, 2023	ACA	9	28	8–48	5.45	29.0	J1717–3342	J1427–4206
	NGC 6445	Apr 07, 2023	ACA	10	28	8–47	5.45	29.0	J1733–1304	J1924–2914
	NGC 2899	Apr 14, 2022	ACA	10	40	8–44	5.45	29.0	J0940–6107	J1058+0133
		Jan 10, 2023	12-m C43-3	43	9	15–783	0.62	7.02	J0852–5755	J0519–4546
	NGC 2818	May 18, 2022	ACA	9	28	8–44	5.45	29.0	J0922–3959	J1058+0133
		Oct 15, 2022	12-m C43-3	44	11	14–500	0.62	7.02	J0922–3959	J1058+0133
Dec 23, 2022	ACA	11	28	8–48	5.45	29.0	J0922–3959	J0854+2006		
B6-4	NGC 2440	Mar 27, 2022	ACA	8	37	8–44	5.45	29.0	J0730–1141	J0854+2006
		Jan 18, 2023	12-m C43-3	43	34	15–782	0.62	4.89	J0730–1141	J0854+2006
	NGC 6302	Aug 30, 2022	12-m C43-3	46	32	15–783	0.40	4.89	J1717–3342	J1617–5848
		Oct 26, 2022	12-m C43-1	43	11	14–312	1.47	12.4	J1717–3342	J1924–2914
	NGC 2899	May 23, 2022	ACA	9	42	8–44	5.45	29.0	J0852–5755	J1058+0133
		Jan 11, 2023	12-m C43-4	45	26	15–783	0.40	4.89	J0852–5755	J1058+0133
	NGC 2818	Mar 29, 2022	ACA	10	46	8–44	5.45	29.0	J0922–3959	J1058+0133
		Jan 16, 2023	12-m C43-4	44	23	15–783	0.40	4.89	J0922–3959	J1058+0133

Table 4. BAND 6 OBSERVATIONS

ALMA Config.	Mol.	$\nu$ (GHz)	Flux <sup>a</sup> (Error <sup>b</sup> )					
			PN Hb 5 (Jy km s <sup>-1</sup> )	NGC 6302 (Jy km s <sup>-1</sup> )	NGC 2440 (Jy km s <sup>-1</sup> )	NGC 6445 (Jy km s <sup>-1</sup> )	NGC 2818 (Jy km s <sup>-1</sup> )	NGC 2899 (Jy km s <sup>-1</sup> )
ACA	<sup>12</sup> CO	230.538	359.078 (0.968)	799.576 (0.688)	92.957(0.872)	830.698 (0.931)	17.167 (0.728)	94.044 (0.925)
	<sup>13</sup> CO	220.398	–	–	44.230 (0.391)	–	<b>3.466 (0.404)</b>	<b>23.009 (0.284)</b>
	C <sup>18</sup> O	219.560	–	–	ND (0.037) <sup>c</sup>	–	ND (0.034) <sup>c</sup>	ND (0.035) <sup>c</sup>
	CO <sup>+</sup>	235.789	–	–	ND (0.072) <sup>c</sup>	–	ND (0.059) <sup>c</sup>	ND (0.051) <sup>c</sup>
	CN	226.697	<b>118.239 (0.789)</b>	<b>26.864 (0.976)</b>	<b>22.324 (0.933)</b>	<b>116.502(1.164)</b>	<b>2.375 (0.587)</b>	<b>8.063(0.409)</b>
		226.874	<b>279.184 (0.789)</b>	<b>79.536 (0.738)</b>	<b>57.088(0.739)</b>	<b>277.213 (0.977)</b>	<b>9.340(0.508)</b>	<b>24.294 (0.416)</b>
	CS	244.936	ND (0.070) <sup>c</sup>	<b>13.852 (0.866)</b>	–	ND (0.061) <sup>c</sup>	–	–
	C <sup>34</sup> S	241.016	–	<b>3.054 (0.667)</b>	–	–	–	–
	HCN	265.886	101.676 (1.030)	–	23.210 (0.629)	–	<b>2.883 (0.238)</b>	<b>9.799 (0.345)</b>
	H <sup>13</sup> CN	259.011	–	<b>15.319 (0.413)</b>	7.690 (0.656)	ND (0.097) <sup>c</sup>	ND (0.091) <sup>c</sup>	ND (0.088) <sup>c</sup>
	HNC	271.981	–	<b>24.116 (0.763)</b>	5.991 (0.606)	13.285 (0.819)	<b>0.949 (0.208)</b>	<b>2.457 (0.354)</b>
	HCO <sup>+</sup>	267.557	139.286 (1.419)	–	9.208 (0.923)	–	<b>0.492 (0.122)</b>	<b>1.836 (0.362)</b>
	H <sup>13</sup> CO <sup>+</sup>	260.255	–	<b>8.401 (0.434)</b>	ND (0.153) <sup>c</sup>	ND (0.143) <sup>c</sup>	ND (0.108) <sup>c</sup>	ND (0.139)
		251.857	ND (0.067) <sup>c</sup>	–	ND (0.028) <sup>c</sup>	–	ND (0.029) <sup>c</sup>	ND (0.067) <sup>c</sup>
	C43-1	<sup>12</sup> CO	230.538	517.688 (0.436)	–	–	982.035 (1.156)	–
<sup>13</sup> CO		220.398	–	286.858 (0.363)	–	–	–	–
C <sup>18</sup> O		219.560	–	<b>5.812 (0.104)</b>	–	–	–	–
CO <sup>+</sup>		235.789	–	ND (0.007) <sup>c</sup>	–	–	–	–
CN		226.697	<b>55.984 (0.843)</b>	–	–	<b>92.246 (0.675)</b>	–	–
		226.874	<b>114.224 (0.789)</b>	–	–	<b>222.366 (0.628)</b>	–	–
CS		244.936	ND (0.009) <sup>c</sup>	–	–	<b>5.982 (0.524)</b>	–	–
SO	219.949	–	6.344 (0.098)	–	–	–	–	
C43-3	<sup>13</sup> CO	220.398	–	–	9.762 (0.221)	–	–	–
	C <sup>18</sup> O	219.560	–	–	ND (0.003) <sup>c</sup>	–	–	–
	CO <sup>+</sup>	235.789	–	–	ND(0.004) <sup>c</sup>	–	–	–
	HCN	265.886	–	<b>97.244 (0.477)</b>	25.143 (0.296)	–	<b>1.962 (0.124)</b>	<b>9.658 (0.277)</b>
	H <sup>13</sup> CN	259.011	ND (0.029) <sup>c</sup>	<b>23.432 (0.500)</b>	8.268 (0.221)	–	ND (0.012) <sup>c</sup>	–
	HNC	271.981	ND (0.013) <sup>c</sup>	<b>19.634 (0.473)</b>	4.023 (0.303)	–	<b>2.446 (0.133)</b>	–
	HCO <sup>+</sup>	267.557	–	<b>140.005 (1.699)</b>	9.247 (0.503)	–	<b>0.778 (0.210)</b>	<b>2.049 (0.329)</b>
	H <sup>13</sup> CO <sup>+</sup>	260.255	<b>4.529 (0.050)</b>	<b>11.111 (0.847)</b>	<b>2.298 (0.196)</b>	–	ND (0.018) <sup>c</sup>	–
		251.857	–	1.702 (0.191)	ND (0.009) <sup>c</sup>	–	–	ND (0.005) <sup>c</sup>
C43-4	SO	219.949	–	4.556 (0.123)	<b>1.775 (0.169)</b>	–	–	–
	<sup>12</sup> CO	230.538	–	818.523 (0.389)	104.494 (0.537)	396.250 (3.156)	5.291 (0.244)	65.674 (0.326)
	<sup>13</sup> CO	220.398	–	262.820 (0.257)	–	–	<b>1.187 (0.101)</b>	<b>19.334 (0.215)</b>
	C <sup>18</sup> O	219.560	–	<b>2.545 (0.162)</b>	–	–	ND (0.002) <sup>c</sup>	ND (0.003) <sup>c</sup>
	CO <sup>+</sup>	235.789	–	ND (0.004) <sup>c</sup>	–	–	ND (0.004) <sup>c</sup>	ND (0.004) <sup>c</sup>
	CN	226.697	–	–	<b>20.843 (0.451)</b>	<b>43.218 (2.916)</b>	<b>0.667 (0.086)</b>	<b>5.878 (0.409)</b>
		226.874	–	–	<b>50.520 (0.480)</b>	<b>145.479 (2.978)</b>	<b>1.729 (0.113)</b>	<b>20.579 (0.618)</b>
	CS	244.936	–	–	ND (0.004) <sup>c</sup>	ND (0.040) <sup>c</sup>	<b>2.218 (0.282)</b>	ND (0.004) <sup>c</sup>
	SO	251.857	–	–	–	–	ND (0.004) <sup>c</sup>	–
		219.949	–	–	–	–	–	ND (0.003) <sup>c</sup>
H30 $\alpha$	231.901	–	<b>25.828 (0.235)</b>	–	–	–	–	

## NOTES:

a) Flux measurements are listed for all ALMA configurations in which data were obtained and the emission line was detected. Cases where configurations were not requested or observations in a given array configuration ran out of observation time are marked with ‘–’; flux measurements for new molecule detections are denoted by bold font.

b) Listed errors are obtained from image noise levels and do not include calibration uncertainties.

c) ‘ND’ indicates the line was observed but not detected; in parentheses are the root-mean-square values at the frequency of non-detected lines, reported in units Jy/beam.

from the ALMA data, are presented in Appendix A. Spatially integrated molecular line profiles are presented in Appendix B.

The integrated intensities of molecular lines detected in ALMA Band 6 ACA and 12-m configurations are compared in Fig. 2 to determine whether there is a loss of flux as the imaging resolution increases. Overall, the brighter molecular emission line sources (NGC 6302, NGC 6445, and NGC 2440) display little flux loss. On the other hand, there appears to be systematic flux loss in the 12-m configurations for the weaker, more fragmented molecular line sources, NGC 2818 and NGC 2899 (see §4.6 and §4.5, respectively). An exception is PN Hubble 5, where  $^{12}\text{CO}$  appears brighter in the 12-m configuration than the ACA configuration. This flux loss in the ACA observation is most likely an artifact of continuum subtraction errors that occurred during the pipeline image cleaning process, as is evident when comparing spectral profiles of  $^{12}\text{CO}$  for 12-m and ACA observations (see App. B), and is not observed when comparing other molecular lines observed for this nebula.

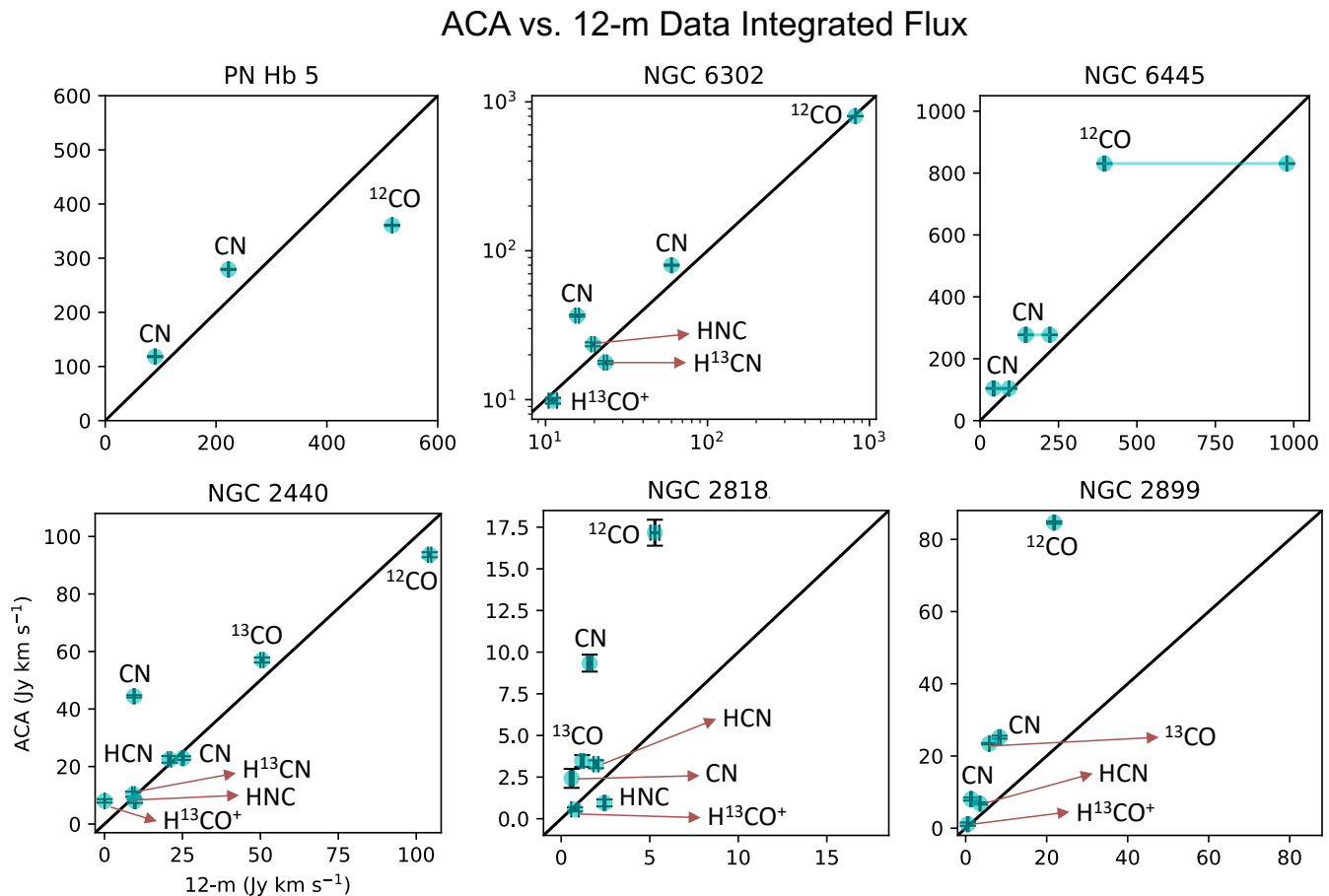


**Figure 2.** Comparison between the integrated fluxes measured with ACA and 12-m data for each molecular line for which observations were made in both ACA and 12-m configurations. Consistent flux measurements would follow along the black lines. The horizontal line in the plot for NGC 6445 indicates results from the C43-1 and C43-4 12-m configuration observations of  $^{12}\text{CO}(2-1)$  and CN hyperfine structure. Error bars were placed for all integrated flux measurements with calibration uncertainties included.

In Figure 3,  $^{12}\text{CO}$  zeroth moment images are overlaid on optical ( $\text{H}\alpha$  and  $[\text{N II}]$ ) emission-line imaging to reveal the location of the molecular gas with respect to the optical lobes for each PN. Each PN displays a distinct CO emission morphology; however, most of the detected emission is observed to arise from or near the central waist regions of each bipolar PNe, indicating that, as in the case of NGC 6302 (Santander-García et al. 2017), the bulk of the molecular gas observed in each case is tracing a central toroidal structure.

In the following subsections, we summarize the molecular transitions detected in each PN in order of inferred molecular torus dynamical age (§ 5), and we discuss in more detail how these ALMA Band 6 data reveal the structures of the dense waists of the survey PNe.

#### 4.1. *Hubble 5 (PN Hb 5)*

Figure 4 presents extractions from the 12-m  $^{12}\text{CO}(2-1)$  observation data cube for Hubble 5, including channel maps (top panels), zeroth moment image (bottom left), and spatially-integrated spectral line profile (bottom right). Detections in Hubble 5, presented in the form of moment 0 images (hereafter mom0) in Figure 5, include the  $J = 2 \rightarrow 1$  transition of  $^{12}\text{CO}$ ,  $N = 2 \rightarrow 1$  hyperfine transitions of CN ( $J = 5/2 \rightarrow 3/2$  and  $J = 3/2 \rightarrow 1/2$ ), and  $J = 3 \rightarrow 2$  transitions of HCN,  $\text{HCO}^+$ , and  $\text{H}^{13}\text{CO}^+$ . Emission from  $^{12}\text{CO}$  and CN was detected in both 12-m and ACA data. However, due to observing time limitations, HCN and  $\text{H}^{12}\text{CO}^+$  data were only obtained in the ACA observations, while  $\text{H}^{13}\text{CO}^+$  data were only obtained with the 12-m array. Fig 22 displays the spectral line profiles extracted for the detections obtained with each ALMA array.

In Fig. 5 (lower panels), the 12-m observations of  $^{12}\text{CO}$ , CN ( $5/2-3/2$ ), and CN ( $3/2-1/2$ ) emission reveal a  $10''$  structure oriented roughly north to south, with fainter extended “wings” that appear nearly orthogonal to this main N–S structure, running E to W. The brightest emission in the 12-m velocity channel maps (Fig. 4, upper panels) appears to trace an elliptical or toroidal structure that wraps around the nebula’s pinched waist. This main torus has a large projected expansion velocity,  $\sim 50 \text{ km s}^{-1}$  (see also Fig 22), while the fainter, extended “wing” structures are confined to smaller projected velocities of  $\sim 7 \text{ km s}^{-1}$ . The 12-m observations also reveal more extended  $^{12}\text{CO}$ , in the form of diffuse emission surrounding the molecular torus (see Fig. 5), that may trace the circular ring system detected in HST imaging of Hb 5. The ACA observations of Hubble 5, while yielding detections of HCN and  $\text{H}^{12}\text{CO}^+$  at the nebular core, offer little additional information regarding the morphology of the molecular emission region, due to the nebula’s compact nature (Fig. 5, upper panels).

Based on the color composite of ALMA and HST imaging (Fig. 3), the brightest  $^{12}\text{CO}$  emission indeed appears to be a nearly edge-on view of the torus. The southern region of the  $^{12}\text{CO}$  emission overlaps with a small optical emission lobe (relative to the main bipolar lobes) extending in that direction, while the extended “wings” detected in the  $^{12}\text{CO}$  and CN maps likely coincide with the front wall of the E optical lobe and the back wall of the W optical lobe, respectively. In the case of Hubble 5, the central torus traced by  $^{12}\text{CO}$  and CN molecular emission appears entirely intact as it wraps around the nebula’s axis of symmetry.

#### 4.2. *NGC 2440*

Channel maps, mom0 image, and spectral line profile extracted from the 12-m Band 6 observations of  $^{12}\text{CO}$  emission from NGC 2440 are presented in Fig. 6. The ACA observations of NGC 2440 yielded detections of  $^{12}\text{CO}$ ,  $^{13}\text{CO}$ , HNC, HCN,  $\text{H}^{13}\text{CN}$ ,  $\text{HCO}^+$ , and hyperfine transitions of CN (Fig. 7 and

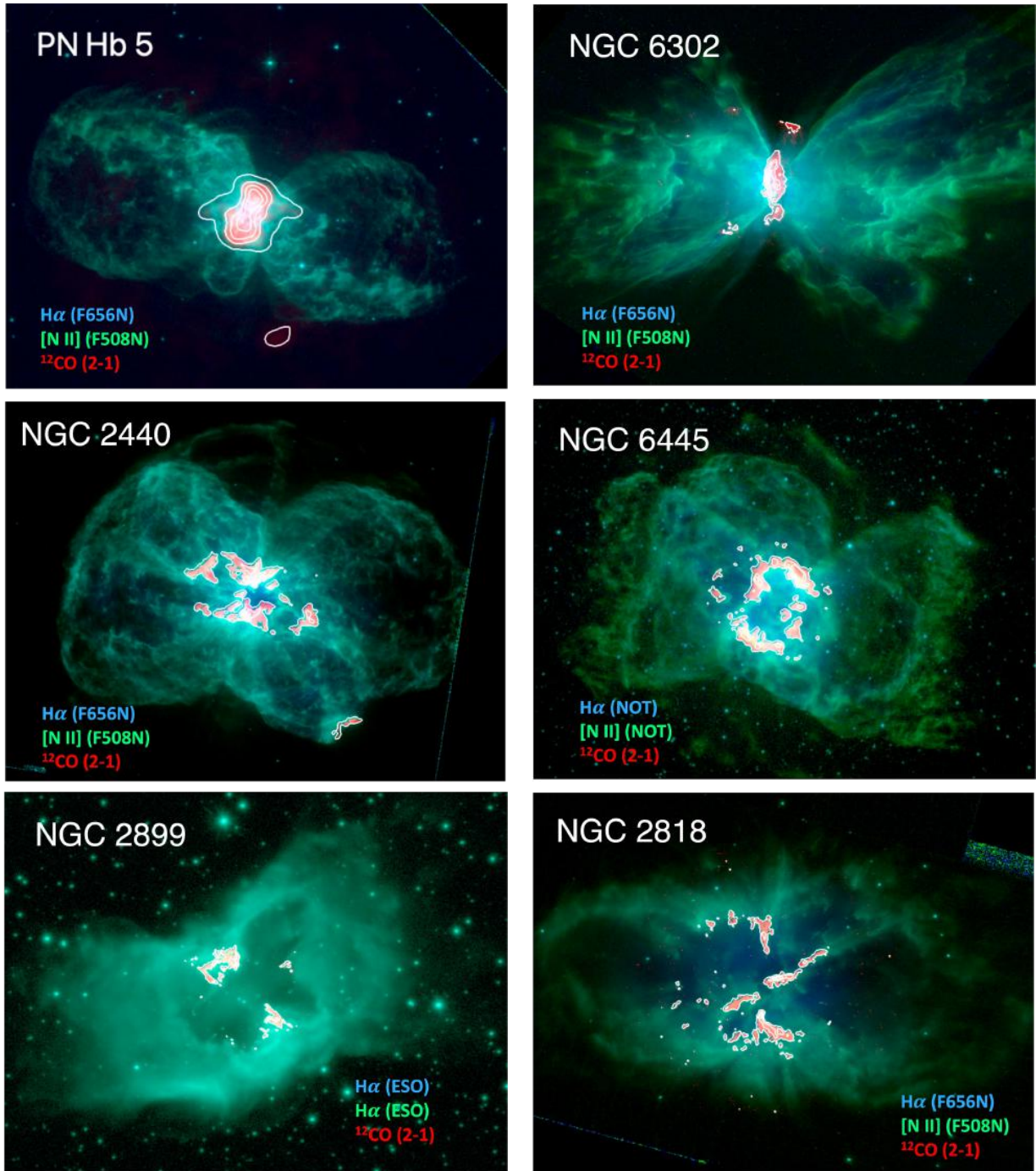


**Figure 3.** Color overlay images for all ALMA Band 6 targets.  $H\alpha$  (blue) and  $[N II]$  (green) images are overlaid with ALMA Band 6 12-m  $^{12}CO$  zeroth moment (red) images. White contours are present to show the full extent of  $^{12}CO$  emission with respect to optical emission lines.  $H\alpha$  and  $[N II]$  emission lines were observed with HST/WFPC2 for PN Hb 5, NGC 2440, and NGC 2818. These emission lines were observed with HST/WFC3 for NGC 6302, and NOT for NGC 6445. In the case of NGC 2899, only  $H\alpha$  ESO images (blue and green) are displayed.

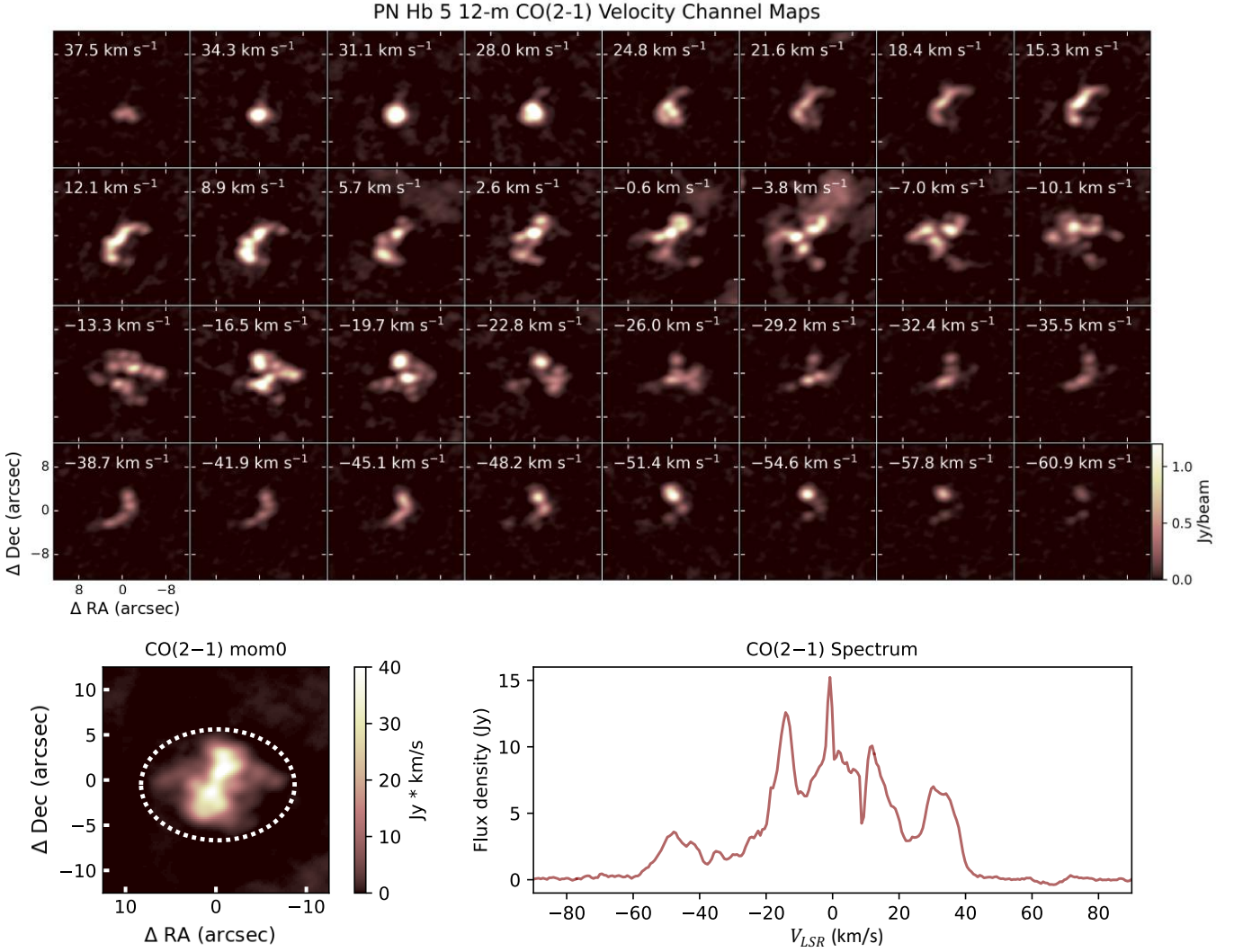


**Figure 4.** Images and spectrum extracted from 12-m  $^{12}\text{CO}(2-1)$  data cube obtained for Hubble 5. *Top panel:* PN Hb 5  $^{12}\text{CO}(2-1)$  emission in units Jy/beam across multiple velocity channels in increments of  $3.2 \text{ km s}^{-1}$ . *Bottom left panel:*  $^{12}\text{CO}(2-1)$  zeroth moment in units  $\text{Jy km s}^{-1}$  corresponding to the data cube displayed above. The white dotted oval surrounding the  $\text{CO}(2-1)$  emission represents the region selected for spectral data extraction from the same data cube. *Bottom right panel:* the resulting spatially integrated spectrum.

Fig. 23, left). The 12-m array observations yielded detections of these same transitions as well as  $\text{H}^{13}\text{CO}^+$  and SO (Figs. 8 and Fig. 23, right).

The ACA observations show bright molecular emission from the core region of NGC 2440, as well as two isolated knots of molecular emission offset by  $\sim 35''$  to the NE and SW from the bright core (Fig. 7). All three structures were previously detected in single-dish CO mapping by Wang et al. (2008). In our ACA data, the polar lobe knot structures are detected in  $^{12}\text{CO}$ ,  $^{13}\text{CO}$ , CN, and  $\text{HCO}^+$ , and appear faintly in HCN emission.

The 12-m observations were centered on the core region of NGC 2440, leaving the NE and SW knot structures just outside of the field of view (Fig. 6). In the 12-m array  $^{12}\text{CO}$  mom0 map, the core emission region of NGC 2440 is resolved into what appears to be a dense torus and molecular gas

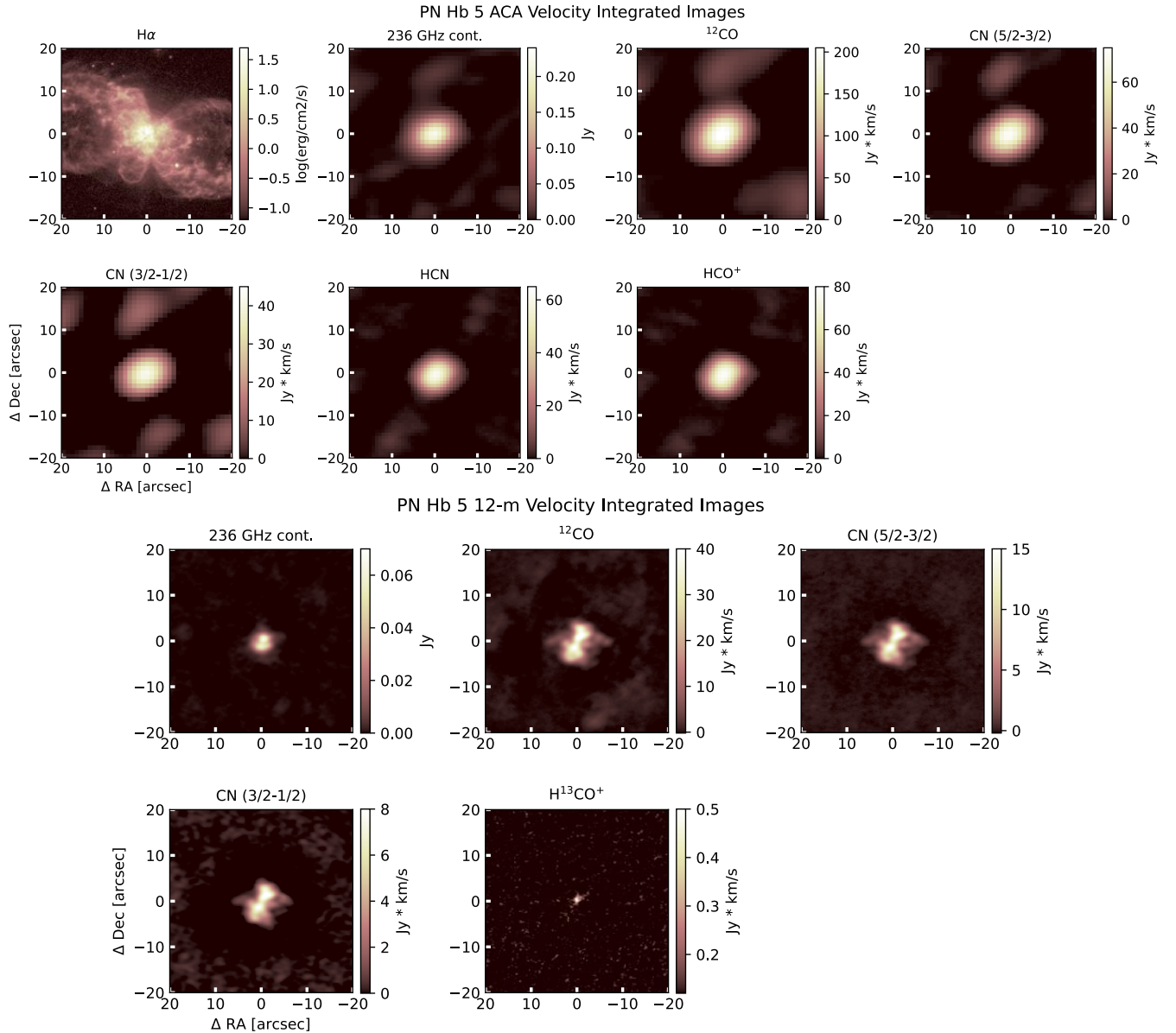


**Figure 5.** ALMA Band 6 mom0 images of emission lines detected in PN Hb 5 with the ACA array (top 7 panels) and 12-m (bottom 6 panels). *Top left panel:* archival HST/WFPC2 H $\alpha$  image. *Second panel from left:* ACA image of the continuum emission at 236 GHz as received from the ALMA pipeline. *Following 5 panels:*  $^{12}\text{CO}$ , CN (5/2–3/2), CN (3/2–1/2), HCN, and HCO $^+$  mom0 images, respectively. *Following 5 (12-m) panels:* 12-m array continuum emission at 236 GHz as received from the ALMA pipeline,  $^{12}\text{CO}$ , CN (5/2–3/2), CN (3/2–1/2), and H $^{13}\text{CO}^+$ , respectively. All images have a field of view of 40'' x 40''.

filaments that form a bi-lobed structure that is similar to, but larger than, that revealed in ALMA mapping of PN Hubble 5 (§ 4.1). The bi-lobed molecular gas structure, which is 20'' in extent, is oriented roughly E to W. The  $^{12}\text{CO}$  velocity channel maps and spectrum indicate that the W lobe is redshifted at velocities up to  $\sim 70 \text{ km s}^{-1}$  and the E lobe is blueshifted at velocities up to  $\sim 20 \text{ km s}^{-1}$ . Thus, the projected expansion velocity of the central molecular gas structure is  $\sim 25 \text{ km s}^{-1}$ .

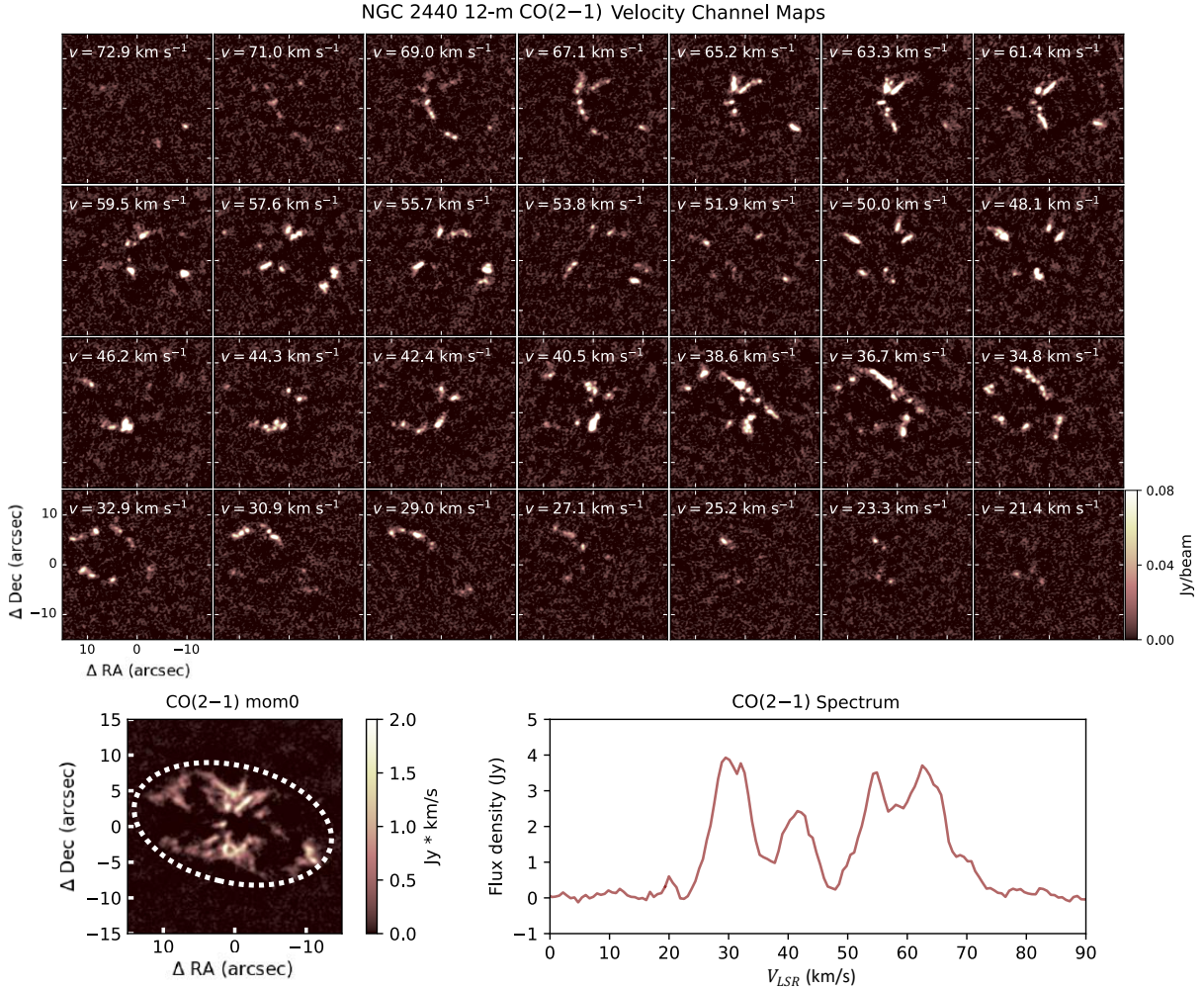


**Figure 6.** Same as Fig. 4, but displaying 12-m Band 6 data for NGC 2440. Velocity channels are displayed in increments of  $1.9 \text{ km s}^{-1}$ .

The projected relative expansion speed of the NE and SW knots obtained from the ACA channel maps (not shown), assuming these features constitute a pair, is  $\sim 14 \text{ km s}^{-1}$ . This indicates that the knots are moving nearly perpendicular to our line of sight. We note that these knot structures lie at the tips of two interior lobes of ionized gas oriented at  $\sim 45^\circ$  with respect to NGC 2440’s larger, E–W aligned lobe pair (Fig. 3). These structures hence could be clumps of progenitor AGB star ejecta that were shot out as projectiles along the NE–SW direction, before the central star was unveiled and the nebula became ionized; their ejection may have generated NGC 2440’s second, misaligned lobe pair.

#### 4.3. NGC 6302

Among the PNe included in our ALMA Band 6 survey, NGC 6302 has yielded the largest set of detections of molecular species, with high signal-to-noise measurements of almost all lines targeted. A notable exception is the nondetection of  $\text{CO}^+$ ; NGC 7027 remains the only PN in which this molecule has been detected thus far (Bublitz et al. 2023, and references therein). In our ACA observations of NGC 6302, the  $J = 2 \rightarrow 1$  transition of  $^{12}\text{CO}$ ,  $N = 2 \rightarrow 1$  hyperfine transitions of

## NGC 2440 ACA Velocity Integrated Images

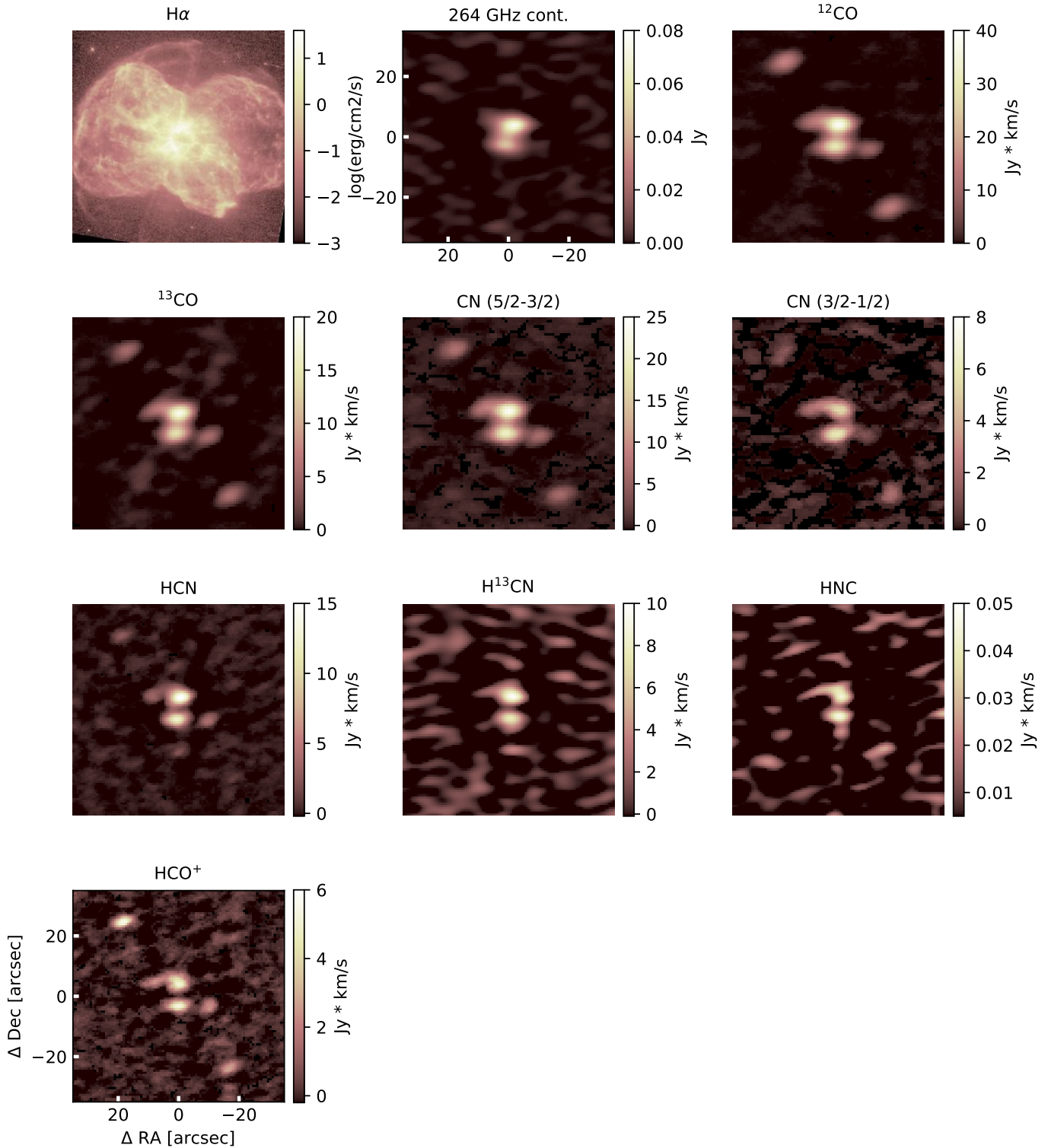


**Figure 7.** As in Fig. 5, but displaying ACA Band 6 mom0 images for NGC 2440. *Top left panel:* an archival HST/WFPC2 H $\alpha$  image of NGC 2440. *Second panel:* an image of the continuum emission at 264 GHz as received from the ALMA pipeline. *Following panels:* <sup>12</sup>CO, <sup>13</sup>CO, CN (5/2–3/2), and CN (3/2–1/2), HCN, H<sup>13</sup>CN, HNC, and HCO<sup>+</sup>, respectively. All images have a field of view of 70'' x 70''.

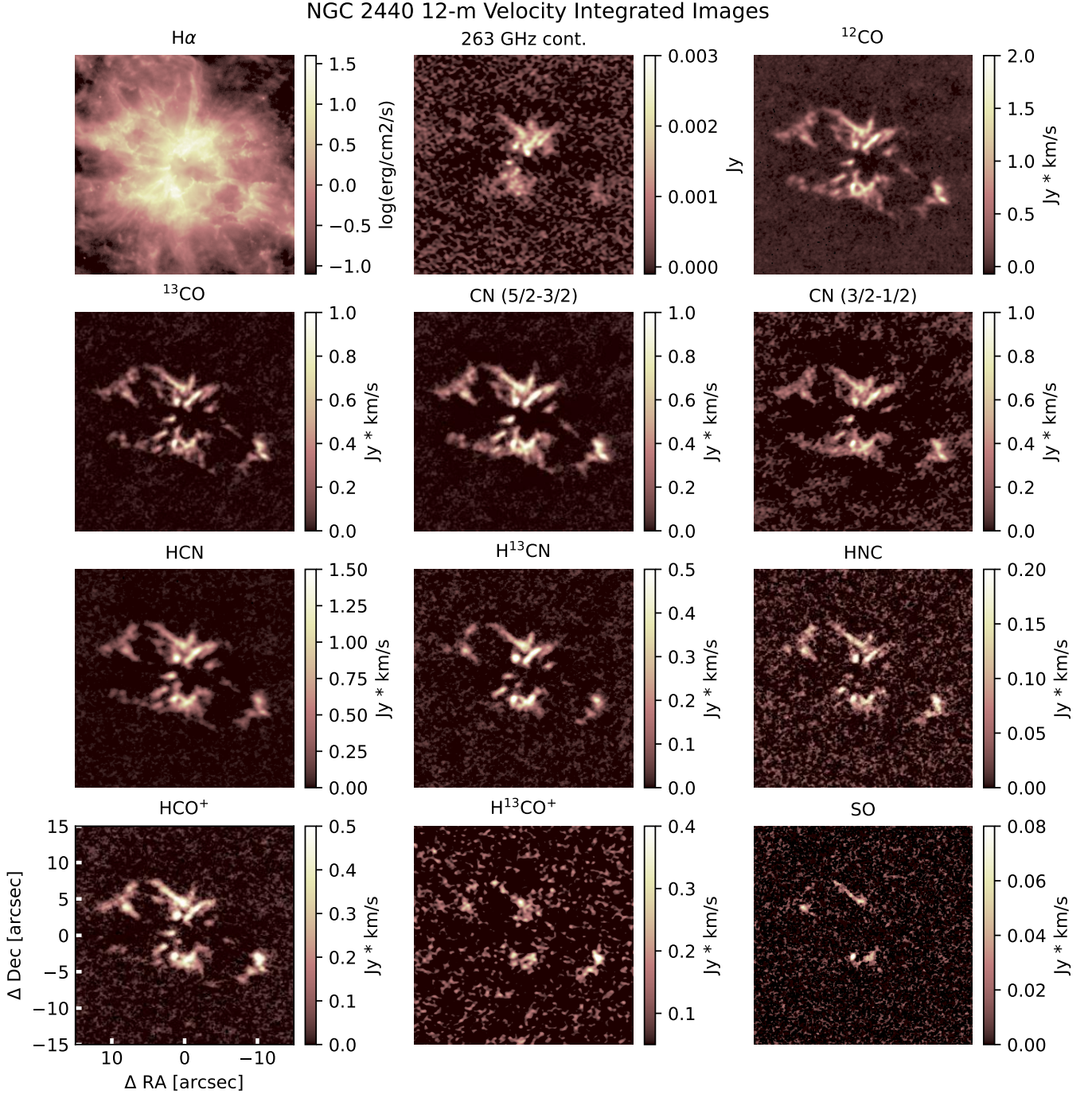


**Figure 8.** Same as Fig. 5, but displaying 12-m Band 6 mom0 images for NGC 2440. *Top left panel:* an archival HST/WFPC2 H $\alpha$  image of NGC 2440. *Second panel:* an image of the continuum emission at 263 GHz as received from the ALMA pipeline. *Following panels:*  $^{12}\text{CO}$ ,  $^{13}\text{CO}$ , CN (5/2-3/2), and CN (3/2-1/2), HCN, H $^{13}\text{CN}$ , HNC, HCO $^+$ , and SO 6(5)-5(4), respectively. All images have a field of view of 30'' x 30''.

CN,  $J = 3 \rightarrow 2$  transitions of HNC, H $^{13}\text{CN}$ , and H $^{13}\text{CO}^+$ , and  $J = 5 \rightarrow 4$  transitions of CS and C $^{34}\text{S}$  were all detected. Additional detections of the  $J = 2 \rightarrow 1$  transitions of  $^{13}\text{CO}$  and C $^{18}\text{O}$ ,  $J = 3 \rightarrow 2$

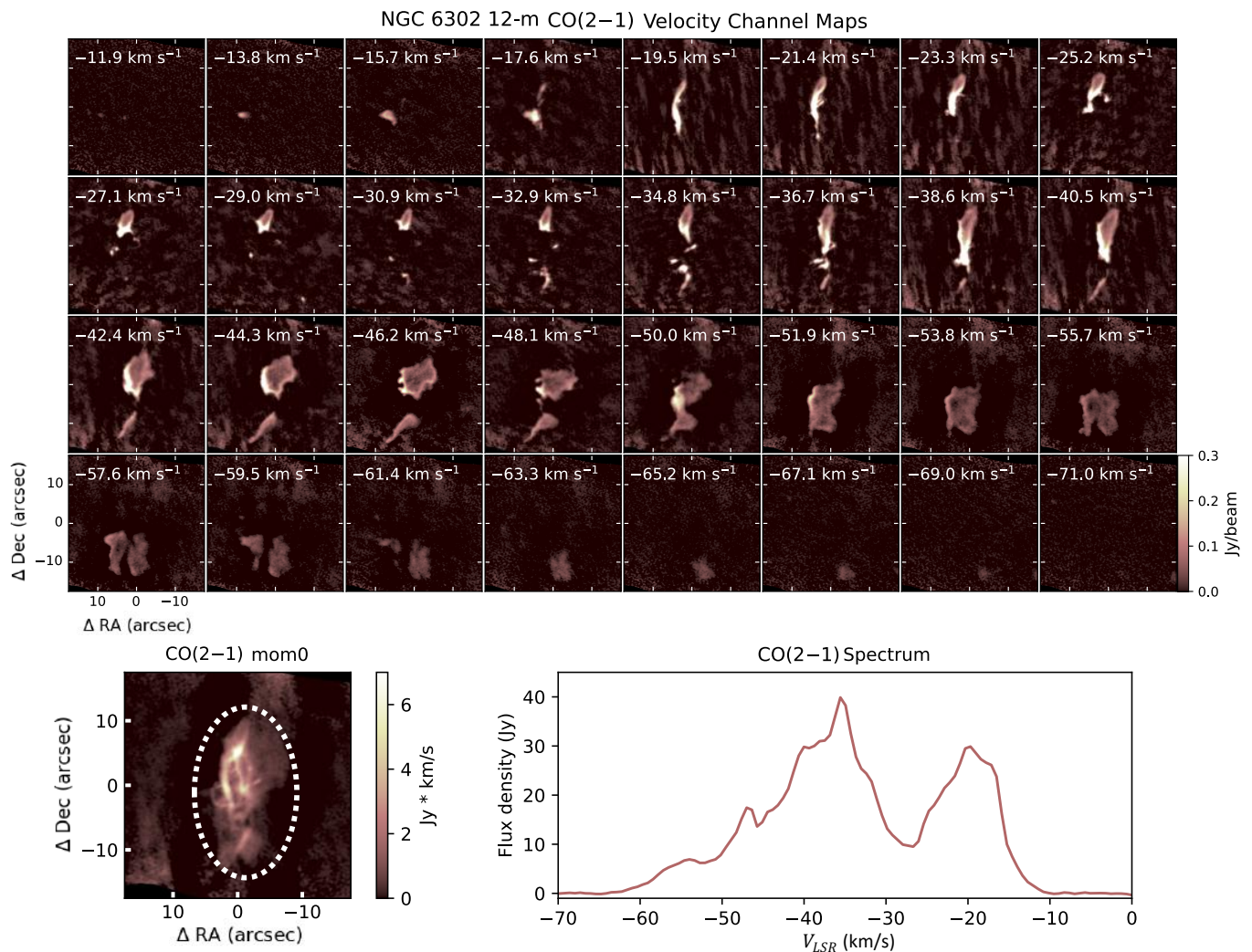


**Figure 9.** Overview of 12-m Band 6  $^{12}\text{CO}$  data for NGC 6302, presented as in Fig. 4. Velocity channels are displayed in increments of  $1.9 \text{ km s}^{-1}$ .

transitions of HCN and  $\text{HCO}^+$ ,  $N_J = 6_5 \rightarrow 5_4$  and  $N_J = 5_6 \rightarrow 4_5$  transitions of SO, and  $\text{H30}\alpha$  were obtained with the 12-m array. Channel maps, mom0 image, and spectral line profile extracted from the 12-m Band 6 observations of  $^{12}\text{CO}$  emission from NGC 6302 are presented in Fig. 9. The zeroth moment images obtained from the ACA and 12-m array data cubes are displayed in Fig. 10 and Fig. 11, respectively; spectral profiles obtained from these data cubes are presented in Fig. 24.

The 12-m data reveals the detailed morphology of the molecular gas that traces NGC 6302’s central region, demonstrating its complexity (Fig. 9). Along with a nearly edge-on toroidal structure tracing the dusty central waist of the nebula, the  $^{12}\text{CO}$  (2–1) emission traces a loop that extends to the east (denoted as structure ‘a’ in Fig. 11). Upon closer inspection of the  $^{12}\text{CO}$  velocity channel maps, however, it is clear that this latter structure is blue-shifted and stretches from the back edge of the central torus, looping around the front. These distinct kinematic structures were previously detected in ALMA  $^{12}\text{CO}$  (3–2) mapping of NGC 6302 obtained, at lower sensitivity, by Santander-García et al. (2017); they concluded that the CO traces two rings of molecular gas that are inclined approximately  $60^\circ$  to each other. Similar two-loop structures have been observed in velocity-resolved CO maps of

## NGC 6302 ACA Velocity Integrated Images

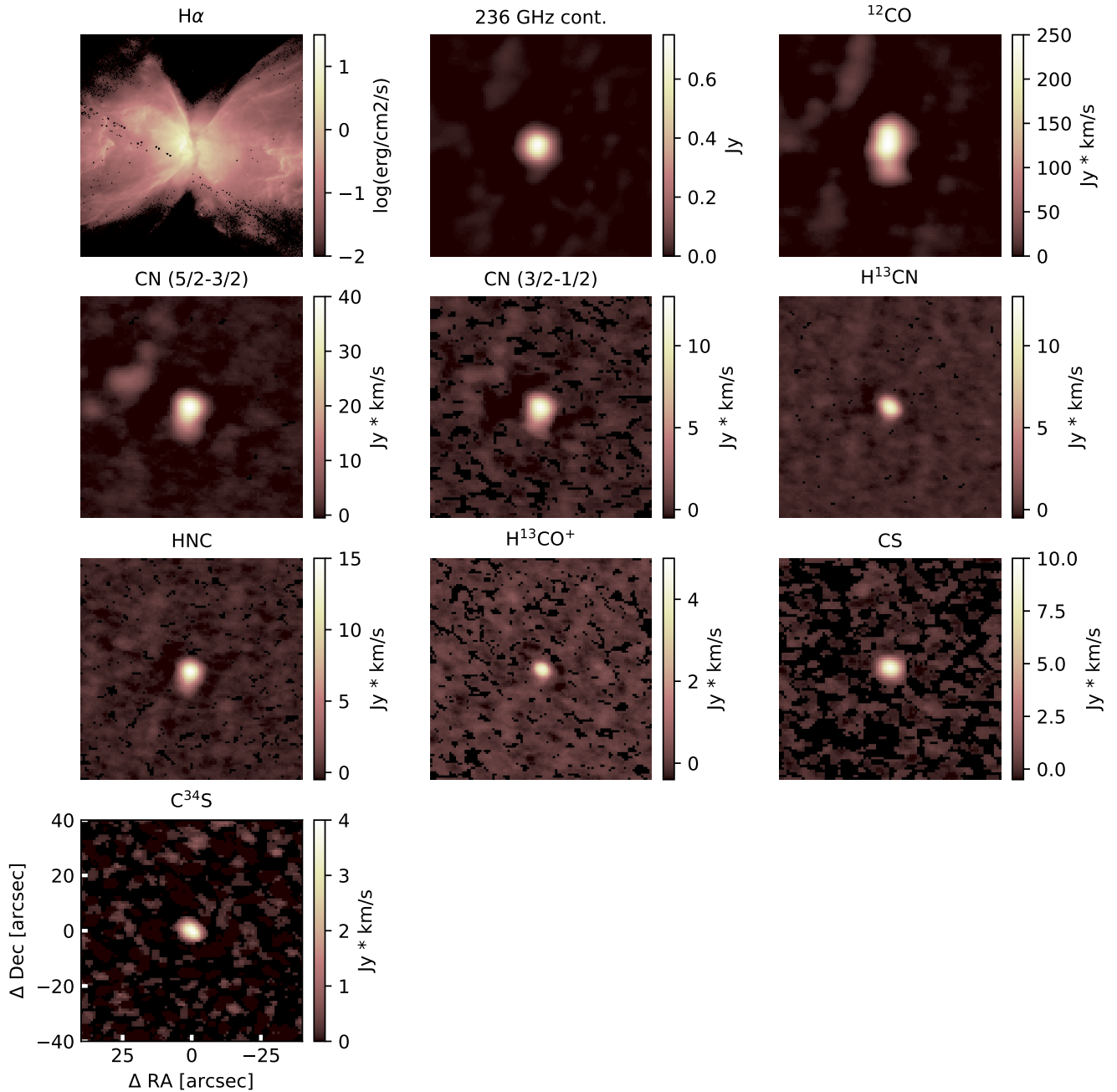


**Figure 10.** ACA Band 6 mom0 images for NGC 6302. *Top left panel:* an archival HST/WFC3 H $\alpha$ . *Second panel:* continuum emission at 236 GHz as received from the ALMA pipeline. *Following panels:*  $^{12}\text{CO}$ , CN (5/2-3/2), CN (3/2-1/2), H $^{13}\text{CN}$ , HNC, H $^{13}\text{CO}^+$ , CS, C $^{34}\text{S}$  respectively. All images have a field of view of 80'' x 80''.

the ring-like PNe NGC 7293 (Young et al. 1999), NGC 3132, and NGC 6720 (Kastner et al. 2024, 2025b).

## NGC 6302 12-m (C43-1) Velocity Integrated Images

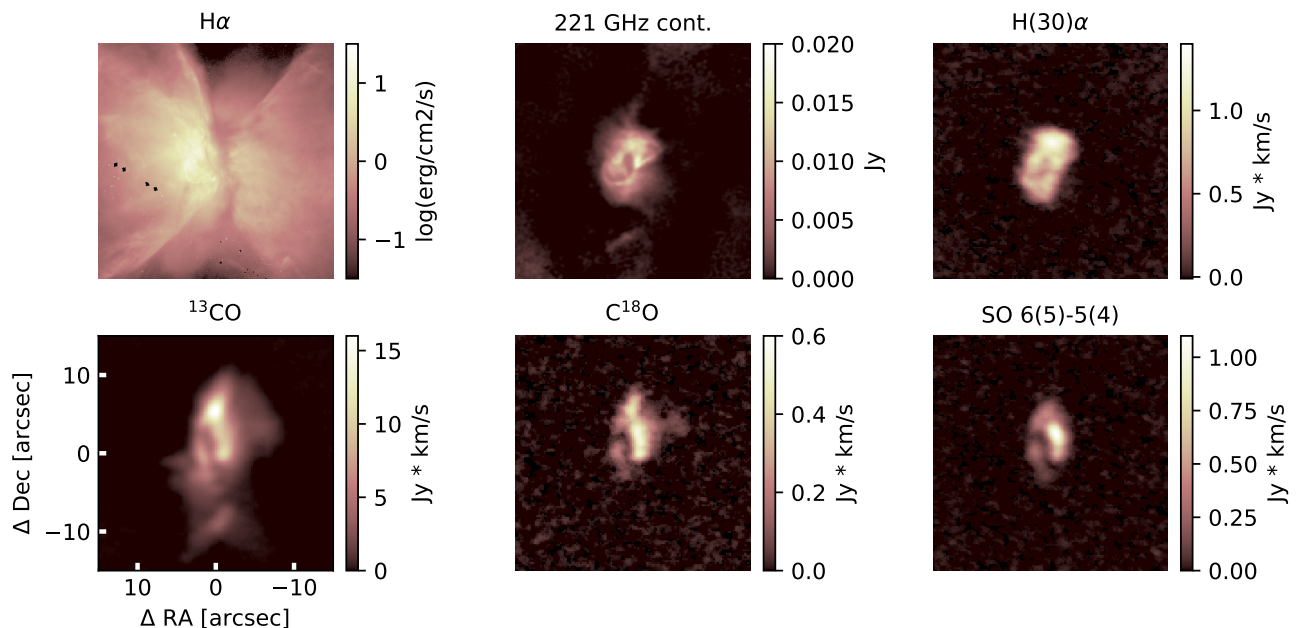


**Figure 11.** 12-m (C43-1) Band 6 mom0 images for NGC 6302. *Top left panel:* an archival HST/WFC3 H $\alpha$  image. *Second panel:* 12-m array C43-1 image of the continuum emission at 221 GHz as received from the ALMA pipeline. *Following panels:* H(30) $\alpha$ ,  $^{13}\text{CO}$ , C $^{18}\text{O}$ , and SO 6(5)–5(4). All images have a field of view of 30'' x 30''.

The same double-looped structure appears in the ALMA 12-m maps of CN, HCN, HNC, HCO $^+$  emission from NGC 6302, and is very also faintly present in  $^{13}\text{CO}$  and H $^{13}\text{CO}^+$  emission. However, the southern region of the central torus is faint in all other emission lines detected, leaving only the northern region visible. Several of the detected emission line maps exhibit a locally bright, thin structure (denoted as structure ‘b’ in Figure 11) that coincides with a local minimum in the  $^{12}\text{CO}$  emission line map. This local minimum is likely due to a particularly dense, cold clump of molecular gas causing self-absorption in  $^{12}\text{CO}$ ; this cold, dense gas likely sits in the foreground of the molecular torus, where it is shielded from direct UV radiation from the planetary nebula central star.

When comparing optical and radio emission-like morphologies of NGC 6302, the molecular gas is almost completely concentrated in the central torus of the nebula, closely tracing the dark lane observed in HST/WFC3 images (Fig. 3). However, a few compact knots of CO emission are detected within the east optical lobe of the nebula. These molecular knots are spatially closely in conjunction with dusty clumps seen in HST imaging of the polar lobes of NGC 6302 (Kastner et al. 2022). The molecular emission morphology seen in the ACA mom0 maps appears marginally extended N–S in  $^{12}\text{CO}$ , CN, and HCN emission, and appears round and possibly unresolved in all other emission lines (Figs. 10, 11); the emission detected by the ACA remains compact and close to the central torus, with no additional extended emission apparent from the lobe regions.

## 4.4. NGC 6445

Channel maps, mom0 image, and spectral line profile extracted from the 12-m Band 6 observations of  $^{12}\text{CO}$  emission from NGC 6445 are presented in Fig. 12. Other molecular line detections include

## NGC 6302 12-m (C43-4) Velocity Integrated Images

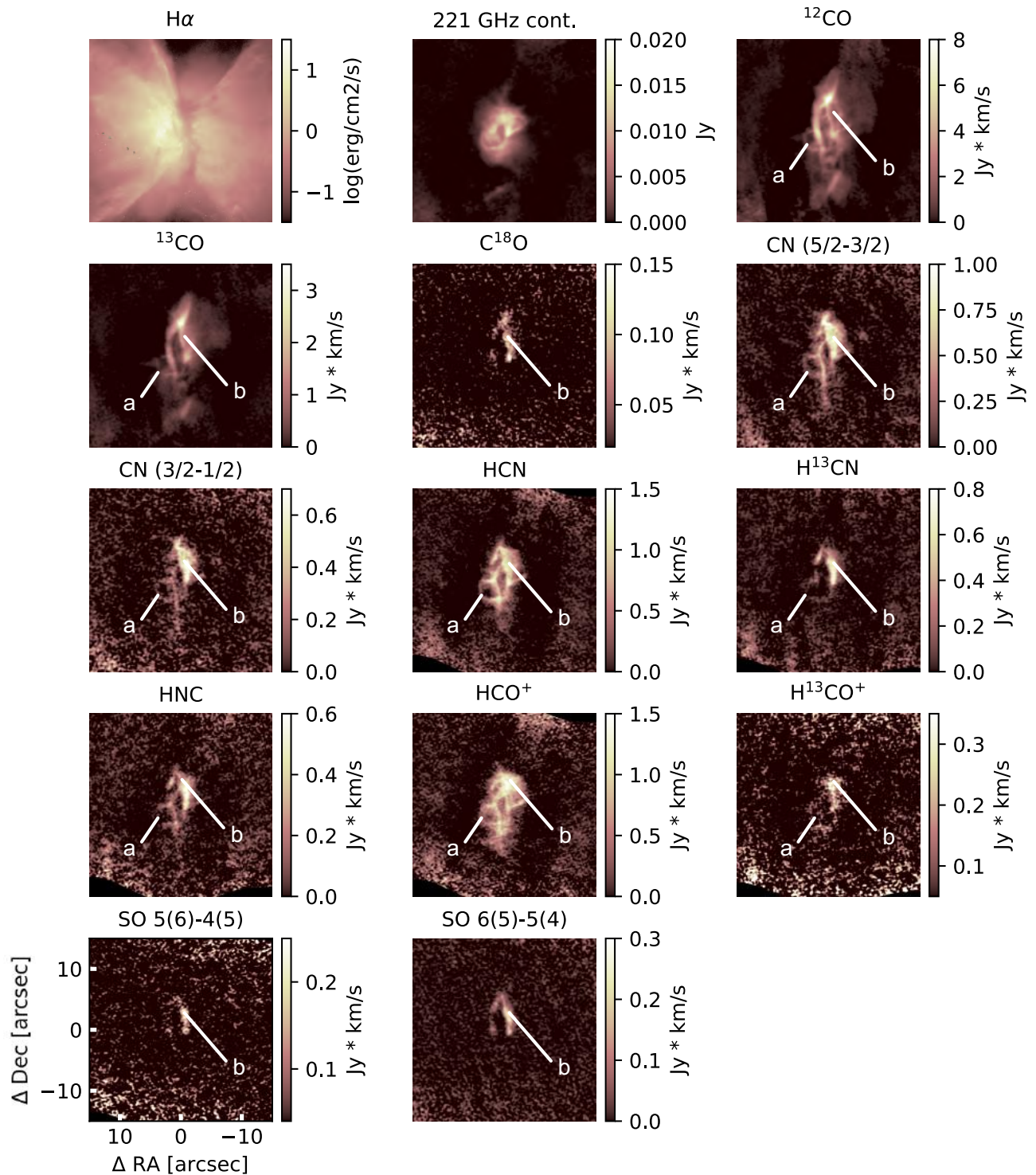


**Figure 11.** (cont.) 12-m (C43-4) Band 6 mom0 images for NGC 6302. *Top left panel:* an archival HST/WFC3 H $\alpha$  image. *Second panel:* continuum emission at 221 GHz as received from the ALMA pipeline. *Following panels:*  $^{12}\text{CO}$ ,  $^{13}\text{CO}$ ,  $\text{C}^{18}\text{O}$ , CN (5/2-3/2), CN (3/2-1/2), HCN,  $\text{H}^{13}\text{CN}$ , HNC,  $\text{HCO}^+$ ,  $\text{H}^{13}\text{CO}^+$ , SO 5(6)-4(5), and SO 6(5)-5(4). All images have a field of view of 30'' x 30''. Two important structures in the nebula, denoted by 'a' and 'b', are discussed in more detail in § 4.3.

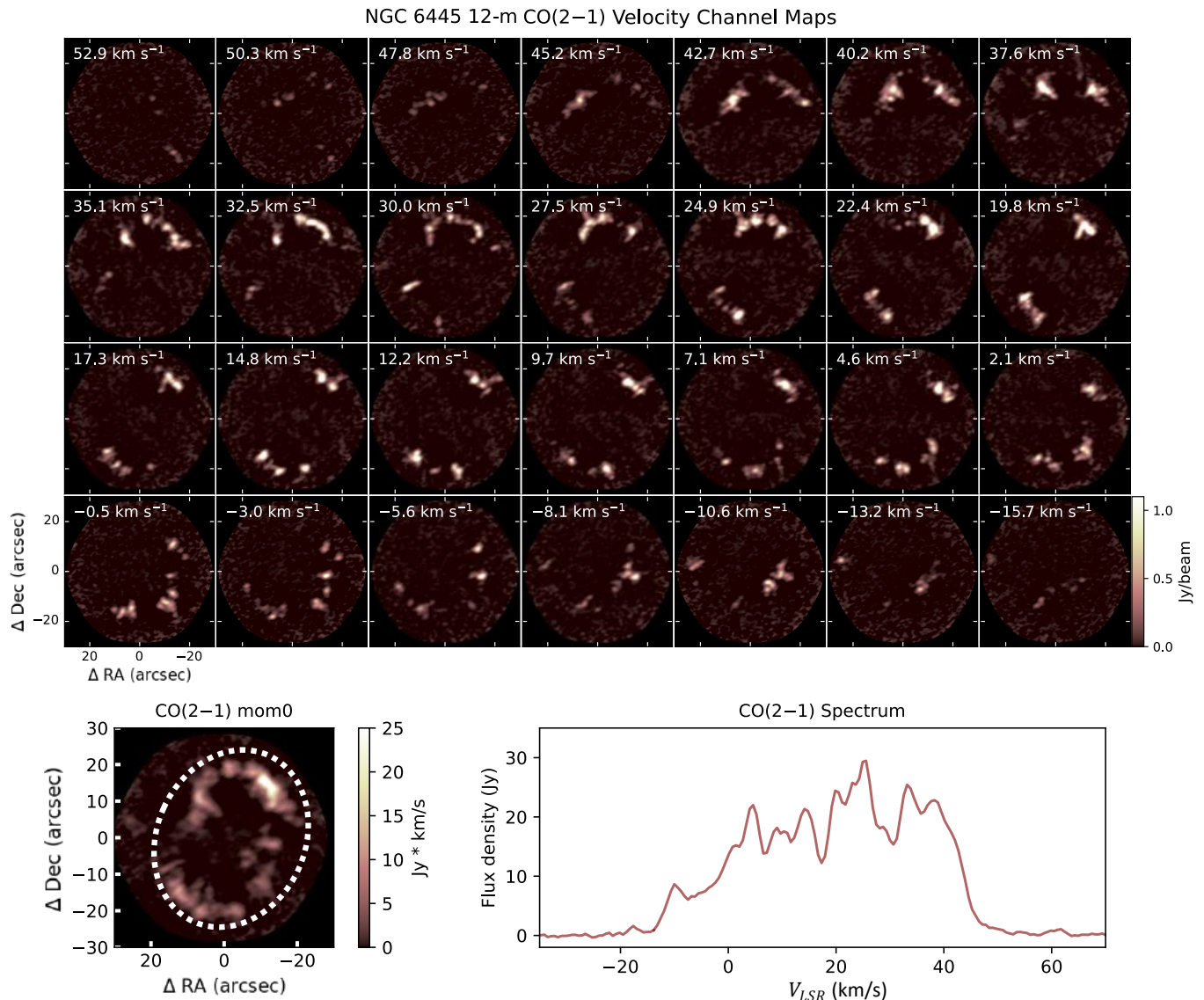


**Figure 12.** Same as Fig. 4, but displaying ALMA Band 6 data for NGC 6445. Velocity channels are displayed in increments of 2.6 km s<sup>-1</sup>.

HNC and hyperfine transitions of CN in the ACA observations (Fig. 13) and CS in the 12-m array observations (Fig. 14). As in the case of Hubble 5, the small number of molecules observed reflects observing time limitations for both ACA and 12-m arrays.

It is immediately apparent from Fig. 12 that the <sup>12</sup>CO emission traces the bright ring of optical line emission surrounding the nebula’s inner cavity. All molecular emission lines detected in NGC 6445 follow this same overall morphology. In the <sup>12</sup>CO velocity channel maps, the molecular gas appears in the form of an elliptical ring of clumps tracing the pinched waist of the nebula, with clump velocities extending from roughly -10 km s<sup>-1</sup> to +45 km s<sup>-1</sup>. Thus — with the benefit of ALMA’s spatial resolution — we can conclude that the molecular gas within NGC 6445 is largely confined to an expanding, clumpy molecular torus, as opposed to multiple polar outflow components, as previously suggested on the basis of single-dish molecular line spectroscopy (Schmidt et al. 2022).

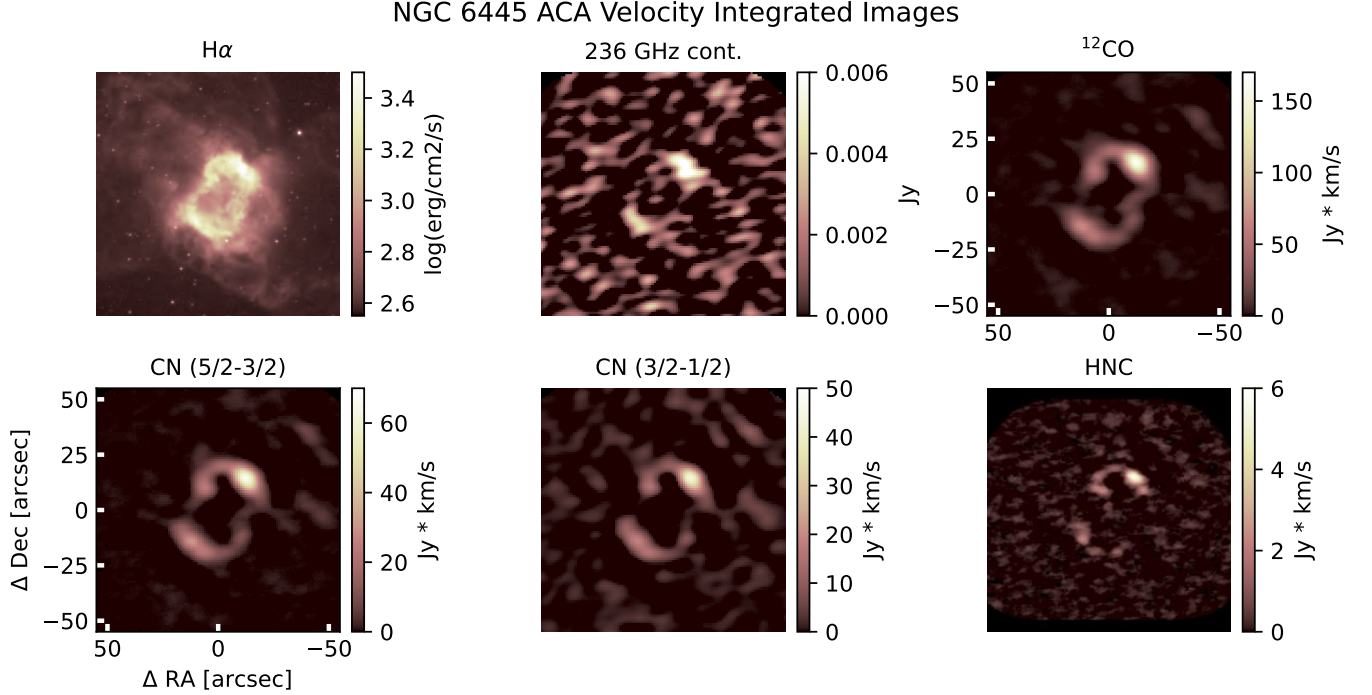


**Figure 13.** As in Fig. 5, but displaying ALMA Band 6 ACA mom0 images for NGC 6445. *Top left panel:* an archival NOT H $\alpha$  image of NGC 6445. *Second panel:* continuum emission at 236 GHz (C43-1) as received from the ALMA pipeline. *Following panels:*  $^{12}\text{CO}$ , CN (5/2–3/2), CN (3/2–1/2), and HNC. All images have a field of view of  $120'' \times 120''$ .

The  $^{12}\text{CO}$  channel maps and integrated spectrum indicate that the molecular torus is expanding at roughly  $30 \text{ km s}^{-1}$ , with the SW region of the shell moving towards the observer and the NE region moving away. All spatially-integrated spectral profiles for NGC 6445 are shown in Appendix B.

#### 4.5. NGC 2899

Channel maps, mom0 image, and spectral line profile extracted from the 12-m Band 6 observations of  $^{12}\text{CO}$  emission from NGC 2899 are presented in Fig. 15. Molecular detections in NGC 2899 include  $^{12}\text{CO}$ ,  $^{13}\text{CO}$ , CN, HCN, and  $\text{HCO}^+$  in 12-m and ACA observations with a detection of HNC in ACA observations only (see Figs. 16–17). All spatially-integrated spectral profiles for NGC 2899 are presented in Appendix B.

Unlike the PNe that have been discussed thus far in this section, the molecular emission from NGC 2899 appears in the form of clumps along the pinched waist of the nebula rather than a complete toroidal structure. In Fig. 15, the  $^{12}\text{CO}$  emission resides mainly in two structures along the central cavity. There is a smaller clump on the W edge of the cavity, which appears in ACA as well as 12-m observations, along with faint, short filaments that trail along the S edge of the cavity, only visible in the 12-m data (see Figs. 16 and 17). The two main knot structures are expanding away from each other at  $\sim 13 \text{ km s}^{-1}$ , while the fainter structures have an expansion speed of  $\sim 22 \text{ km s}^{-1}$ . Whether or not all of these structures were once part of the same ring of molecular gas is unclear; the knots may be the remnants of a multiple ring system. Regardless, the fragmented structure of the molecular gas found in NGC 2899 indicates that this nebula is quite evolved, consistent with the conclusions of Lopez et al. (1991).

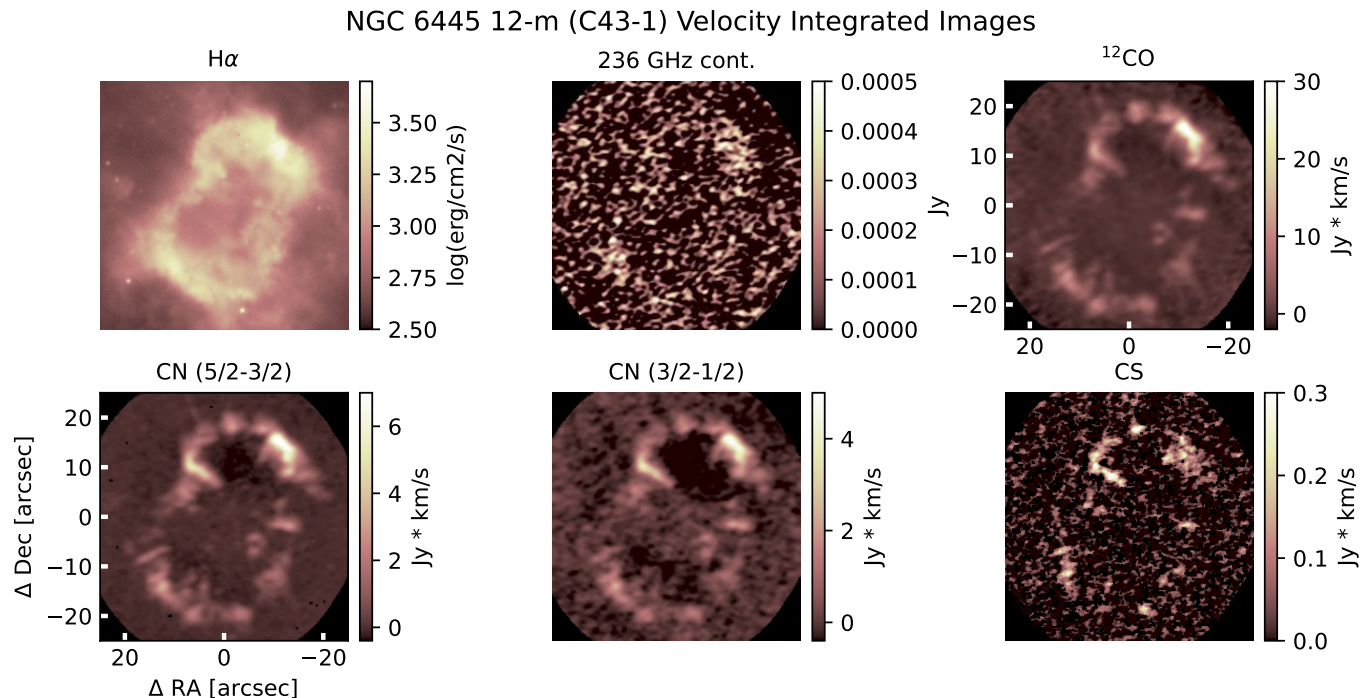


**Figure 14.** As in Fig. 5, but displaying ALMA Band 6 12-m mom0 images for NGC 6445. *Top left panel:* an archival NOT H $\alpha$  image of NGC 6445. *Second panel:* continuum emission at 236 GHz (C43-1) as received from the ALMA pipeline. *Following panels:*  $^{12}\text{CO}$ , CN (5/2–3/2), CN (3/2–1/2), and CS, respectively. All images have a field of view of  $50'' \times 50''$ .

#### 4.6. NGC 2818

Channel maps, mom0 image, and spectral line profile extracted from the 12-m Band 6 observations of  $^{12}\text{CO}$  emission from PN NGC 2818 are presented in Fig. 18. Molecules detected in NGC 2818 include  $^{12}\text{CO}$ ,  $^{13}\text{CO}$ , CN, HCN, and  $\text{HCO}^+$  in both ACA and 12-m arrays along with a detection of CS in 12-m array observations only and a detection of HNC in ACA observations only (see Figures 19 and 20 for ACA and 12-m array observations, respectively). As in the case of NGC 2899, just discussed, the molecular torus of NGC 2818 appears to be highly fragmented. In Fig. 18, the  $^{12}\text{CO}$  emission traces the filament structures that spread across the center of the nebula in optical emission-line images (Fig. 3). The 12-m array observations of  $^{12}\text{CO}$  reveal finer structures that wrap around the central cavity of ionized gas. From these observations, we infer that the clumps of molecular gas were once part of a nearly edge-on, molecular torus, suggesting that NGC 2818 is indeed an evolved PN. The remnant of this molecular torus is expanding at  $\sim 17 \text{ km s}^{-1}$ , with the eastern-most clumps moving towards the observer and the western-most clump moving away. All spatially-integrated spectral line profiles for NGC 2818 are shown in Appendix B.

## 5. DYNAMICAL AGES

### 5.1. Measurements

In order to calculate the dynamical age of a PN's central torus, we assume that the molecular emission regions have simple toroidal geometries, radially expanding with uniform velocities. By assuming that the intrinsic shape of the torus is perfectly circular, the problem is simplified to one

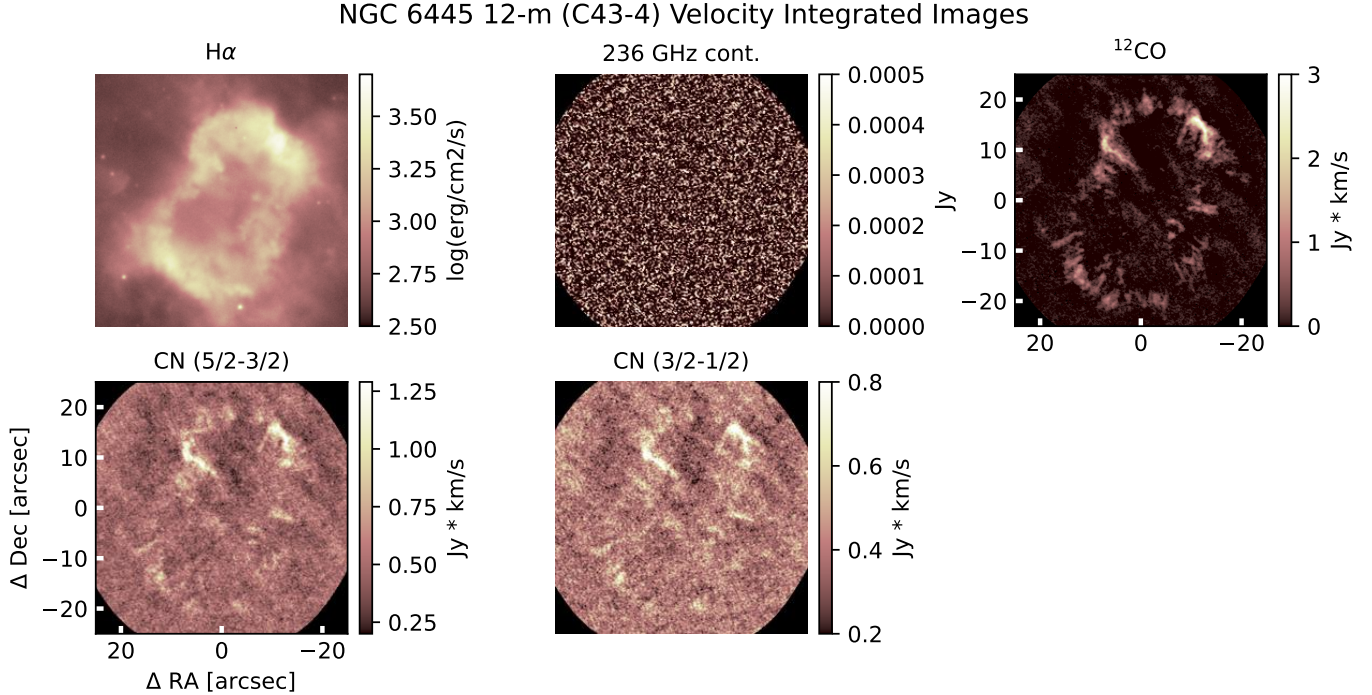


**Figure 14.** (cont.) *Top left panel:* an archival NOT H $\alpha$  image of NGC 6445. *Second panel:* continuum emission at 236 GHz (C43-4) as received from the ALMA pipeline. *Following panels:*  $^{12}\text{CO}$ , CN (5/2–3/2), and CN (3/2–1/2), from left to right. All images have a field of view of  $50'' \times 50''$ .

dimension of motion with one inclination angle  $i$ , defined as the angle of inclination with respect to the plane of the sky (where  $i = 90^\circ$  is defined as edge-on). Fig. 21 shows how the orientation of each molecular torus was defined with respect to the mom0 image and the projected (redshifted and blueshifted) velocity components of the molecular gas for the target PNe, which in turn are used to estimate the projected expansion velocity of each torus. The dynamical age  $t$  is then

$$t \text{ (yr)} = 4.8 a \sin i D V_{\text{exp}}^{-1} \quad (1)$$

where  $a$  is the angular size of the projected ellipse’s semi-major axis in arcseconds;  $i$  is given by  $\cos^{-1}(b/a)$ , where  $b/a$  is the projected ellipse semi-minor to semi-major axis ratio;  $D$  is the adopted distance to the PN in pc; and  $V_{\text{exp}}$  is the estimated projected expansion velocity in  $\text{km s}^{-1}$ .

The  $^{12}\text{CO}$  ALMA Band 6 data in 12-m configuration are used to estimate the ellipse parameters of each nebula because these data resolve the tori more readily than the ACA data. The inferred ellipse parameters used for dynamical age estimates, as well as the resulting ages, are listed in Table 5. The listed uncertainties in these dynamical ages reflect the uncertainties in our adopted distances, and do not reflect systematic errors in the determination of the dimensions and inclinations of the molecular tori (i.e., the ellipse parameters). The resulting dynamical ages of the molecular tori range from  $\sim 500$  yr (Hubble 5) to  $\sim 11000$  yr (NGC 2818).

### 5.2. Comparisons with Previous Estimates

Although mm-wave transitions of CO (and, in some cases, other trace molecules) had been previously detected in all six of the PNe included in our ALMA Band 6 mapping survey (see §§ 4.1–4.5),

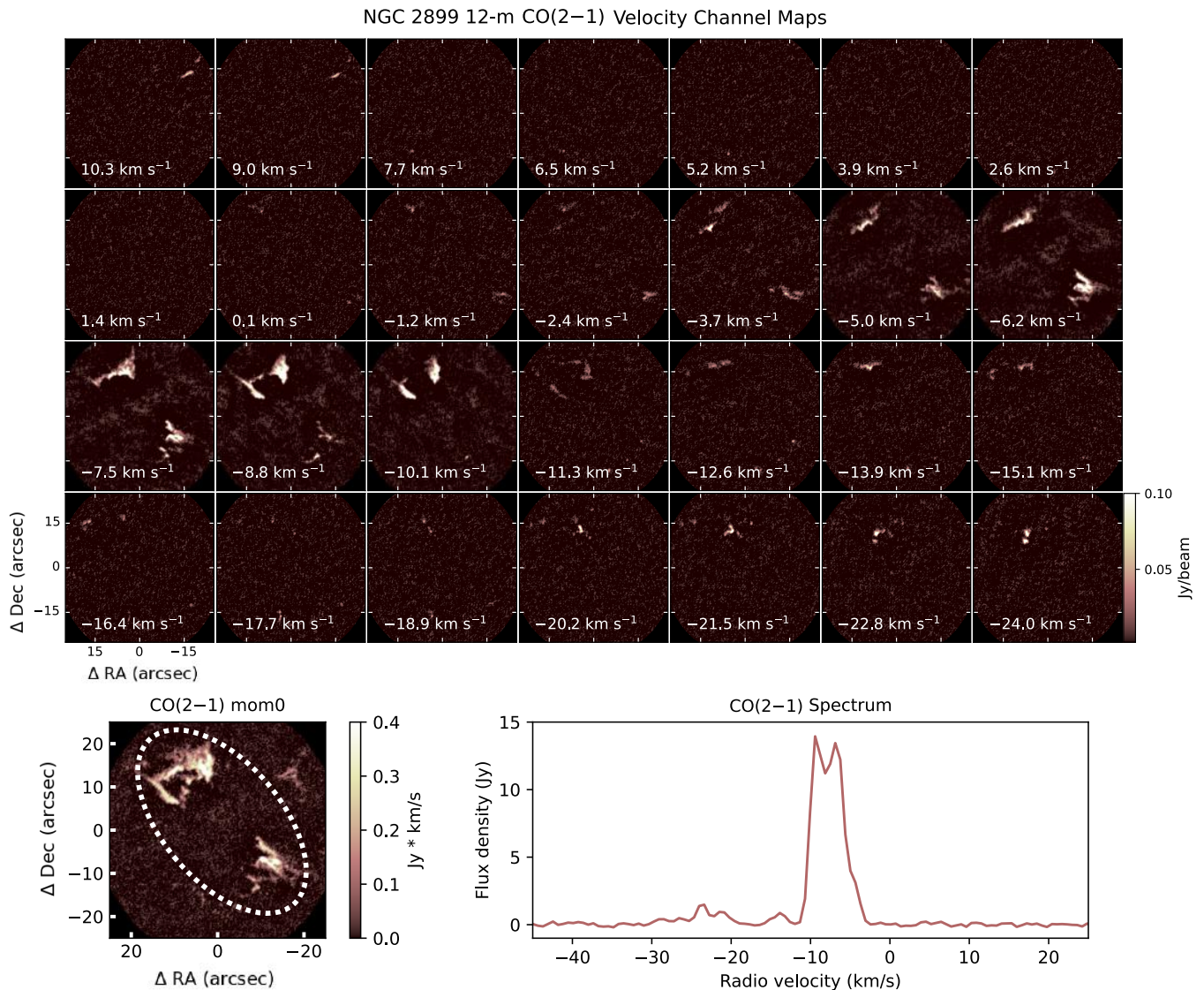


**Figure 15.** Same as Fig. 4, but displaying 12-m Band 6 data for NGC 2899. Velocity channels are displayed in increments of  $1.3 \text{ km s}^{-1}$ .

only NGC 6302 has previously been mapped at sufficient spatial and spectral resolution (by ALMA) to resolve its central torus and thereby estimate a torus dynamical age (2200 yr; Santander-García et al. 2017). The estimated molecular torus dynamical ages of the other five nebulae reported in Table 5 are hence the first such direct determinations for these PNe. In the following, we compare these estimated torus dynamical ages with PN dynamical ages reported in the literature, almost all of which describe the expansion ages of the bipolar lobes (as opposed to the equatorial tori) of the PNe.

*Hubble 5:* On the basis of long-slit optical spectroscopy data, López et al. (2012) determined an age for the optical lobes of  $1500 \pm 540 \text{ yr}$  assuming a distance of 1.7 kpc. This age estimate decreases to  $800 \pm 300 \text{ yr}$  for our revised distance of 0.9 kpc. The molecular torus dynamical age derived in this work,  $\sim 500 \text{ yr}$ , hence falls at the lower end of the range of uncertainty in the López et al. (2012)

## NGC 2899 ACA Velocity Integrated Images

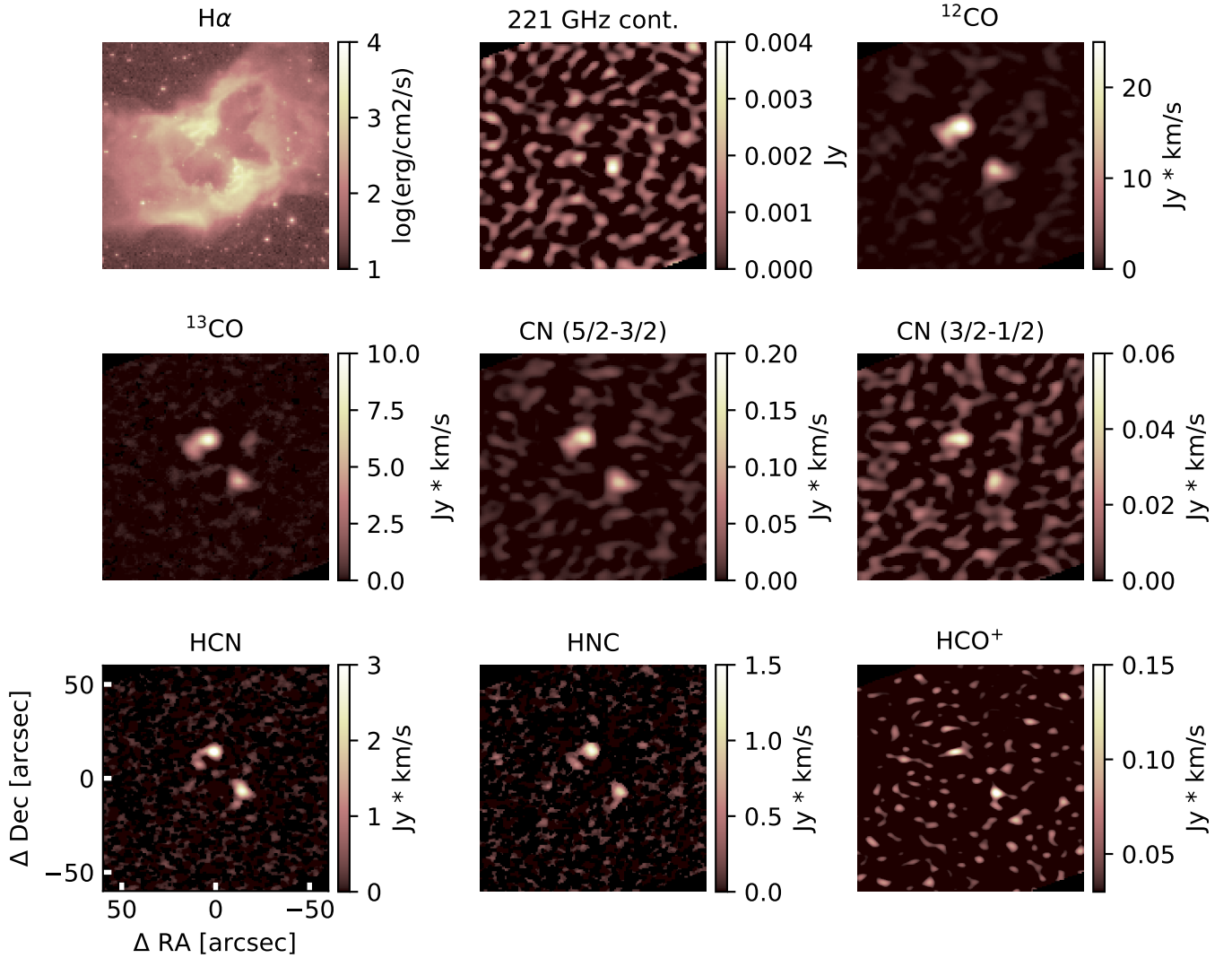


**Figure 16.** Same as Fig. 5, but displaying ACA Band 6 data for NGC 2899. *Top left panel:* an archival ESO H $\alpha$  image. *Second panel:* continuum emission at 221 GHz. *Following panels:*  $^{12}\text{CO}$ ,  $^{13}\text{CO}$ , CN (5/2–3/2), CN (3/2–1/2), HCN, HNC, and HCO $^+$ . All images have a field of view of 120'' x 120''.

estimate. The molecular torus inclination angle we derive from the ALMA CO mapping ( $55^\circ$ ) is similar to that estimated for the inclination of the nebula’s polar axis ( $62^\circ$ ; López et al. 2012).

*NGC 2440:* We find a molecular torus dynamical age of  $\sim 1500$  yr and inclination angle of  $i = 65^\circ$ . Previous dynamical age estimates for the optical lobes of NGC 2440 range between 2100 and 4200 yr (Baessgen et al. 1995; Gorny et al. 1997; Schmidt & Ziurys 2016, and references therein), after correcting to our revised distance estimate of 1.0 kpc. However, there is evidence the lobes may be much younger dynamically. Lago & Costa (2016) used comprehensive long-slit spectroscopy as the basis for detailed 3D spatio-kinematical modeling of the nebula, determining inclinations of  $\sim 63^\circ$  and  $\sim 90^\circ$  for its two main lobe pairs, oriented at position angles of  $85^\circ$  and  $35^\circ$ , respectively; the

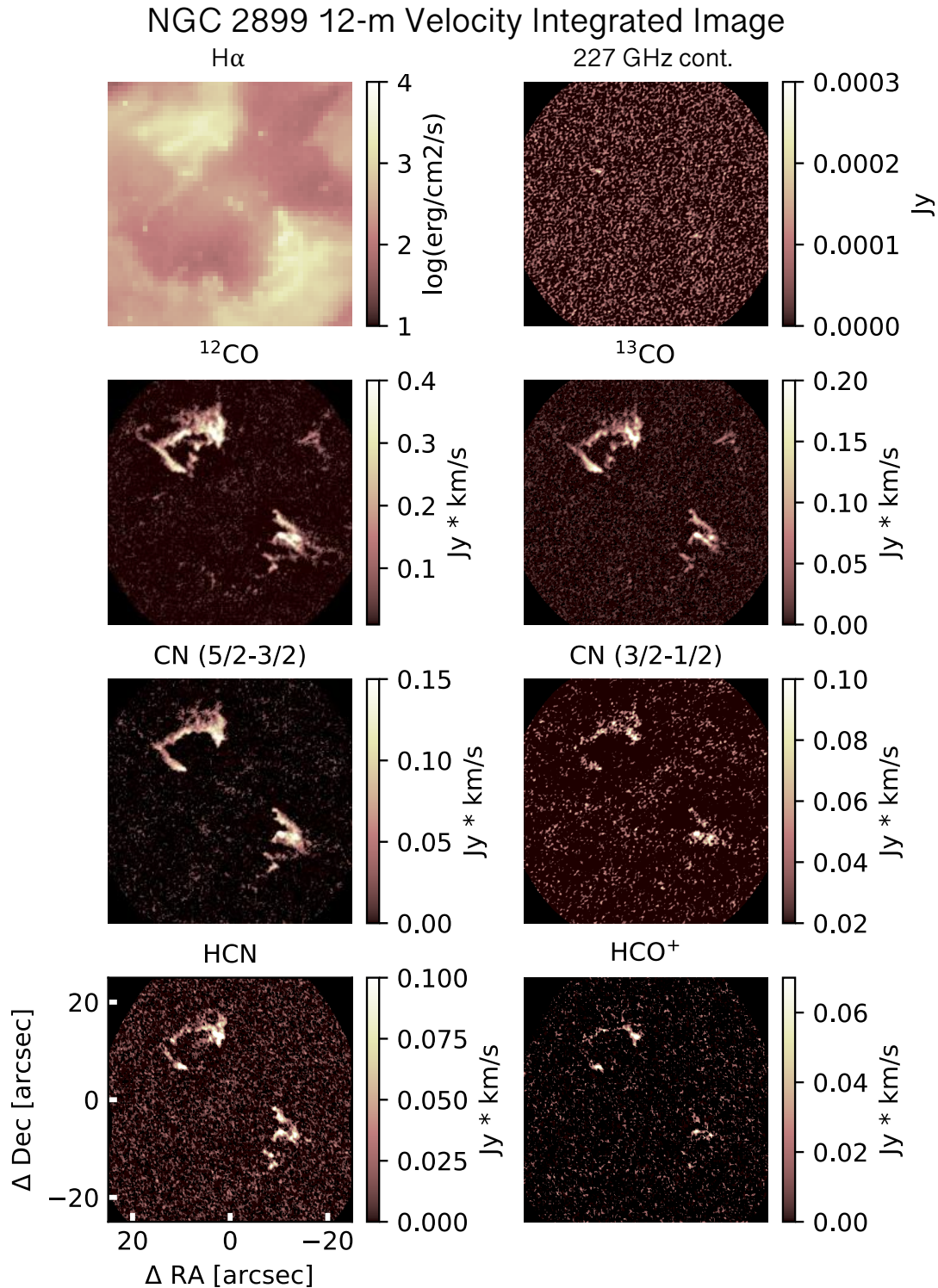


**Figure 17.** Same as Fig. 5, but displaying 12-m Band 6 data for NGC 2899. *Top left panel:* is an archival ESO H $\alpha$  image. *Second panel:* continuum emission at 227 GHz. *Following panels:*  $^{12}\text{CO}$ ,  $^{13}\text{CO}$ , CN (5/2–3/2), CN (3/2–1/2), HCN, and HCO $^+$ . All images have a field of view of 50'' x 50''.

former agrees well with the polar axis inclination of  $65^\circ$  listed in Schwarz et al. (2008), as well as

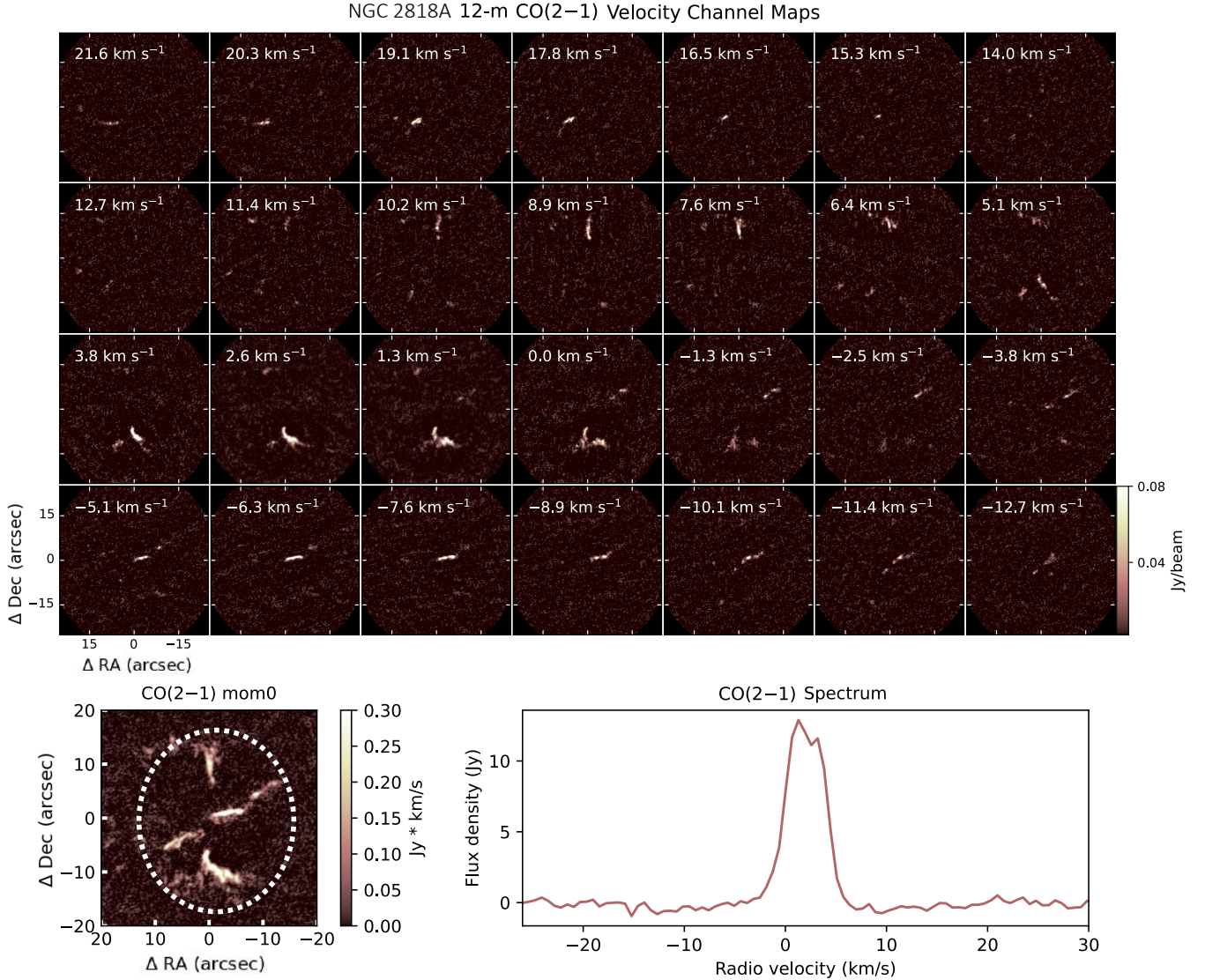


**Figure 18.** Same as Fig. 4, but displaying 12-m Band 6 data for NGC 2818. Velocity channels are displayed in increments of  $1.2 \text{ km s}^{-1}$ .

our inferred torus inclination. Although [Lago & Costa \(2016\)](#) do not estimate dynamical ages for the optical lobe pairs, their inferred expansion velocities of  $184 \text{ km s}^{-1}$  and  $160 \text{ km s}^{-1}$  for the PA  $85^\circ$  and  $35^\circ$  lobe pairs (respectively) would imply very young dynamical ages of  $\sim 800\text{--}1000 \text{ yr}$  for these structures, given our adopted distance of  $1.0 \text{ kpc}$  to NGC 2440. Our estimated molecular torus dynamical age,  $\sim 1500 \text{ yr}$ , hence indicates that this equatorial torus structure was ejected well before the polar lobe pairs.

*NGC 6302:* Our estimated molecular torus inclination of  $i = 70^\circ$  and dynamical age of  $\sim 3300$  years are in good agreement with previous estimates of  $75^\circ$  and  $2500\text{--}3700$  years, respectively, as obtained from far more detailed structural modeling of early-cycle ALMA  $^{12}\text{CO}(3\text{--}2)$  mapping data ([Santander-García et al. 2017](#)). The torus inclination is similar to that inferred for the bipolar lobe symmetry axis ( $70^\circ$ ; [Schwarz et al. 2008](#)). Recent analysis of proper motions of knots and features in the optical (ionized) nebula, as imaged by HST/WFC3 over a  $\sim 10 \text{ yr}$  interval, revealed

**Table 5.** MOLECULAR TORUS DYNAMICAL AGE MEASUREMENTS

PN G	Name	Distance (kpc)	Ellipse Dimensions ( $a, b$ )	Incl. Angle $i^a$ ( $^\circ$ )	Expansion Velocity $^a$ (km/s)	Dynamical Age $^a$ (yrs)	Optical Lobe Incl. Angle ( $^\circ$ )	Optical Lobe Dyn. Age (yrs)
359.3-00.9	PN Hb 5	$0.9^{+0.1}_{-0.1}$	(4.5'', 2.5'')	55	30	$500^{+120}_{-120}$	62 <sup>b</sup>	800 <sup>b</sup>
234.8+02.4	NGC 2440	$1.0^{+0.1}_{-0.1}$	(5.0'', 2.5'')	65	17	$1500^{+360}_{-360}$	65 <sup>c</sup>	1000 <sup>d</sup>
349.5+01.0	NGC 6302	$1.0^{+0.1}_{-0.1}$	(11.0'', 3.5'')	70	14	$3300^{+660}_{-660}$	70 <sup>c</sup>	900–2300 <sup>e</sup>
008.0+03.9	NGC 6445	$1.1^{+0.1}_{-0.1}$	(18.0'', 13.0'')	50	22	$3700^{+550}_{-550}$	50 <sup>c</sup>	3400 <sup>f</sup>
277.1-03.8	NGC 2899	$0.8^{+0.2}_{-0.2}$	(16.0'', 6.0'')	70	8	$7600^{+2200}_{-2200}$	75 <sup>c</sup>	5400 <sup>g</sup>
261.9+08.5	NGC 2818	$3.3^{+0.1}_{-0.1}$	(10.0'', 5.0'')	60	12	$11000^{+2000}_{-2000}$	60 <sup>h</sup>	7400–11000 <sup>b,i</sup>

NOTES: (a) This work; age uncertainties are determined by distance errors and uncertainties in ellipse dimensions of 0.5''; the expansion velocities listed in this table correspond to emission in the molecular torus only, these are different from the expansion velocities listed in Appendix A which are derived using all observed emission for each molecular line. (b) López et al. 2012. (c) Schwarz et al. 2008. (d) See text. (e) Balick et al. 2023. (f) Dynamical age of central ionized region as estimated by van Hoof et al. 2000. (g) Based on data presented in Lopez et al. 1991; see text. (h) Vázquez 2012. (i) Derlopa et al. 2024. All literature ages for optical lobes are corrected using this work’s adopted distances; see text.

multiple, point-symmetric zones within its bipolar lobe system; these lobe zones (knot systems) have dynamical ages ranging from  $\sim 900$  yr to  $\sim 2300$  yr, strongly suggestive of episodic, misaligned polar outflows (Balick et al. 2023). The estimated dynamical age of the oldest of these episodic polar lobe ejections revealed by multi-epoch HST imaging, which is very similar to that deduced from ground-based proper motion measurements of clumps in the outermost regions of the NW lobe (2200 yr; Meaburn et al. 2008), would make the lobes somewhat younger than the molecular torus, based on the dynamical ages estimated from ALMA CO data both via our simple analysis and the detailed modeling of Santander-García et al. (2017).

*NGC 6445*: The projected elliptical shape and velocity extremes of the clumpy molecular emission ring within this PN yield an intermediate inclination of  $i = 50^\circ$  and a molecular torus dynamical age of  $\sim 3700$  years. This estimated dynamical age is within the range of previously determined dynamical ages for the molecular emitting region ( $\sim 4600$  yr, based on assumed emitting region radius; Schmidt et al. 2022) and the central  $\sim 40'' \times 30''$  ionized region ( $\sim 3400$  yr; van Hoof et al. 2000), where we have corrected both age estimates for our adopted distance. We find no previous literature measurements of the expansion velocities and (hence) dynamical ages for NGC 6445’s polar lobes. However, our inferred molecular torus inclination is in good agreement with the polar axis inclination of  $50^\circ$  listed in Schwarz et al. (2008).

*NGC 2899*: This PN is estimated to have the second oldest molecular torus in our ALMA Band 6 survey, with a dynamical age of  $\sim 7600$  years. We find a torus inclination of  $i = 70^\circ$ , in good agreement with the polar axis inclination of  $i = 75^\circ$  listed in Schwarz et al. (2008). Based on the polar lobe expansion velocities of  $\sim 100$ – $130$  km s $^{-1}$  measured by Lopez et al. (1991) and the ( $\sim 60''$ ) extent of the lobes in their images, we roughly estimate a polar lobe dynamical age of 5400 yr, suggesting the lobes are somewhat younger than the molecular torus.

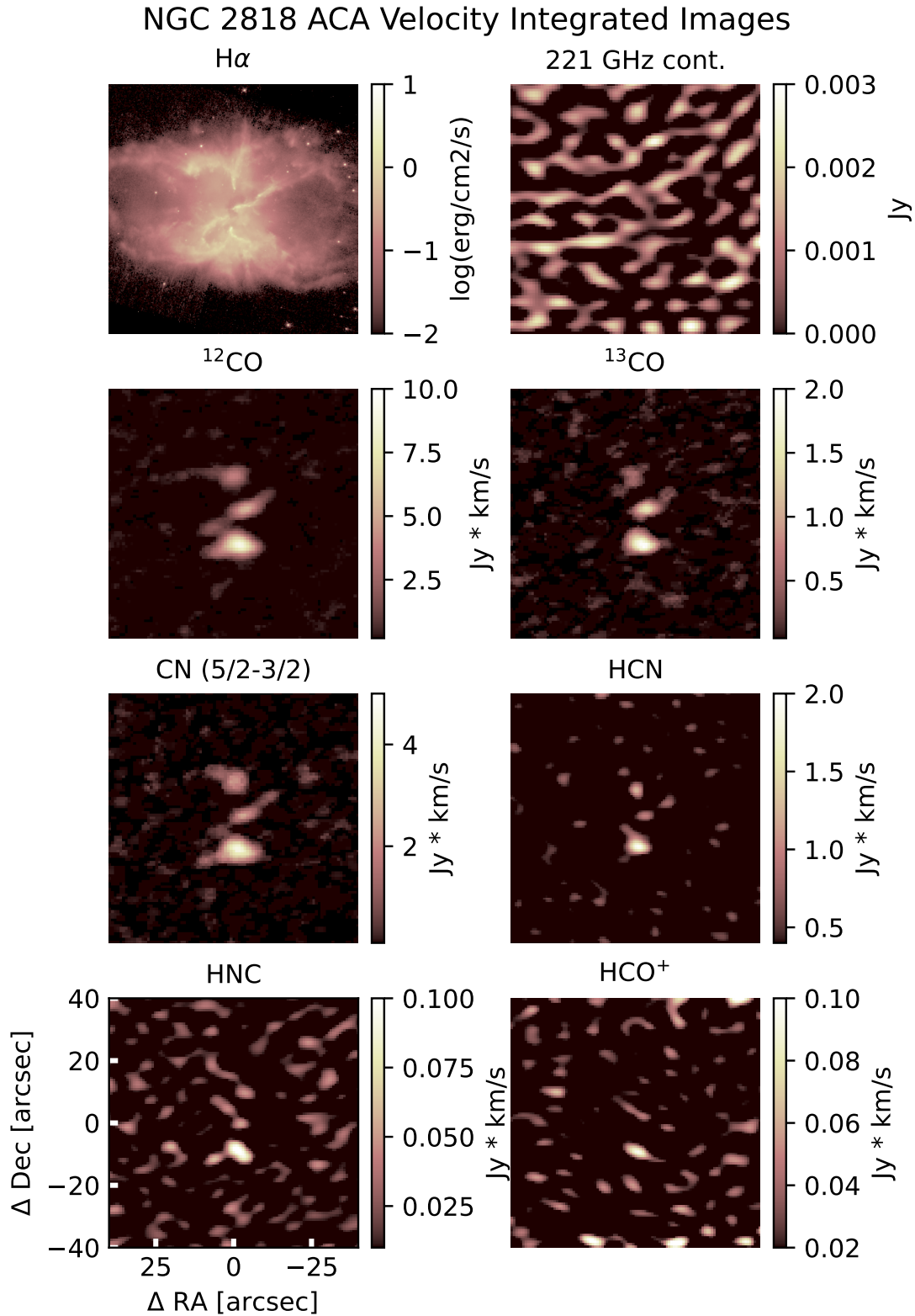


**Figure 19.** Same as Fig. 5, but displaying ACA Band 6 data for NGC 2818. *Top left panel:* an archival HST/WFPC2 H $\alpha$  image of NGC 2818. *Second panel:* continuum emission at 221 GHz (ACA) as received from the ALMA pipeline. *Following panels:*  $^{12}\text{CO}$ ,  $^{13}\text{CO}$ , CN (5/2–3/2), HCN, HNC, and HCO $^+$ . All images have a field of view of 80'' x 80''.

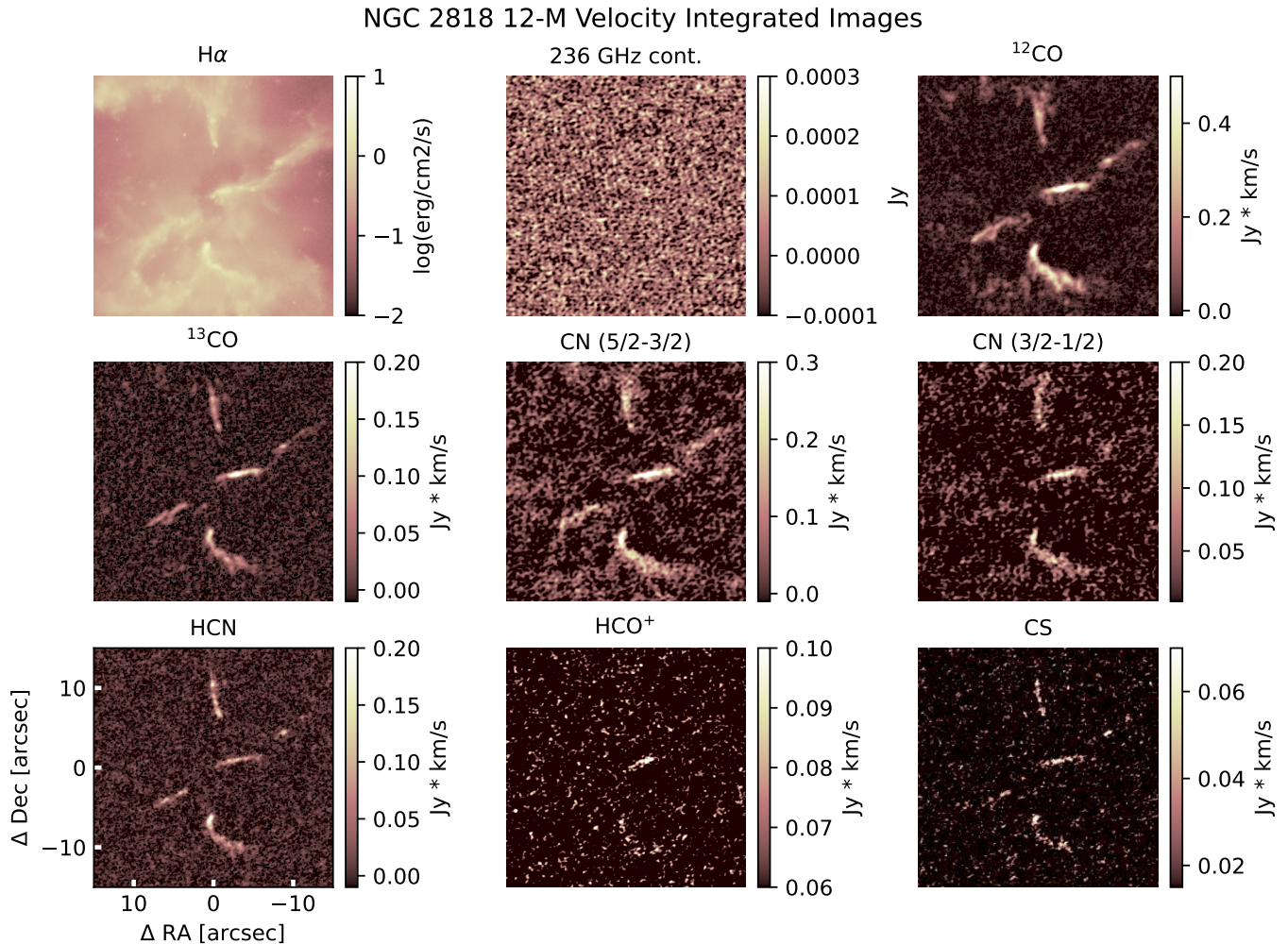


**Figure 20.** Same as Fig. 5, but displaying 12-m Band 6 data for NGC 2818. *Top left panel:* an archival HST/WFPC2 H $\alpha$  image. *Second panel:* continuum emission at 236 GHz (C43-4) as received from the ALMA pipeline. *Following panels:*  $^{12}\text{CO}$ ,  $^{13}\text{CO}$ , CN (5/2–3/2), CN (3/2–1/2), HCN, HCO $^+$ , and CS. All images have a field of view of 30'' x 30''.

*NGC 2818:* We find an inclination of  $i = 60^\circ$  and a dynamical age for the molecular torus in the range 9000–13000 yr, adopting the (open-cluster-based) distance of 3.3 kpc. Vázquez (2012) found a polar axis inclination of  $i = 60^\circ$  and a dynamical age for the polar lobes of  $\sim 11000$  yr, while Derlopa et al. 2024 found  $i = 70^\circ$  and  $\sim 7400$  yr, respectively (where we have rescaled both previous dynamical age estimates to our revised PN distance). Given either age estimate, it is apparent that the molecular torus dynamical age is far older than that of the lobes.

### 5.3. Discussion

The results for dynamical age in Table 5 are consistent with the progression of molecular torus morphologies described in §§4.1–4.5, wherein the dynamically younger PNe (Hubble 5, NGC 2440, NGC 6302, and NGC 6445) have the most coherent central molecular ring structures (see Figs. 5, 8, 11, and 14, respectively) and the oldest PNe (NGC 2899 and NGC 2818) have more fragmented structures (see Figs. 17 and 20, respectively). Furthermore, this sequence also represents a monotonic

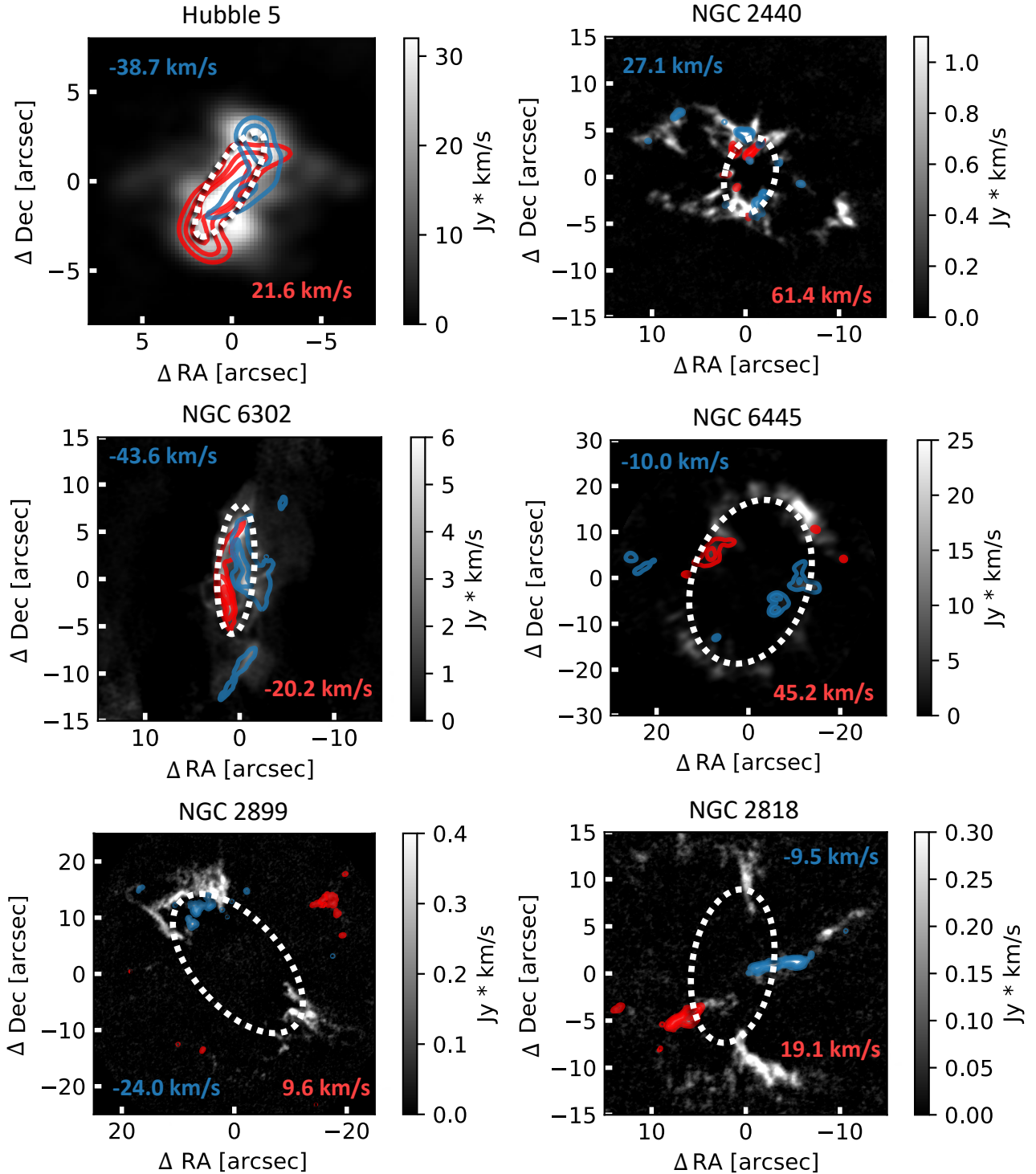


**Figure 21.** Contours of redshifted (red) and blueshifted (blue) emission components overlaid on greyscale  $mom_0$  images for Hubble 5, NGC 2440, NGC 6302, NGC 6445, NGC 2899, and NGC 2818, as extracted from the 12-m array  $^{12}CO(2-1)$  data cubes. The central  $V_{LSR}$  used to highlight the red- and blueshifted components are noted in each panel with red and blue text, respectively. A set of 3 channels centered around the  $V_{LSR}$  velocities labeled in the figure were used to create the blue and red contour maps with a total velocity range of  $1.9 \text{ km s}^{-1}$  for all PNe. White dotted ellipses overlaid on the emission components denote the (projected) molecular torus geometry adopted for each PN (with ellipse parameters listed in Table 5).

decline in mm-wave continuum emission from ionized gas at the nebular cores, wherein Hubble 5, NGC 2440, and NGC 6302 display bright continuum emission from their tori, NGC 6445 displays relatively weak continuum emission, and NGC 2899 and NGC 2818 are undetected. Only the dynamically youngest PNe — Hb 5, NGC 2440, NGC 6302 — display emission from molecular gas within their optical (polar) lobes, in the form of bubble-like structures; NGC 2440 also displays twin knots of CO and trace molecule emission that coincide with optical condensations at the tips of one of its two main sets of polar lobes.

Furthermore, a pattern emerges across this sample of extreme, high-excitation bi-lobed PNe in which the molecular torus dynamical ages are consistently older than the dynamical ages of the optical lobes (Table 5). The lone exception is the dynamically youngest sample PN, Hb 5, for which the torus and lobe ages are the same to within the uncertainties. The comparison of torus vs. lobe dynamical ages in Table 5 hence generally supports the schematic “jet lag” model describing the evolution of bipolar PNe (Huggins 2007), wherein the ejection of a molecular torus precedes the fast, collimated outflows that form the lobes of ionized gas observed in the optical/IR (see also Kastner et al. 2025a, and references therein). Indeed, the dynamically younger sample PNe display evidence of multiple collimated outflows during their post-torus-ejection PN stages. Such episodic ejections are apparent both through determinations of the ages of point-symmetric lobe substructures (e.g., NGC 6302; Balick et al. 2023, and references therein) as well as via inspection of their optical lobe morphologies (e.g., Hb 5, NGC 2440, NGC 6445; see Fig. 3 and discussions in López et al. 2012; Lago & Costa 2016).

The strong implication is that molecular torus ejection represents the final major mass loss stage of the progenitor AGB stars of these pinched-waist bipolar PNe, and that this equatorially-directed mass loss then leads directly to a phase of collimated, episodic (and perhaps precessing) polar outflows from the vicinities of their hot, luminous central stars. We note that this general scenario is the same as that proposed to explain the structural evolution of ring-like PNe (Kastner et al. 2024, 2025b, and references therein) as well as the complex juxtaposition of structures observed in the young, molecule-rich, high-excitation PN NGC 7027 (Bublitz et al. 2023; Moraga Baez et al. 2023, and references therein). Indeed, in NGC 7027, we are likely seeing the immediate precursor to somewhat (dynamically) older bipolar PNe Hb 5, NGC 2440, NGC 6302, and NGC 6445, which in turn represent precursors to the dynamically old — yet still high-excitation and molecule-rich — NGC 2899 and NGC 2818.

## 6. H<sub>2</sub> MASSES

### 6.1. Mass Estimation from CO Lines

As in most astrophysical environments, the masses of cold molecular gas in PNe are most easily measured via mm-wave observations of rotational lines of CO, the second most abundant molecule after H<sub>2</sub>, as H<sub>2</sub> has no dipole moment and the low-lying rotational energy levels of CO are readily excited even in low-density ( $n \gtrsim 10^2 \text{ cm}^{-3}$ ) regions. We hence follow standard practice (e.g., Kastner et al. 2024, and references therein) and estimate H<sub>2</sub> masses from the ACA <sup>12</sup>CO(2–1) and <sup>13</sup>CO(2–1) observations of our target PNe by modeling these line intensities to obtain pixel-by-pixel CO column densities across each object, with the <sup>12</sup>CO brightness temperatures serving to constrain the emitting region kinetic temperatures; integrating the resulting column densities over each PN’s CO emission

region, to obtain the total number of CO molecules; and, finally, applying assumptions for CO:H<sub>2</sub> number ratios to obtain the total number (hence mass) of H<sub>2</sub> molecules.

To estimate the CO column densities, we used the RADEX statistical equilibrium radiative transfer code (van der Tak et al. 2007). For the purpose of these estimates, both <sup>12</sup>CO(2–1) and <sup>13</sup>CO(2–1) lines are assumed to be optically thin; for many or perhaps most of the sample objects, the former assumption may not hold (see below). We use the peak main-beam antenna temperature  $T_{mb}$  within the <sup>12</sup>CO(2–1) data cube to provide a lower limit on the kinetic temperature  $T_k$  via  $T_{mb} \sim T_k - T_{bg}$  (Dinh-V-Trung et al. 2008b), where  $T_{bg}$  is the temperature of the cosmic background radiation and the main beam brightness temperature<sup>3</sup>  $T_{mb}$  is obtained via

$$T_{mb} = 1.222 \times 10^3 \frac{I}{\nu^2 \theta_{maj} \theta_{min}}, \quad (2)$$

with  $I$  the line intensity in mJy beam<sup>-1</sup>,  $\nu$  the frequency of emission in GHz, and  $\theta_{maj}$  and  $\theta_{min}$  the major and minor axes of the beam in arcseconds. For most of the PNe, the resulting  $T_k$  range from 18 to 40 K (Table 6), consistent with previous inferred molecular gas kinetic temperatures in PNe (e.g., Bachiller et al. 1997). The PN NGC 6302 is a notable outlier, with a far higher peak  $T_{mb}$  within its brightest <sup>12</sup>CO(2–1) emitting region, leading to a relatively high inferred  $T_k$  of 84 K.

With these <sup>12</sup>CO-based estimates of  $T_k$  as constraints, we used RADEX to obtain the column densities of <sup>12</sup>CO and <sup>13</sup>CO ( $N_{CO}$ ) from the observed <sup>12</sup>CO(2–1) and <sup>13</sup>CO(2–1) line brightness temperatures. We assume an H<sub>2</sub> number density of  $n_{H_2} = 10^4$  cm<sup>-3</sup>, which is near the lower bound of the likely range of molecular gas densities in PNe (e.g., Schmidt & Ziurys 2016; Kastner et al. 2024, and references therein); the results for column densities are relatively insensitive to the assumed value of  $n_{H_2}$ . The resulting cubes of column density per pixel were computed for both <sup>12</sup>CO and <sup>13</sup>CO for regions above the 1 $\sigma$  background (root mean square) noise level; the mean <sup>12</sup>CO and <sup>13</sup>CO column densities derived from these RADEX calculations are listed in Table 6. A caveat in interpreting these results is that the <sup>12</sup>CO column density calculations are less reliable for lines of sight for which <sup>12</sup>CO(2–1) is optically thick. While <sup>12</sup>CO(2–1) emission appears to be optically thin for many if not most PNe (e.g., Bachiller et al. 1997; Kastner et al. 2024), <sup>12</sup>CO(2–1) will invariably have greater opacity than <sup>13</sup>CO(2–1), and the former may become optically thick in PN regions with especially large H<sub>2</sub> densities. Indeed the ratios of integrated <sup>12</sup>CO(2–1) to <sup>13</sup>CO(2–1) fluxes for our sample PNe fall in the range  $\sim 2 - 5$  (Table 4). These ratios are much smaller than the expected <sup>12</sup>CO/<sup>13</sup>CO abundance ratio (see below), and are similar to the integrated H<sup>12</sup>CO<sup>+</sup>(3–2)/H<sup>13</sup>CO<sup>+</sup>(3–2) and H<sup>12</sup>CN(3–2)/H<sup>13</sup>CN(3–2) flux ratios for the two PNe for which we have measured emission lines from both C isotopologues of these molecules (NGC 6302 and NGC 2440; Table 4), indicating that <sup>12</sup>CO(2–1) is optically thick across some of the emitting regions in these PNe. We further consider this possibility below (§ 6.2).

To estimate total molecular (H<sub>2</sub>) gas masses from the resulting CO column densities, we assume <sup>12</sup>CO:H<sub>2</sub> and <sup>13</sup>CO:H<sub>2</sub> abundance ratios of 10<sup>-4</sup> and 10<sup>-5</sup>, respectively; both are well within the range of CO isotopologue abundances commonly assumed for PNe (e.g., Healy & Huggins 1990; Schmidt et al. 2022; Kastner et al. 2024, and references therein). Adopting these ratios is, of course, also equivalent to assuming a <sup>12</sup>CO:<sup>13</sup>CO abundance ratio of 10. In § 6.2, we consider the implications of, and potential deviations from, this assumed <sup>12</sup>CO:<sup>13</sup>CO abundance ratio.

<sup>3</sup> Formula derived for radio interferometry in <https://science.nrao.edu/facilities/vla/proposing/TBconv>

**Table 6.** MOLECULAR MASS ESTIMATES

PN	Name	T <sub>k</sub> (K)	Column Density <sup>a</sup> (cm <sup>-2</sup> )		Molecular Mass <sup>a</sup> (M <sub>⊙</sub> )		
			<sup>12</sup> CO	<sup>13</sup> CO	<sup>12</sup> CO	<sup>13</sup> CO	Lit.
359.3-00.9	PN Hb 5	29	$(5.8 \pm 0.4) \times 10^{15}$		$(2.3 \pm 0.4) \times 10^{-3}$		$5.0 \times 10^{-3}$ <sup>b</sup>
234.8+02.4	NGC 2440	40	$(4.8 \pm 0.1) \times 10^{15}$	$(5.2 \pm 0.1) \times 10^{15}$	$(1.1 \pm 0.1) \times 10^{-2}$	$(7.4 \pm 1.0) \times 10^{-2}$	$\geq 4.0 \times 10^{-3}$ <sup>c,d,e</sup>
349.5+01.0	NGC 6302	84	$(4.7 \pm 0.1) \times 10^{15}$	$(7.4 \pm 0.1) \times 10^{15}$	$(4.7 \pm 1.7) \times 10^{-3}$	$(6.1 \pm 2.2) \times 10^{-2}$	$1.0 \times 10^{-1}$ <sup>f</sup>
008.0+03.9	NGC 6445	18	$(6.3 \pm 0.1) \times 10^{15}$		$(3.6 \pm 0.3) \times 10^{-2}$		$(2.1 - 3.5) \times 10^{-2}$ <sup>g,e</sup>
277.1-03.8	NGC 2899	29	$(3.7 \pm 0.1) \times 10^{15}$	$(1.1 \pm 0.1) \times 10^{15}$	$(3.6 \pm 1.6) \times 10^{-3}$	$(8.0 \pm 3.6) \times 10^{-3}$	$3.9 \times 10^{-3}$ <sup>e</sup>
261.9+08.5	NGC 2818	18	$(1.8 \pm 0.5) \times 10^{15}$	$(1.4 \pm 0.1) \times 10^{15}$	$(1.5 \pm 0.4) \times 10^{-2}$	$(8.6 \pm 2.3) \times 10^{-2}$	$1.5 \times 10^{-2}$ <sup>e</sup>

NOTES: Error propagation of mass comes from computing additional upper and lower limit values using distance and column density errors. (a) Molecular masses and column densities derived from ACA observations, assuming an H<sub>2</sub> density of  $1 \times 10^4$  cm<sup>-3</sup>. Estimates for NGC 2440 include the N and S molecular lobes observed in ACA observations. Column density values represent the average column density over the molecular torus. References for literature values: (b) Bernard-Salas & Tielens 2005, from mid-IR H<sub>2</sub> emission lines; (c) Dayal & Bieging 1996; (d) Wang et al. 2008; (e) Huggins et al. 1996; (f) Santander-García et al. 2017; (g) Huggins & Healy 1989.

The resulting H<sub>2</sub> masses obtained from the <sup>12</sup>CO and <sup>13</sup>CO column density calculations are listed in Table 6. Given the preceding caveat concerning the possibility that <sup>12</sup>CO(2–1) emission from some or all of our sample PNe may be optically thick, we regard the estimates obtained from <sup>12</sup>CO(2–1) as providing a lower limit on each nebula’s molecular mass. These molecular mass estimates are compared with values from the literature in Table 6 (last column), where we have rescaled these values according to our adopted distances to the sample PNe. The agreement between our ALMA-CO-based molecular masses and previously published molecular mass estimates is generally good, within a factor  $\sim 2$  in all cases. The discrepancies with previous estimates are likely reflective of the fact that many were based on single-dish CO measurements (with the exceptions of NGC 6302 and Hb 5, which were obtained via ALMA <sup>12</sup>CO(3–2) and IR H<sub>2</sub> observations, respectively); discrepancies would also arise from differences in assumed or estimated gas kinetic temperatures.

## 6.2. Discussion

In the optically thin limit, the total molecular (H<sub>2</sub>) masses as estimated from <sup>12</sup>CO and <sup>13</sup>CO should be consistent with one another, if our assumed <sup>12</sup>CO/<sup>13</sup>CO number ratio of 10 is accurate. However, in Table 6, it is clear that the mass estimates obtained from the <sup>13</sup>CO data are systematically larger than those estimated from the <sup>12</sup>CO data. This systematic discrepancy is hence evidence either of large <sup>12</sup>CO opacities, <sup>12</sup>CO/<sup>13</sup>CO abundance ratios  $< 10$ , or both. Selective photodissociation of <sup>13</sup>CO may also affect the modeled <sup>12</sup>CO/<sup>13</sup>CO column density (hence abundance) ratios, although this should raise (as opposed to lower) the derived ratios.

With regard to the possibility that <sup>12</sup>CO is optically thick, we note that the mean <sup>12</sup>CO and <sup>13</sup>CO column densities obtained from the RADEX calculations are very similar for the PNe observed in both isotopologues; whereas, barring exceptional circumstances, one expects <sup>12</sup>CO/<sup>13</sup>CO  $> 1$  and, hence, the derived <sup>12</sup>CO column densities should be larger than those of <sup>13</sup>CO, for pure optically thin emission. Indeed, for the mean column densities in Table 6, the RADEX calculations indicate the <sup>12</sup>CO(2–1) optical depths typically lie in the range  $\tau \sim 0.2$  to  $\sim 1.3$  for the sample PNe, given

the adopted values of  $T_k$  and an assumed  $\text{H}_2$  number density of  $10^4 \text{ cm}^{-3}$ . Thus, it is likely that  $^{12}\text{CO}(2-1)$  is at least marginally optically thick, with values  $\tau > 1.0$  likely along specific lines of sight — a prime example being the region of NGC 6302 marked ‘a’ in Fig. 11.

However, the results for mean  $^{12}\text{CO}$  and  $^{13}\text{CO}$  column densities are indicative of low intrinsic  $^{12}\text{C}/^{13}\text{C}$  ratios in the PN molecular gas. This inference is supported by the low integrated  $\text{H}^{12}\text{CN}/\text{H}^{13}\text{CN}$  and  $\text{H}^{12}\text{CO}^+/\text{H}^{13}\text{CO}^+$  flux ratios we have measured for NGC 6302 and NGC 2440 ( $\sim 3-14$ ; see Table 4), as well as the results of previous single-dish studies of C-bearing isotopologues in molecule-rich PNe, including NGC 2440 (e.g., Ziurys et al. 2020, and references therein). The likelihood of low  $^{12}\text{C}/^{13}\text{C}$  ratios across our sample has interesting implications for the potential common origin and evolution of these PNe; this C isotopic ratio is a potentially sensitive indicator of hot-bottom burning in the more massive progenitors of AGB stars (e.g., Karakas & Lugaro 2016) or binary interactions during the primary star’s post-main sequence evolution (e.g., Khouri et al. 2021, and references therein). According to the models presented in Karakas & Lugaro (2016),  $^{12}\text{C}/^{13}\text{C}$  is predicted to be  $\lesssim 10$  for initial masses in the range  $\sim 4-8 M_\odot$ , with a precipitous drop in  $^{12}\text{C}/^{13}\text{C}$  from  $>40$  to  $<10$  as progenitor mass exceeds  $4 M_\odot$  (or even slightly higher, for super-solar-metallicity progenitors). For reference, the  $^{12}\text{C}/^{13}\text{C}$  isotopic ratio in the local ISM typically ranges from about 40 to 80, while regions of increased stellar density near the Galactic Center exhibit  $^{12}\text{C}/^{13}\text{C}$  ratios in the range  $\sim 15-30$ , with the  $^{13}\text{C}$  enhancement in these regions attributed to the accumulated effects of CN processing in relative massive stars (Wilson & Rood 1994; Halfen et al. 2017; Hily-Blant et al. 2019, and references therein).

However, anomalously low  $^{12}\text{CO}/^{13}\text{CO}$  ratios are also observed in some bipolar pre-PNe that are thought to be descended from relatively low-mass progenitor stars, with the low  $^{12}\text{CO}/^{13}\text{CO}$  ratios in such cases indicative of truncation of AGB evolution via onset of the common envelope stage of an interacting binary system (e.g., Khouri et al. 2021, and references therein). Indeed, while the estimated progenitor masses of sample PNe Hb 5 and NGC 6302 exceed  $\sim 4 M_\odot$  (e.g., Steffen et al. 2013; Kastner et al. 2022, and references therein), the progenitor masses of NGC 2440, NGC 2818, and NGC 2899 have been estimated as  $\lesssim 3 M_\odot$  (Kaler & Jacoby 1989; Miller et al. 2019; Fragkou et al. 2025). Hence — barring the possibility of large  $^{13}\text{CO}(2-1)$  as well as  $^{12}\text{CO}(2-1)$  optical depths — both the ALMA data (i.e., measurements of integrated  $^{12}\text{CO}(2-1)/^{13}\text{CO}(2-1)$  line intensity ratios in the range  $\sim 2-5$ ) and RADEX modeling ( $^{12}\text{CO}/^{13}\text{CO}$  column density ratios near unity) suggest that the PNe in our sample are either descended from relatively massive AGB progenitors (initial masses  $\sim 4-8 M_\odot$ ) or underwent AGB-truncating binary interactions, perhaps via common envelope evolution.

## 7. CONCLUSIONS

We have presented results from extensive mm-wave interferometric molecular line mapping observations of a sample of a half-dozen molecule-rich, high-excitation, bipolar PNe. The data were obtained with the ALMA ACA and 12-meter arrays operating at 1.3 mm (Band 6). The sample we observed with ALMA comprises the PNe Hubble 5, NGC 2440, NGC 6302, NGC 6445, NGC 2818, and NGC 2899. Our primary objective is to gain a deeper understanding of the progenitor systems, shaping histories, and irradiation geometries of these nebulae. In this paper, we have presented the survey data and initial survey results, focusing on the molecular species and transitions detected and the molecular gas kinematics and masses of the sample PNe.

High-quality, subarcsecond-resolution maps of  $^{12}\text{CO}(2-1)$  emission were obtained with the 12-m array for all six of the sample PNe, conclusively demonstrating that the bulk of their molecular gas masses are confined to the central, dusty, pinched waists of these nebulae. We interpret the resulting position-velocity  $^{12}\text{CO}(2-1)$  data cubes as revealing, in each case, the presence of an expanding molecular torus that generally traces the bipolar PN's equatorial plane. These equatorial torus structures range from relatively coherent, for Hb 5, NGC 2440, NGC 6302, and NGC 6445, to highly fragmented, for NGC 2899 and NGC 2818. This apparent evolution of molecular torus structure is consistent with the dynamical age sequence represented by the sample PNe; we infer torus dynamical ages ranging from  $\sim 500$  yr for Hb 5, to a few thousand yr for NGC 2440, NGC 6302, and NGC 6445, to  $\sim 10^4$  yr for NGC 2899 and NGC 2818, respectively (Table 5).

Our results hence demonstrate how, as a molecule-rich bipolar PN evolves, its molecular torus expands and fragments. In the youngest such nebulae, e.g., Hb 5 (and NGC 7027; [Bublitz et al. 2023](#)), the molecular torus forms a nearly continuous, compact structure surrounding the nebular core that lies more or less perpendicular to the optical lobes. Evidently, however, the torus begins to fragment, on a timescale of a few thousand years. This fragmentation process is reflected in the rings of detached, knot-like structures observed in the cores of NGC 2440 and NGC 6445, and in the distortions and azimuthal asymmetries of the NGC 6302 molecular torus. Eventually, the torus becomes highly disrupted, with the molecular gas fragmenting into isolated structures or filaments, as observed in NGC 2899 and NGC 2818.

The ALMA observations of the six sample PNe also yielded detections and maps of CO isotopologues and the trace molecules HCN, HNC,  $\text{HCO}^+$ , CN, CS, and SO, as well as 1.3 mm continuum emission, in some or all of these nebulae (see Table 4). The HCN(3-2), CN(2-1), and  $\text{HCO}^+(3-2)$  transitions are detected in all sample PNe observed (the only exception being NGC 6445, for which no HCN or  $\text{HCO}^+$  data were obtained), while HNC(3-2) is detected in all PNe except Hb 5. Emission from CS(5-4) is detected in NGC 6302, NGC 6445, and NGC 2818. Lines of SO covered in our spectrometer setups are detected only in NGC 2440 and NGC 6302. Emission from  $\text{CO}^+(2-1)$  was not detected from any of the four nebulae for which the ALMA data included coverage of this line, leaving NGC 7027 as the only PN detected to date in  $\text{CO}^+$  ([Bublitz et al. 2023](#), and references therein). Bright, compact 1.3 mm continuum emission is detected in Hb 5, NGC 2440, and NGC 6302, while weak continuum emission is detected in NGC 6445. In a subsequent paper, we investigate the molecular chemistries of the PNe as revealed by molecular line ratio images and line ratio diagnostic diagrams, focusing on the potential effects of UV and X-ray irradiation of PN molecular gas by the hot, luminous central stars powering these nebulae and the impacts of fast stellar winds.

We analyzed the  $^{12}\text{CO}(2-1)$  and  $^{13}\text{CO}(2-1)$  emission-line data cubes to obtain estimates for  $^{12}\text{CO}$  and  $^{13}\text{CO}$  column densities and, hence, the total masses of molecular gas in these nebulae, under an assumed  $^{12}\text{CO}:\text{H}_2$  ratio of  $10^{-4}$  and an assumed  $^{13}\text{CO}:\text{H}_2$  ratio of  $10^{-5}$ . The resulting molecular mass estimates for our target PNe lie in the range  $\sim 0.002 - 0.09 M_\odot$  (§6). Interestingly, there is no clear correlation of the estimated PN molecular masses with the inferred torus dynamical ages. This lack of dependence of PN molecular mass on age suggests that the molecular mass of a PN is determined by its progenitor system properties, rather than by its UV irradiation (hence molecular dissociation) history. The low measured  $^{12}\text{CO}/^{13}\text{CO}$  integrated flux ratios and resulting low inferred  $^{12}\text{CO}/^{13}\text{CO}$  column density ratios, in addition to suggesting large  $^{12}\text{CO}$  opacities, likely reflect intrinsically low  $^{12}\text{C}/^{13}\text{C}$  isotopic ratios. Such low C isotopic ratios, in turn, would suggest that the progenitor masses

of our sample PNe generally lie in the range  $\sim 4\text{--}8 M_{\odot}$  and/or that the central stars of these PNe reside in interacting binary systems (§ 6.2).

This ALMA molecular line mapping study of a sample of high-excitation, molecule-rich, bipolar PNe hence well illustrates how the presence and evolution of molecular gas in a PN is inextricably linked to its progenitor star system as well as the resultant nebula’s formation and structural evolution. Our analysis bolsters the assertion (Huggins 2007) that ejection of a dense equatorial torus precedes the onset of the collimated polar outflows (jets) that, along with large molecular gas masses, represent the defining characteristics of the class of extreme bi-lobed PNe. The sequential nature of the formation of torus and lobes (§ 5.3), along with the multi-polar, episodic polar ejections observed in optical emission-line imaging, are indicative of mass loss processes far more complex than can be explained via single-star AGB and post-AGB models (see, e.g., Höfner & Olofsson 2018, and references therein), adding to the evidence for the presence of interacting binary companions at the cores of the sample PNe.

Our results further demonstrate that the high CSPN  $T_{\text{eff}}$  and  $L_{\text{bol}}$  of molecule-rich bipolar PNe are maintained over  $\sim 10\text{--}20$  kyr timescales, post-AGB; such timescales far exceed expected post-AGB core cooling times (e.g., Miller Bertolami 2016). Perhaps mass accretion at the central stars and/or companion stars in these systems is both sustaining their intense UV fields and driving polar flows well into post-AGB evolution. Such a long-timescale yet episodic accretion/outflow process, along with the delay we and others have deduced between the formation of the molecular tori and optical lobes of extreme bi-lobed PNe, appears consistent with a model of bipolar PN formation via Intermediate-Luminosity Optical Transient (ILOT) events (Soker & Kashi 2012). This model offers an explanation for the formation of bi-lobed PNe that display evidence for multiple, paired mass ejections. Such a model, which has been considered to explain the formation and structural evolution of NGC 6302 (Soker & Kashi 2012; Kastner et al. 2022), is worth exploring in more detail for the other PNe in our ALMA survey sample.

#### ACKNOWLEDGMENTS

The authors thank Letizia Stanghellini and the anonymous referee for their many valuable comments, which greatly improved this paper. Major support for the work of PMB and JHK on mm-wave interferometric mapping of molecular line emission from planetary nebulae has been provided by NSF grant AST-2206033 to RIT. JA and MSG acknowledge the financial support of I+D+i projects PID2019-105203GB-C21 and PID2023-146056NB-C21, funded by the Spanish MCIN/AEI/10.13039/501100011033 and EU/ERDF. This paper makes use of ALMA data from programs 2021.1.00456.S, 2021.2.00004.S, and 2022.1.00401.S (PI: J. Kastner). ALMA is a partnership of ESO (representing its member states), NSF (USA) and NINS (Japan), together with NRC (Canada), NSTC and ASIAA (Taiwan), and KASI (Republic of Korea), in cooperation with the Republic of Chile. The Joint ALMA Observatory is operated by ESO, AUI/NRAO and NAOJ. The National Radio Astronomy Observatory is a facility of the National Science Foundation operated under cooperative agreement by Associated Universities, Inc.

#### REFERENCES

Aleman, I., Ueta, T., Ladjal, D., et al. 2014, *A&A*, 566, A79, doi: [10.1051/0004-6361/201322940](https://doi.org/10.1051/0004-6361/201322940)

- Aller, L. H., Czyzak, S. J., Craine, E., & Kaler, J. B. 1973, *ApJ*, 182, 509, doi: [10.1086/152158](https://doi.org/10.1086/152158)
- Aller, L. H., Ross, J. E., Omara, B. J., & Keyes, C. D. 1981, *MNRAS*, 197, 95, doi: [10.1093/mnras/197.1.95](https://doi.org/10.1093/mnras/197.1.95)
- Ashley, M. C. B., & Hyland, A. R. 1988, *ApJ*, 331, 532, doi: [10.1086/166578](https://doi.org/10.1086/166578)
- Bachiller, R., Forveille, T., Huggins, P. J., & Cox, P. 1997, *A&A*, 324, 1123
- Baessgen, M., Diesch, C., & Grewing, M. 1995, *A&A*, 297, 828
- Bailer-Jones, C. A. L., Rybizki, J., Founesneau, M., Demleitner, M., & Andrae, R. 2021, *AJ*, 161, 147, doi: [10.3847/1538-3881/abd806](https://doi.org/10.3847/1538-3881/abd806)
- Balick, B. 1987, *AJ*, 94, 671, doi: [10.1086/114504](https://doi.org/10.1086/114504)
- Balick, B., Borcherdt, L., Kastner, J. H., et al. 2023, *ApJ*, 957, 54, doi: [10.3847/1538-4357/acf5ea](https://doi.org/10.3847/1538-4357/acf5ea)
- Balick, B., & Frank, A. 2002, *Annual Review of Astronomy and Astrophysics*, 40, 439, doi: [10.1146/annurev.astro.40.060401.093849](https://doi.org/10.1146/annurev.astro.40.060401.093849)
- Bernard-Salas, J., & Tielens, A. G. G. M. 2005, *A&A*, 431, 523, doi: [10.1051/0004-6361:20035746](https://doi.org/10.1051/0004-6361:20035746)
- Bohuski, T. J., & Smith, M. G. 1974, *ApJ*, 193, 197, doi: [10.1086/153147](https://doi.org/10.1086/153147)
- Bonatto, C., Bica, E., & Santos, J. F. C. 2008, *MNRAS*, 386, 324, doi: [10.1111/j.1365-2966.2008.13042.x](https://doi.org/10.1111/j.1365-2966.2008.13042.x)
- Bublitz, J., Kastner, J. H., Hily-Blant, P., et al. 2022, *A&A*, 659, A197, doi: [10.1051/0004-6361/202141778](https://doi.org/10.1051/0004-6361/202141778)
- Bublitz, J., Kastner, J. H., Santander-García, M., et al. 2019, *A&A*, 625, A101, doi: [10.1051/0004-6361/201834408](https://doi.org/10.1051/0004-6361/201834408)
- Bublitz, J., Kastner, J. H., Hily-Blant, P., et al. 2023, *ApJ*, submitted
- Bucciarelli, B., & Stanghellini, L. 2023, *A&A*, 680, A104, doi: [10.1051/0004-6361/202347519](https://doi.org/10.1051/0004-6361/202347519)
- CASA Team, Bean, B., Bhatnagar, S., et al. 2022, *PASP*, 134, 114501, doi: [10.1088/1538-3873/ac9642](https://doi.org/10.1088/1538-3873/ac9642)
- Casassus, S., Roche, P. F., & Barlow, M. J. 2000, *MNRAS*, 314, 657, doi: [10.1046/j.1365-8711.2000.03208.x](https://doi.org/10.1046/j.1365-8711.2000.03208.x)
- Corradi, R. L. M., & Schwarz, H. E. 1993, *A&A*, 269, 462
- Corradi, R. L. M., & Schwarz, H. E. 1995, *A&A*, 293, 871
- Cortes, P. C., ed. 2024, *ALMA Cycle 11 Technical Handbook*.  
<https://almascience.nrao.edu/documents-and-tools/cycle11/alma-technical-handbook>
- Cox, P., Omont, A., Huggins, P. J., Bachiller, R., & Forveille, T. 1992, *A&A*, 266, 420
- Cuesta, L., & Phillips, J. P. 1999, *AJ*, 117, 974, doi: [10.1086/300746](https://doi.org/10.1086/300746)
- Daub, C. T. 1982, *ApJ*, 260, 612, doi: [10.1086/160283](https://doi.org/10.1086/160283)
- Dayal, A., & Bieging, J. H. 1996, *ApJ*, 472, 703, doi: [10.1086/178100](https://doi.org/10.1086/178100)
- De Marco, O., & Izzard, R. G. 2017, *Publications of the Astronomical Society of Australia*, 34, doi: [10.1017/pasa.2016.52](https://doi.org/10.1017/pasa.2016.52)
- Deguchi, S., Izumiura, H., Kaifu, N., et al. 1990, *ApJ*, 351, 522, doi: [10.1086/168490](https://doi.org/10.1086/168490)
- Derlopa, S., Akras, S., Amram, P., et al. 2024, *MNRAS*, 530, 3327, doi: [10.1093/mnras/stae1013](https://doi.org/10.1093/mnras/stae1013)
- Dinh-V-Trung, Bujarrabal, V., Castro-Carrizo, A., Lim, J., & Kwok, S. 2008a, *ApJ*, 673, 934, doi: [10.1086/524373](https://doi.org/10.1086/524373)
- Dinh-V-Trung, Bujarrabal, V., Castro-Carrizo, A., Lim, J., & Kwok, S. 2008b, *ApJ*, 673, 934, doi: [10.1086/524373](https://doi.org/10.1086/524373)
- Drew, J. E., Gonzalez-Solares, E., Greimel, R., et al. 2014, *MNRAS*, 440, 2036, doi: [10.1093/mnras/stu394](https://doi.org/10.1093/mnras/stu394)
- Dufour, R. J. 1984, *ApJ*, 287, 341, doi: [10.1086/162694](https://doi.org/10.1086/162694)
- Edwards, J. L., Cox, E. G., & Ziurys, L. M. 2014, *ApJ*, 791, 79, doi: [10.1088/0004-637X/791/2/79](https://doi.org/10.1088/0004-637X/791/2/79)
- Edwards, J. L., & Ziurys, L. M. 2013, *ApJL*, 770, L5, doi: [10.1088/2041-8205/770/1/L5](https://doi.org/10.1088/2041-8205/770/1/L5)
- Fang, X., Zhang, Y., Kwok, S., et al. 2018, *The Astrophysical Journal*, 859, 92, doi: [10.3847/1538-4357/aac01e](https://doi.org/10.3847/1538-4357/aac01e)
- Fragkou, V., Vázquez, R., Parker, Q. A., Gonçalves, D. R., & Lomelí-Núñez, L. 2025, arXiv e-prints, arXiv:2503.19287, doi: [10.48550/arXiv.2503.19287](https://doi.org/10.48550/arXiv.2503.19287)
- Freeman, M., Montez, R., J., Kastner, J. H., et al. 2014, *ApJ*, 794, 99, doi: [10.1088/0004-637X/794/2/99](https://doi.org/10.1088/0004-637X/794/2/99)
- Frew, D. J., Parker, Q. A., & Bojičić, I. S. 2016, *MNRAS*, 455, 1459, doi: [10.1093/mnras/stv1516](https://doi.org/10.1093/mnras/stv1516)
- García-Segura, G., Ricker, P. M., & Taam, R. E. 2018, *ApJ*, 860, 19, doi: [10.3847/1538-4357/aac08c](https://doi.org/10.3847/1538-4357/aac08c)
- Gómez-Gordillo, S., Akras, S., Gonçalves, D. R., & Steffen, W. 2020, *MNRAS*, 492, 4097, doi: [10.1093/mnras/staa060](https://doi.org/10.1093/mnras/staa060)

- Gorny, S. K., Stasińska, G., & Tylenda, R. 1997, *A&A*, 318, 256
- Greig, W. E. 1972, *A&A*, 18, 70
- Halfen, D. T., Woolf, N. J., & Ziurys, L. M. 2017, *ApJ*, 845, 158, doi: [10.3847/1538-4357/aa816b](https://doi.org/10.3847/1538-4357/aa816b)
- Healy, A. P., & Huggins, P. J. 1990, *AJ*, 100, 511, doi: [10.1086/115532](https://doi.org/10.1086/115532)
- Henry, R. B. C., Stephenson, B. G., Miller Bertolami, M. M., Kwitter, K. B., & Balick, B. 2018, *MNRAS*, 473, 241, doi: [10.1093/mnras/stx2286](https://doi.org/10.1093/mnras/stx2286)
- Hily-Blant, P., Magalhaes de Souza, V., Kastner, J., & Forveille, T. 2019, *A&A*, 632, L12, doi: [10.1051/0004-6361/201936750](https://doi.org/10.1051/0004-6361/201936750)
- Höfner, S., & Olofsson, H. 2018, *A&A Rv*, 26, 1, doi: [10.1007/s00159-017-0106-5](https://doi.org/10.1007/s00159-017-0106-5)
- Huggins, P. J. 2007, *ApJ*, 663, 342, doi: [10.1086/518415](https://doi.org/10.1086/518415)
- Huggins, P. J., Bachiller, R., Cox, P., & Forveille, T. 1996, *A&A*, 315, 284
- Huggins, P. J., Bachiller, R., Planesas, P., Forveille, T., & Cox, P. 2005, *ApJS*, 160, 272, doi: [10.1086/432668](https://doi.org/10.1086/432668)
- Huggins, P. J., Forveille, T., Bachiller, R., & Cox, P. 2000, *ApJ*, 544, 889, doi: [10.1086/317240](https://doi.org/10.1086/317240)
- Huggins, P. J., & Healy, A. P. 1989, *ApJ*, 346, 201, doi: [10.1086/168001](https://doi.org/10.1086/168001)
- Kaler, J. B., & Jacoby, G. H. 1989, *ApJ*, 345, 871, doi: [10.1086/167957](https://doi.org/10.1086/167957)
- Karakas, A. I., & Lugaro, M. 2016, *ApJ*, 825, 26, doi: [10.3847/0004-637X/825/1/26](https://doi.org/10.3847/0004-637X/825/1/26)
- Kastner, J. H., Moraga Baez, P., Balick, B., et al. 2022, *ApJ*, 927, 100, doi: [10.3847/1538-4357/ac51cd](https://doi.org/10.3847/1538-4357/ac51cd)
- Kastner, J. H., Moraga Baez, P., Balick, B., et al. 2025a, *ApJ*, 993, 79, doi: [10.3847/1538-4357/ae0706](https://doi.org/10.3847/1538-4357/ae0706)
- Kastner, J. H., Weintraub, D. A., Gatley, I., Merrill, K. M., & Probst, R. G. 1996, *ApJ*, 462, 777, doi: [10.1086/177192](https://doi.org/10.1086/177192)
- Kastner, J. H., Wilner, D. J., Moraga Baez, P., et al. 2024, *ApJ*, 965, 21, doi: [10.3847/1538-4357/ad2848](https://doi.org/10.3847/1538-4357/ad2848)
- Kastner, J. H., Wilner, D. J., Ryder, D., et al. 2025b, *ApJ*, 981, 46, doi: [10.3847/1538-4357/adace1](https://doi.org/10.3847/1538-4357/adace1)
- Kastner, J. H., Montez, R., J., Balick, B., et al. 2012, *AJ*, 144, 58, doi: [10.1088/0004-6256/144/2/58](https://doi.org/10.1088/0004-6256/144/2/58)
- Kemper, F., Molster, F. J., Jäger, C., & Waters, L. B. F. M. 2002, *A&A*, 394, 679, doi: [10.1051/0004-6361:20021119](https://doi.org/10.1051/0004-6361:20021119)
- Khoury, T., Vlemmings, W. H. T., Tafuya, D., et al. 2021, *Nature Astronomy*, 6, 275, doi: [10.1038/s41550-021-01528-4](https://doi.org/10.1038/s41550-021-01528-4)
- Kohoutek, L., Roth-Hoepfner, M. L., & Laustsen, S. 1986, *A&A*, 162, 232
- Kwok, S., Purton, C. R., & Fitzgerald, P. M. 1978, *ApJL*, 219, L125, doi: [10.1086/182621](https://doi.org/10.1086/182621)
- Lago, P. J. A., & Costa, R. D. D. 2016, *RMxAA*, 52, 329, doi: [10.48550/arXiv.1606.01234](https://doi.org/10.48550/arXiv.1606.01234)
- Lago, P. J. A., Costa, R. D. D., Faúndez-Abans, M., & Maciel, W. J. 2019, *MNRAS*, 489, 2923, doi: [10.1093/mnras/stz2319](https://doi.org/10.1093/mnras/stz2319)
- Lopez, J. A., Falcon, L. H., Ruiz, M. T., & Roth, M. 1991, *A&A*, 241, 526
- López, J. A., García-Díaz, M. T., Steffen, W., Riesgo, H., & Richer, M. G. 2012, *ApJ*, 750, 131, doi: [10.1088/0004-637X/750/2/131](https://doi.org/10.1088/0004-637X/750/2/131)
- López, J. A., Meaburn, J., Bryce, M., & Holloway, A. J. 1998, *ApJ*, 493, 803, doi: [10.1086/305155](https://doi.org/10.1086/305155)
- Mata, H., Ramos-Larios, G., Guerrero, M. A., et al. 2016, *MNRAS*, 459, 841, doi: [10.1093/mnras/stw646](https://doi.org/10.1093/mnras/stw646)
- Meaburn, J., Lloyd, M., Vaytet, N. M. H., & López, J. A. 2008, *MNRAS*, 385, 269, doi: [10.1111/j.1365-2966.2007.12782.x](https://doi.org/10.1111/j.1365-2966.2007.12782.x)
- Meaburn, J., López, J. A., Steffen, W., Graham, M. F., & Holloway, A. J. 2005, *AJ*, 130, 2303, doi: [10.1086/496978](https://doi.org/10.1086/496978)
- Miller, T. R., Henry, R. B. C., Balick, B., et al. 2019, *MNRAS*, 482, 278, doi: [10.1093/mnras/sty2517](https://doi.org/10.1093/mnras/sty2517)
- Miller Bertolami, M. M. 2016, *A&A*, 588, A25, doi: [10.1051/0004-6361/201526577](https://doi.org/10.1051/0004-6361/201526577)
- Molster, F. J., Lim, T. L., Sylvester, R. J., et al. 2001, *A&A*, 372, 165, doi: [10.1051/0004-6361:20010465](https://doi.org/10.1051/0004-6361:20010465)
- Montez, R., J., Kastner, J. H., Balick, B., et al. 2015, *ApJ*, 800, 8, doi: [10.1088/0004-637X/800/1/8](https://doi.org/10.1088/0004-637X/800/1/8)
- Montez, Rodolfo, J., Kastner, J. H., Balick, B., & Frank, A. 2009, *ApJ*, 694, 1481, doi: [10.1088/0004-637X/694/2/1481](https://doi.org/10.1088/0004-637X/694/2/1481)
- Moraga Baez, P., Kastner, J. H., Balick, B., Montez, R., & Bublitz, J. 2023, *ApJ*, 942, 15, doi: [10.3847/1538-4357/aca401](https://doi.org/10.3847/1538-4357/aca401)

- Ortiz, R., Copetti, M. V. F., & Lorenz-Martins, S. 2011, *MNRAS*, 418, 2004,  
doi: [10.1111/j.1365-2966.2011.19619.x](https://doi.org/10.1111/j.1365-2966.2011.19619.x)
- Peretto, N., Fuller, G., Zijlstra, A., & Patel, N. 2007, *A&A*, 473, 207, doi: [10.1051/0004-6361:20066973](https://doi.org/10.1051/0004-6361:20066973)
- Phillips, J. P., & Mampaso, A. 1988, *A&A*, 190, 237
- Poggio, E., Drimmel, R., Cantat-Gaudin, T., et al. 2021, *A&A*, 651, A104,  
doi: [10.1051/0004-6361/202140687](https://doi.org/10.1051/0004-6361/202140687)
- Pottasch, S. R., & Surendiranath, R. 2007, *A&A*, 462, 179, doi: [10.1051/0004-6361:20066012](https://doi.org/10.1051/0004-6361:20066012)
- Pottasch, S. R., Baud, B., Beintema, D., et al. 1984, *A&A*, 138, 10
- Rani, S., Pandey, G., Subramaniam, A., & Rao, N. K. 2023, *ApJ*, 945, 11, doi: [10.3847/1538-4357/acb0c8](https://doi.org/10.3847/1538-4357/acb0c8)
- Rauch, T., Köppen, J., Napiwotzki, R., & Werner, K. 1999, *A&A*, 347, 169
- Sabbadin, F. 1986, *A&AS*, 64, 579
- Santander-García, M., Bujarrabal, V., Alcolea, J., et al. 2017, *A&A*, 597, A27,  
doi: [10.1051/0004-6361/201629288](https://doi.org/10.1051/0004-6361/201629288)
- Schmidt, D. R., Gold, K. R., Sinclair, A., Bergstrom, S., & Ziurys, L. M. 2022, *ApJ*, 927, 46,  
doi: [10.3847/1538-4357/ac4474](https://doi.org/10.3847/1538-4357/ac4474)
- Schmidt, D. R., & Ziurys, L. M. 2016, *ApJ*, 817, 175, doi: [10.3847/0004-637X/817/2/175](https://doi.org/10.3847/0004-637X/817/2/175)
- Schmidt, D. R., & Ziurys, L. M. 2017a, *ApJ*, 835, 79, doi: [10.3847/1538-4357/835/1/79](https://doi.org/10.3847/1538-4357/835/1/79)
- Schmidt, D. R., & Ziurys, L. M. 2017b, *ApJ*, 850, 123, doi: [10.3847/1538-4357/aa8a6a](https://doi.org/10.3847/1538-4357/aa8a6a)
- Schwarz, H. E., Corradi, R. L. M., & Melnick, J. 1992, *A&AS*, 96, 23
- Schwarz, H. E., Monteiro, H., & Peterson, R. 2008, *ApJ*, 675, 380, doi: [10.1086/524094](https://doi.org/10.1086/524094)
- Soker, N., & Kashi, A. 2012, *ApJ*, 746, 100, doi: [10.1088/0004-637X/746/1/100](https://doi.org/10.1088/0004-637X/746/1/100)
- Stanghellini, L., & Haywood, M. 2010, *ApJ*, 714, 1096, doi: [10.1088/0004-637X/714/2/1096](https://doi.org/10.1088/0004-637X/714/2/1096)
- Stanghellini, L., Shaw, R. A., & Villaver, E. 2008, *ApJ*, 689, 194, doi: [10.1086/592395](https://doi.org/10.1086/592395)
- Steffen, W., Koning, N., Esquivel, A., et al. 2013, *MNRAS*, 436, 470, doi: [10.1093/mnras/stt1583](https://doi.org/10.1093/mnras/stt1583)
- Szyszkla, C., Zijlstra, A. A., & Walsh, J. R. 2011, *MNRAS*, 416, 715, doi: [10.1111/j.1365-2966.2011.19087.x](https://doi.org/10.1111/j.1365-2966.2011.19087.x)
- Tifft, W. G., Connolly, L. P., & Webb, D. F. 1972, *MNRAS*, 158, 47, doi: [10.1093/mnras/158.1.47](https://doi.org/10.1093/mnras/158.1.47)
- van der Tak, F. F. S., Black, J. H., Schöier, F. L., Jansen, D. J., & van Dishoeck, E. F. 2007, *A&A*, 468, 627, doi: [10.1051/0004-6361:20066820](https://doi.org/10.1051/0004-6361:20066820)
- van Hoof, P. A. M., Van de Steene, G. C., Beintema, D. A., et al. 2000, *ApJ*, 532, 384, doi: [10.1086/308536](https://doi.org/10.1086/308536)
- Vázquez, R. 2012, *ApJ*, 751, 116, doi: [10.1088/0004-637X/751/2/116](https://doi.org/10.1088/0004-637X/751/2/116)
- Wang, M.-Y., Hasegawa, T. I., & Kwok, S. 2008, *ApJ*, 673, 264, doi: [10.1086/524185](https://doi.org/10.1086/524185)
- Wilson, T. L., & Rood, R. 1994, *ARA&A*, 32, 191, doi: [10.1146/annurev.aa.32.090194.001203](https://doi.org/10.1146/annurev.aa.32.090194.001203)
- Wolff, M. J., Code, A. D., & Groth, E. J. 2000, *AJ*, 119, 302, doi: [10.1086/301169](https://doi.org/10.1086/301169)
- Wright, N. J., Barlow, M. J., Ercolano, B., & Rauch, T. 2011, *MNRAS*, 418, 370,  
doi: [10.1111/j.1365-2966.2011.19490.x](https://doi.org/10.1111/j.1365-2966.2011.19490.x)
- Young, K., Cox, P., Huggins, P. J., Forveille, T., & Bachiller, R. 1999, *ApJ*, 522, 387, doi: [10.1086/307639](https://doi.org/10.1086/307639)
- Zhang, Y., Kwok, S., & Dinh-V-Trung. 2008, *ApJ*, 678, 328, doi: [10.1086/529428](https://doi.org/10.1086/529428)
- Ziurys, L. M., Schmidt, D. R., & Woolf, N. J. 2020, *ApJL*, 900, L31, doi: [10.3847/2041-8213/abb082](https://doi.org/10.3847/2041-8213/abb082)
- Zweigle, J., Neri, R., Bachiller, R., Bujarrabal, V., & Grewing, M. 1997, *A&A*, 324, 624

## APPENDIX

## A. ALMA BAND 6 OBSERVATIONS: MOLECULES DETECTED

Tables 7–12 present compilations of results for molecular lines detected in each PN.

**Table 7.** DETECTED MOLECULAR TRANSITIONS

PN G	Name	ALMA Config.	Molecule	QN	$\nu$ (GHz)	$\log A_{ul}$ (s <sup>-1</sup> )	$E_u/k$ (K)	$I$ ( $\sigma_I^a$ ) (Jy km s <sup>-1</sup> )	$V_{LSR}$ (km s <sup>-1</sup> )	$\Delta V_{1/2}$ (km s <sup>-1</sup> )
359.3-00.9	PN Hb 5	ACA	<sup>12</sup> CO	$J = 2 - 1$	230.538	-6.1605	16.5961	360.709 (1.053) <sup>c</sup>	-10.777	53.022
			<b>CN</b>	$N = 2 - 1^b$	<b>226.697</b>	<b>-4.2783</b>	<b>16.3089</b>	<b>118.239 (1.044)</b>	<b>-5.028</b>	<b>49.081</b>
				$N = 2 - 1^b$	<b>226.874</b>	<b>-3.9419</b>	<b>16.3349</b>	<b>279.184 (0.931)</b>	<b>-2.136</b>	<b>44.237</b>
			HCN	$J = 3 - 2$	265.886	-3.0780	25.5209	101.701 (0.302)	-9.529	46.657
			HCO <sup>+</sup>	$J = 3 - 2$	267.557	-2.8376	25.6817	140.549 (0.696)	-9.583	49.596
		C43-1	<sup>12</sup> CO	$J = 2 - 1$	230.538	-6.1605	16.5961	517.688 (1.053)	-22.211	55.562
			<b>CN</b>	$N = 2 - 1^b$	<b>226.697</b>	<b>-4.2783</b>	<b>16.3089</b>	<b>90.101(1.044)</b>	<b>-0.922</b>	<b>45.918</b>
				$N = 2 - 1^b$	<b>226.874</b>	<b>-3.9419</b>	<b>16.3349</b>	<b>222.419(0.931)</b>	<b>-3.702</b>	<b>46.210</b>
			<b>H<sup>13</sup>CO<sup>+</sup></b>	$N = 3 - 2$	<b>260.255</b>	<b>-2.8737</b>	<b>24.9807</b>	<b>4.529 (0.050)</b>	<b>-0.256</b>	<b>15.124</b>

NOTES: New molecule detections are denoted by bold font. a) Integrated line flux within 8'' x 8'' synthetic beam centered on (17:44:43.970, -29:58:39.709) position. b) Hyperfine complex; representative transition frequency,  $A_{ul}$ , and upper level energy listed retrieved from CDMS. c) The ACA observation of <sup>12</sup>CO reflects flux loss due to continuum subtraction errors that occurred during the pipeline cleaning process.

**Table 8.** NGC 2440: DETECTED MOLECULAR TRANSITIONS

ALMA Config.	Molecule	QN	$\nu$ (GHz)	$\log A_{ul}$ ( $s^{-1}$ )	$E_u/k$ (K)	$I^a$ ( $\sigma_I$ ) (Jy km s $^{-1}$ )	$V_{LSR}$ (km s $^{-1}$ )	$\Delta V_{1/2}$ (km s $^{-1}$ )
ACA	$^{12}\text{CO}$	$J = 2 - 1$	230.538	-6.1605	16.5961	93.656 (0.872)	40.235	28.485
	$^{13}\text{CO}$	$N = 2 - 1$	220.398	-6.2164	15.8662	44.422 (0.391)	38.138	30.225
	<b>CN</b>	$N = 2 - 1^b$	<b>226.697</b>	<b>-4.2783</b>	<b>16.3089</b>	<b>22.484 (1.150)</b>	<b>55.195</b>	<b>12.272</b>
		$N = 2 - 1^b$	<b>226.874</b>	<b>-3.9419</b>	<b>16.3349</b>	<b>57.031 (0.868)</b>	<b>42.410</b>	<b>29.040</b>
	HCN	$J = 3 - 2$	265.886	-3.0780	25.5209	22.935 (0.629)	44.828	23.264
	H $^{13}\text{CN}$	$J = 3 - 2$	259.011	-3.1121	24.8616	7.993 (0.653)	41.750	19.200
	<b>HNC</b>	<b><math>J = 3 - 2</math></b>	<b>271.981</b>	<b>-3.0298</b>	<b>26.1069</b>	<b>8.056 (0.606)</b>	<b>41.202</b>	<b>18.842</b>
	HCO $^+$	$J = 3 - 2$	267.557	-2.8376	25.6817	10.357 (0.887)	42.634	20.793
C43-3	$^{13}\text{CO}$	$N = 2 - 1$	220.398	-6.2164	15.8662	9.501 (0.206)	41.881	40.851
	HCN	$J = 3 - 2$	265.886	-3.0780	25.5209	25.143 (0.290)	43.556	38.402
	H $^{13}\text{CN}$	$N = 3 - 2$	259.011	-3.1121	24.8616	9.736 (0.294)	42.604	20.571
	<b>HNC</b>	<b><math>J = 3 - 2</math></b>	<b>271.981</b>	<b>-3.0298</b>	<b>26.1069</b>	<b>0.042 (0.00788)</b>	<b>38.918</b>	<b>24.220</b>
	HCO $^+$	$J = 3 - 2$	267.557	-2.8376	25.6817	9.247 (0.409)	42.690	28.520
	<b>H<math>^{13}\text{CO}^+</math></b>	<b><math>N = 3 - 2</math></b>	<b>260.255</b>	<b>-2.8737</b>	<b>24.9807</b>	<b>2.298 (0.196)</b>	<b>39.125</b>	<b>16.242</b>
C43-4	<b>SO</b>	<b><math>N_J = 6_5 - 5_4^b</math></b>	<b>219.949</b>	<b>-3.8744</b>	<b>16.9790</b>	<b>1.775 (0.163)</b>	<b>52.990</b>	<b>10.650</b>
	$^{12}\text{CO}$	$J = 2 - 1$	230.538	-6.1605	16.5961	104.282 (0.525)	42.059	40.957
	<b>CN</b>	$N = 2 - 1^b$	<b>226.697</b>	<b>-4.2783</b>	<b>16.3089</b>	<b>20.843 (0.483)</b>	<b>38.790</b>	<b>37.137</b>
$N = 2 - 1^b$		<b>226.874</b>	<b>-3.9419</b>	<b>16.3349</b>	<b>50.520 (0.526)</b>	<b>41.516</b>	<b>40.974</b>	

NOTES: New molecule detections are denoted by bold font. a) Integrated line flux within a  $9'' \times 14''$  synthetic beam centered on (7:39:41.414, -18:05:24.739) position for the central torus and a  $5'' \times 5''$  synthetic beam centered on the NE and SW lobes (ACA data). b) Hyperfine complex; representative transition frequency,  $A_{ul}$ , and upper level energy listed retrieved from CDMS.

**Table 9.** NGC 6302: DETECTED MOLECULAR TRANSITIONS

ALMA Config.	Molecule	QN	$\nu$ (GHz)	$\log A_{ul}$ ( $s^{-1}$ )	$E_u/k$ (K)	$I^a$ ( $\sigma_I$ ) (Jy km s $^{-1}$ )	$V_{LSR}$ (km s $^{-1}$ )	$\Delta V_{1/2}$ (km s $^{-1}$ )	
ACA	$^{12}\text{CO}$	$J = 2 - 1$	230.538	-6.1605	16.5961	802.263 (0.805)	-40.622	27.302	
	<b>CS</b>	$N = 5 - 4$	<b>244.936</b>	<b>-3.5257</b>	<b>35.2660</b>	<b>14.338 (0.866)</b>	<b>-38.120</b>	<b>2.988</b>	
	<b>C<math>^{34}\text{S}</math></b>	$N = 5 - 4$	<b>241.016</b>	<b>-3.5467</b>	<b>27.7763</b>	<b>3.054 (0.660)</b>	<b>-39.076</b>	<b>3.644</b>	
	CN	$N = 2 - 1^b$	226.697	-4.2783	16.3089	36.676 (0.618)	-28.600	34.2265	
		$N = 2 - 1^b$	226.874	-3.9419	16.3349	79.996 (0.738)	-38.211	24.217	
	<b>H<math>^{13}\text{CN}</math></b>	$J = 3 - 2$	<b>259.011</b>	<b>-3.1121</b>	<b>24.8616</b>	<b>17.766 (0.413)</b>	<b>-30.4065</b>	<b>10.9515</b>	
	<b>HNC</b>	$J = 3 - 2$	<b>271.981</b>	<b>-3.0298</b>	<b>26.1069</b>	<b>23.545 (0.696)</b>	<b>-30.967</b>	<b>13.455</b>	
	<b>H<math>^{13}\text{CO}^+</math></b>	$N = 3 - 2$	<b>260.255</b>	<b>-2.8737</b>	<b>24.9807</b>	<b>9.844 (0.434)</b>	<b>-38.586</b>	<b>3.1645</b>	
	C43-1	$^{13}\text{CO}$	$N = 2 - 1$	220.398	-6.2164	15.8662	286.858 (0.363)	-40.898	30.886
		<b>C<math>^{18}\text{O}</math></b>	$J = 2 - 1$	<b>219.560</b>	<b>-6.2210</b>	<b>15.8058</b>	<b>5.813 (0.104)</b>	<b>-32.304</b>	<b>13.002</b>
SO		$N_J = 6_5 - 5_4^b$	219.949	-3.8744	16.9790	6.343 (0.0955)	-30.668	11.314	
<b>H30<math>\alpha</math></b>		...	<b>231.901</b>	...	...	<b>25.827 (0.235)</b>	...	...	
C43-3	HCN	$J = 3 - 2$	265.886	-3.0780	25.5209	97.156 (0.477)	-34.122	18.995	
	<b>H<math>^{13}\text{CN}</math></b>	$J = 3 - 2$	<b>259.011</b>	<b>-3.1121</b>	<b>24.8616</b>	<b>23.432 (0.547)</b>	<b>-29.976</b>	<b>11.517</b>	
	<b>HNC</b>	$J = 3 - 2$	<b>271.981</b>	<b>-3.0298</b>	<b>26.1069</b>	<b>19.634 (0.500)</b>	<b>-30.262</b>	<b>22.069</b>	
	HCO $^+$	$J = 3 - 2$	267.557	-2.8376	25.6817	140.159 (0.963)	-31.180	24.349	
	<b>H<math>^{13}\text{CO}^+</math></b>	$N = 3 - 2$	<b>260.255</b>	<b>-2.8737</b>	<b>24.9807</b>	<b>11.111 (0.661)</b>	<b>-37.251</b>	<b>4.852</b>	
SO	$N_J = 5_6 - 4_5^b$	251.857	-3.6737	26.8110	0.377 (0.268)	-37.160	2.906		
	$N_J = 6_5 - 5_4^b$	219.949	-3.8744	16.9790	4.556 (0.302)	-38.130	11.002		
C43-4	$^{12}\text{CO}$	$J = 2 - 1$	230.538	-6.1605	16.5961	818.523 (0.442)	-38.885	30.799	
	$^{13}\text{CO}$	$N = 2 - 1$	220.398	-6.2164	15.8662	262.820 (0.412)	-39.927	27.898	
	<b>C<math>^{18}\text{O}</math></b>	$J = 2 - 1$	<b>219.560</b>	<b>-6.2210</b>	<b>15.8058</b>	<b>2.545 (0.185)</b>	<b>-32.326</b>	<b>13.002</b>	
	CN	$N = 2 - 1^b$	226.697	-4.2783	16.3089	15.674 (0.413)	-32.632	20.991	
$N = 2 - 1^b$		226.874	-3.9419	16.3349	59.984 (0.399)	-38.372	29.064		

NOTES: New molecule detections are denoted by bold font. a) Integrated line flux within  $8'' \times 12''$  synthetic beam centered on (17:10:21.263, -37:02:43.793) position. b) Hyperfine complex; representative transition frequency,  $A_{ul}$ , and upper level energy listed retrieved from CDMS.

**Table 10.** NGC 6445: DETECTED MOLECULAR TRANSITIONS

ALMA Config.	Molecule	QN	$\nu$ (GHz)	$\log A_{ul}$ (s <sup>-1</sup> )	$E_u/k$ (K)	$I^a$ ( $\sigma_I$ ) (Jy km s <sup>-1</sup> )	$V_{LSR}$ (km s <sup>-1</sup> )	$\Delta V_{1/2}$ (km s <sup>-1</sup> )
ACA	<sup>12</sup> CO	$J = 2 - 1$	230.538	-6.1605	16.5961	830.698 (1.053)	18.065	38.731
	CN	$N = 2 - 1^b$	<b>226.697</b>	<b>-4.2783</b>	<b>16.3089</b>	<b>103.930 (1.044)</b>	<b>18.217</b>	<b>39.393</b>
		$N = 2 - 1^b$	<b>226.874</b>	<b>-3.9419</b>	<b>16.3349</b>	<b>277.213 (0.931)</b>	<b>20.578</b>	<b>37.456</b>
C43-1	HNC	$J = 3 - 2$	271.981	-3.0298	26.1069	13.285 (0.819)	23.347	18.567
	<sup>12</sup> CO	$J = 2 - 1$	230.538	-6.1605	16.5961	978.148 (1.108)	21.750	44.260
	CS	$N = 5 - 4$	244.936	-3.5257	35.2660	5.953 (0.487)	14.968	29.286
	CN	$N = 2 - 1^b$	<b>226.697</b>	<b>-4.2783</b>	<b>16.3089</b>	<b>92.246 (1.047)</b>	<b>12.744</b>	<b>45.208</b>
		$N = 2 - 1^b$	<b>226.874</b>	<b>-3.9419</b>	<b>16.3349</b>	<b>222.366 (2.187)</b>	<b>32.694</b>	<b>46.824</b>
C43-4	<sup>12</sup> CO	$J = 2 - 1$	230.538	-6.1605	16.5961	396.250 (3.156)	16.048	39.680
	CN	$N = 2 - 1^b$	<b>226.697</b>	<b>-4.2783</b>	<b>16.3089</b>	<b>43.218 (2.916)</b>	<b>21.677</b>	<b>28.735</b>
		$N = 2 - 1^b$	<b>226.874</b>	<b>-3.9419</b>	<b>16.3349</b>	<b>145.479 (2.978)</b>	<b>22.716</b>	<b>34.546</b>

NOTES: New molecule detections are denoted by bold font. a) Integrated line flux within 21'' x 25'' synthetic beam centered on (17:46:16.993, -19:59:41.126) position. b) Hyperfine complex; representative transition frequency,  $A_{ul}$ , and upper level energy listed retrieved from CDMS.

**Table 11.** NGC 2899: DETECTED MOLECULAR TRANSITIONS

ALMA Config.	Molecule	QN	$\nu$ (GHz)	$\log A_{ul}$ (s <sup>-1</sup> )	$E_u/k$ (K)	$I^a$ ( $\sigma_I$ ) (Jy km s <sup>-1</sup> )	$V_{LSR}$ (km s <sup>-1</sup> )	$\Delta V_{1/2}$ (km s <sup>-1</sup> )
ACA	<sup>12</sup> CO	$J = 2 - 1$	230.538	-6.1605	16.5961	84.664 (0.322)	-15.294	14.288
	<sup>13</sup> CO	$N = 2 - 1$	<b>220.398</b>	<b>-6.2164</b>	<b>15.8662</b>	<b>23.410 (0.187)</b>	<b>-13.888</b>	<b>12.953</b>
	CN	$N = 2 - 1^b$	<b>226.697</b>	<b>-4.2783</b>	<b>16.3089</b>	<b>8.063 (0.409)</b>	<b>-4.138</b>	<b>5.813</b>
		$N = 2 - 1^b$	<b>226.874</b>	<b>-3.9419</b>	<b>16.3349</b>	<b>25.200 (0.416)</b>	<b>-7.374</b>	<b>7.104</b>
	HNC	$J = 3 - 2$	<b>265.886</b>	<b>-3.0780</b>	<b>25.5209</b>	<b>6.836 (0.302)</b>	<b>-8.018</b>	<b>4.268</b>
	HNC	$J = 3 - 2$	<b>271.981</b>	<b>-3.0298</b>	<b>26.1069</b>	<b>2.533 (0.354)</b>	<b>-7.220</b>	<b>3.499</b>
C43-4	HCO <sup>+</sup>	$J = 3 - 2$	<b>267.557</b>	<b>-2.8376</b>	<b>25.6817</b>	<b>1.115 (0.450)</b>	<b>-7.216</b>	<b>3.010</b>
	<sup>12</sup> CO	$J = 2 - 1$	230.538	-6.1605	16.5961	21.848 (0.212)	-17.996	18.732
	<sup>13</sup> CO	$N = 2 - 1$	<b>220.398</b>	<b>-6.2164</b>	<b>15.8662</b>	<b>5.831 (0.0753)</b>	<b>-17.346</b>	<b>15.941</b>
	CN	$N = 2 - 1^b$	<b>226.697</b>	<b>-4.2783</b>	<b>16.3089</b>	<b>1.326 (0.227)</b>	<b>-4.246</b>	<b>5.812</b>
		$N = 2 - 1^b$	<b>226.874</b>	<b>-3.9419</b>	<b>16.3349</b>	<b>8.361 (0.299)</b>	<b>-7.006</b>	<b>15.504</b>
C43-3	HNC	$J = 3 - 2$	<b>265.886</b>	<b>-3.0780</b>	<b>25.5209</b>	<b>3.540 (0.149)</b>	<b>-14.047</b>	<b>11.149</b>
	HCO <sup>+</sup>	$J = 3 - 2$	<b>267.557</b>	<b>-2.8376</b>	<b>25.6817</b>	<b>0.532 (0.213)</b>	<b>-14.028</b>	<b>8.754</b>

NOTES: New molecule detections are denoted by bold font. a) Integrated line flux within 15'' x 25'' synthetic beam centered on (9:25:30.467, -55:53:13.217) position. b) Hyperfine complex; representative transition frequency,  $A_{ul}$ , and upper level energy listed retrieved from CDMS.

**Table 12.** NGC 2818: DETECTED MOLECULAR TRANSITIONS

ALMA Config.	Molecule	QN	$\nu$ (GHz)	$\log A_{ul}$ (s <sup>-1</sup> )	$E_u/k$ (K)	$I^a$ ( $\sigma_I$ ) (Jy km s <sup>-1</sup> )	$V_{LSR}$ (km s <sup>-1</sup> )	$\Delta V_{1/2}$ (km s <sup>-1</sup> )
ACA	<sup>12</sup> CO	$J = 2 - 1$	230.538	-6.1605	16.5961	17.167 (0.779)	3.431	14.604
	<b><sup>13</sup>CO</b>	<b><math>N = 2 - 1</math></b>	<b>220.398</b>	<b>-6.2164</b>	<b>15.8662</b>	<b>3.466 (0.351)</b>	<b>9.942</b>	<b>9.632</b>
	CN	$N = 2 - 1^b$	226.874	-3.9419	16.3349	10.459 (0.508)	1.646	15.501
	HCN	$J = 3 - 2$	265.886	-3.0780	25.5209	3.271 (0.238)	10.356	10.186
	HNC	$J = 3 - 2$	271.981	-3.0298	26.1069	0.949 (0.208)	3.060	2.700
	HCO <sup>+</sup>	$J = 3 - 2$	267.557	-2.8376	25.6817	0.561 (0.122)	2.671	3.284
		$N = 2 - 1^b$	226.874	-3.9419	16.3349	1.609 (0.141)	1.509	19.374
C43-3	HCN	$J = 3 - 2$	265.886	-3.0780	25.5209	1.962 (0.139)	4.468	16.104
	HNC	$J = 3 - 2$	271.981	-3.0298	26.1069	2.446 (0.056)	2.242	14.017
	HCO <sup>+</sup>	$J = 3 - 2$	267.557	-2.8376	25.6817	0.778 (0.210)	-2.226	6.018
C43-4	<sup>12</sup> CO	$J = 2 - 1$	230.538	-6.1605	16.5961	5.291 (0.253)	7.004	22.859
	<b><sup>13</sup>CO</b>	<b><math>N = 2 - 1</math></b>	<b>220.398</b>	<b>-6.2164</b>	<b>15.8662</b>	<b>1.187 (0.0886)</b>	<b>4.066</b>	<b>17.270</b>
	CS	$N = 5 - 4$	244.936	-3.5257	35.2660	0.552 (0.138)	5.554	13.746
	CN	$N = 2 - 1^b$	226.697	-4.2783	16.3089	0.587 (0.113)	9.007	17.114

NOTES: New molecule detections are denoted by bold font. a) Integrated line flux within 12'' x 18'' synthetic beam centered on (9:14:00.276, -36:25:04.002) position. b) Hyperfine complex; representative transition frequency,  $A_{ul}$ , and upper level energy listed retrieved from CDMS.

## B. ALMA BAND 6 OBSERVATIONS: MOLECULAR LINE SPECTRA

Molecular emission line profiles extracted from the data cubes for the lines detected in each PN are presented in Figures 22–27. In some cases, molecular spectra have been magnified or de-magnified to fit in the same plot. Magnifications are stated next to the molecule name and transition if applicable.

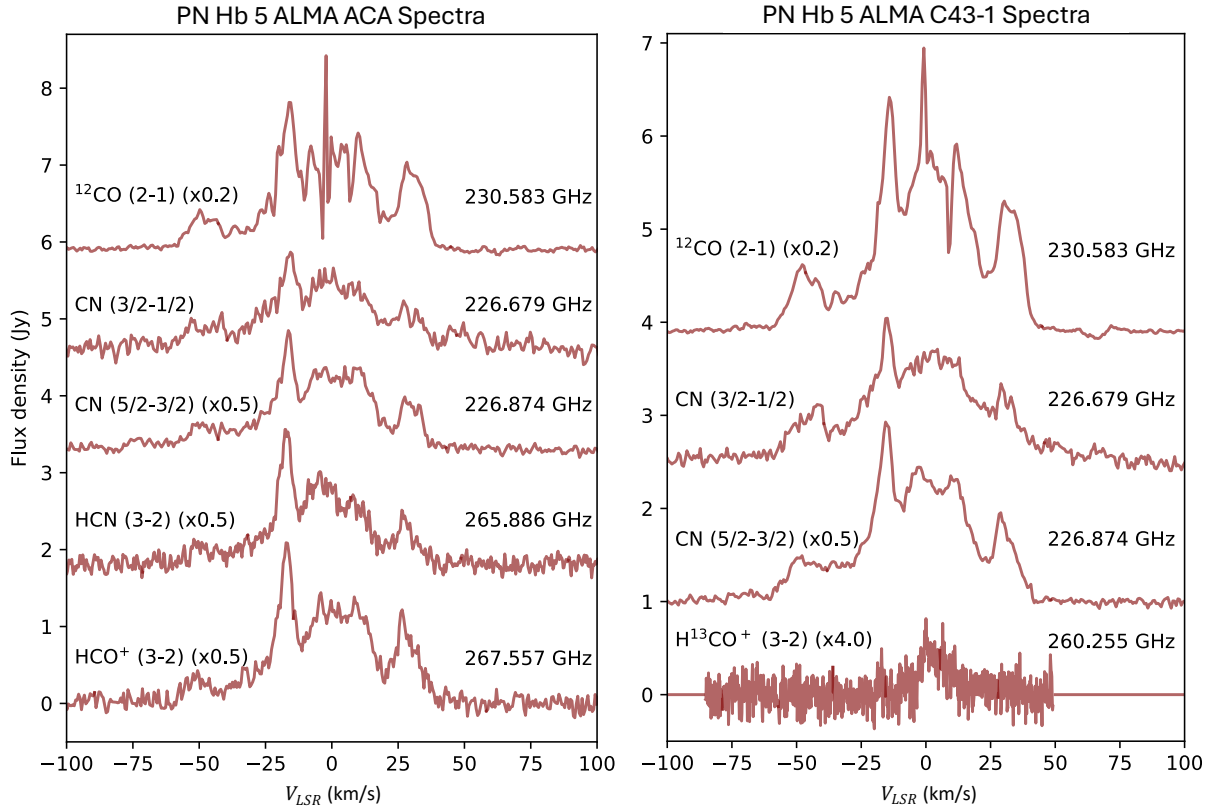


**Figure 22.** *Left panel:* spectral profiles of PN Hb 5 ALMA Band 6 ACA data. The *Right panel:* spectral profiles of PN Hb 5 ALMA Band 6 12-m data. In some cases, molecular spectra have been magnified or de-magnified to fit in the same plot. These magnifications are stated next to the molecule name and transition.

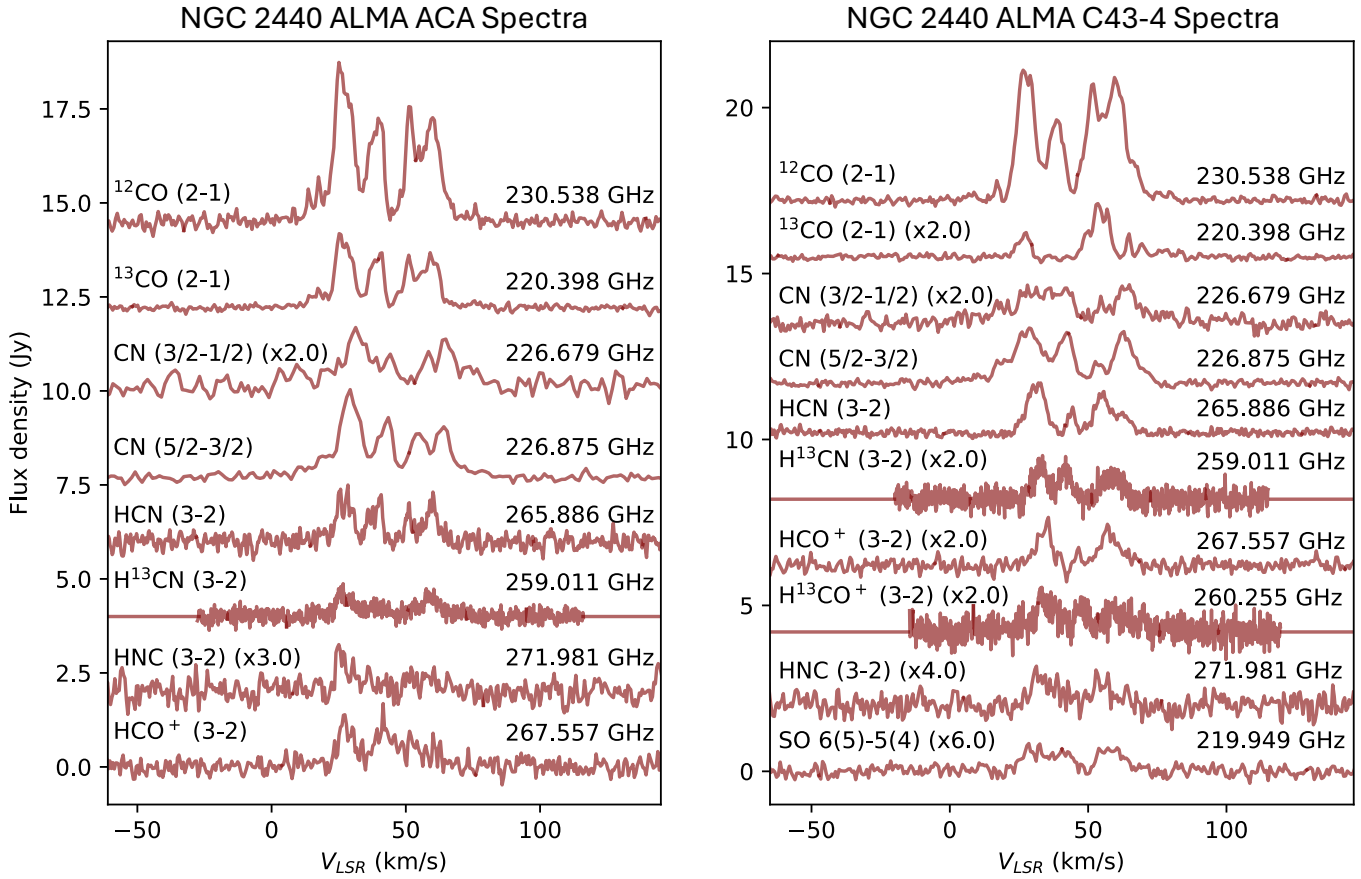


**Figure 23.** *Left panel:* spectral profiles of NGC 2440 ALMA Band 6 ACA data. The *Right panel:* spectral profiles of NGC 2440 ALMA Band 6 12-m data. Magnifications are stated next to the molecule name and transition if applicable.

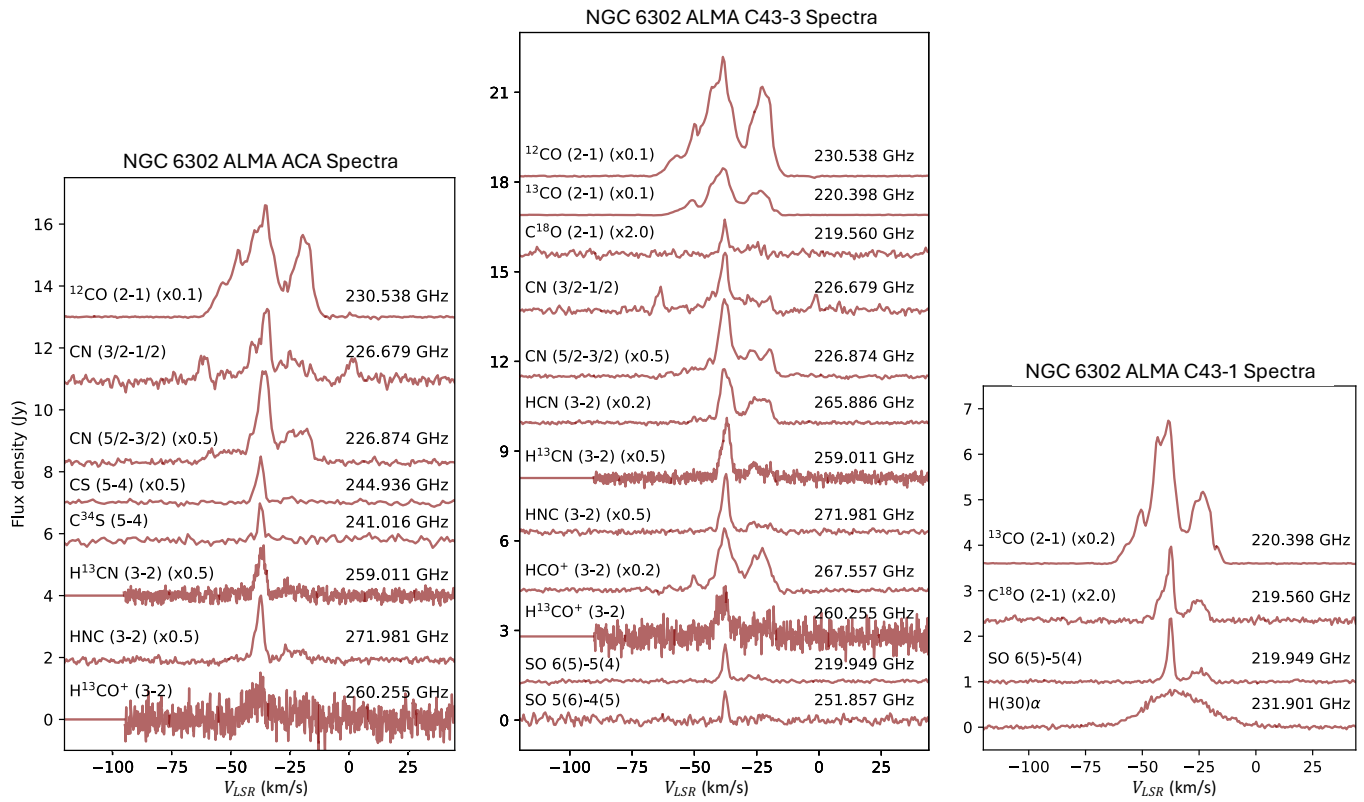


**Figure 24.** *Left panel:* spectral profiles of NGC 6302 ALMA Band 6 ACA data. *Middle panel:* spectral profiles of NGC 6302 ALMA Band 6 12-m (C43-4) data. *Right panel:* spectral profiles of NGC 6302 ALMA Band 6 12-m (C43-1) data. Magnifications are stated next to the molecule name and transition if applicable.

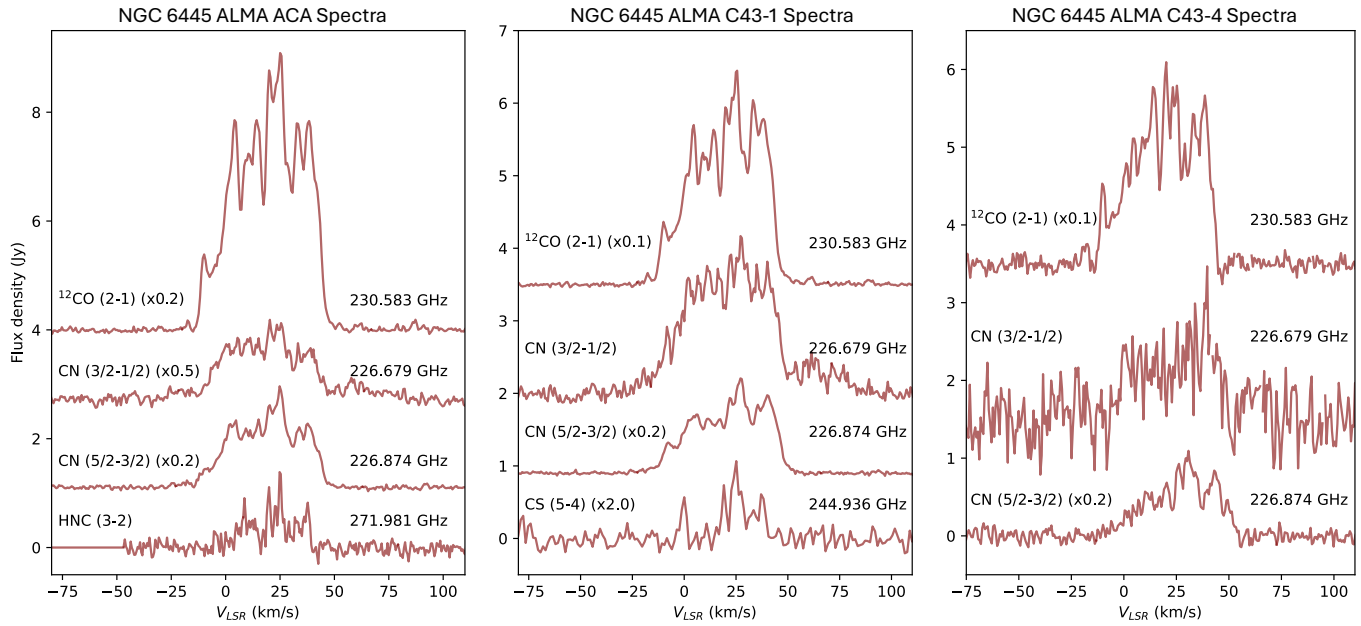


**Figure 25.** *Left panel:* spectral profiles of NGC 6445 ALMA Band 6 ACA data. *Middle panel:* spectral profiles of NGC 6445 ALMA Band 6 12-m (C43-1) data. *Right panel:* spectral profiles of NGC 6445 ALMA Band 6 12-m (C43-4) data. Magnifications are stated next to the molecule name and transition if applicable.

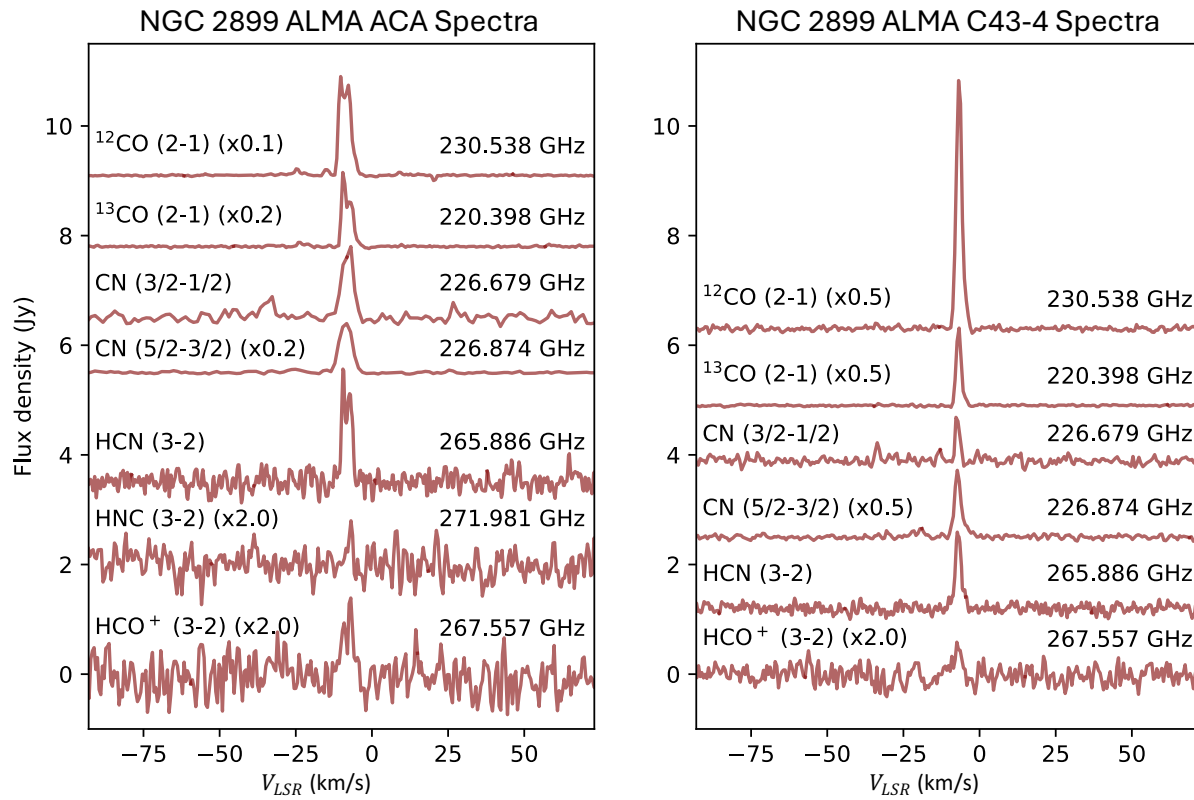


**Figure 26.** *Left panel:* spectral profiles of NGC 2899 ALMA Band 6 ACA data. *Right panel:* spectral profiles of NGC 2899 ALMA Band 6 12-m (C43-4) data. Magnifications are stated next to the molecule name and transition if applicable.

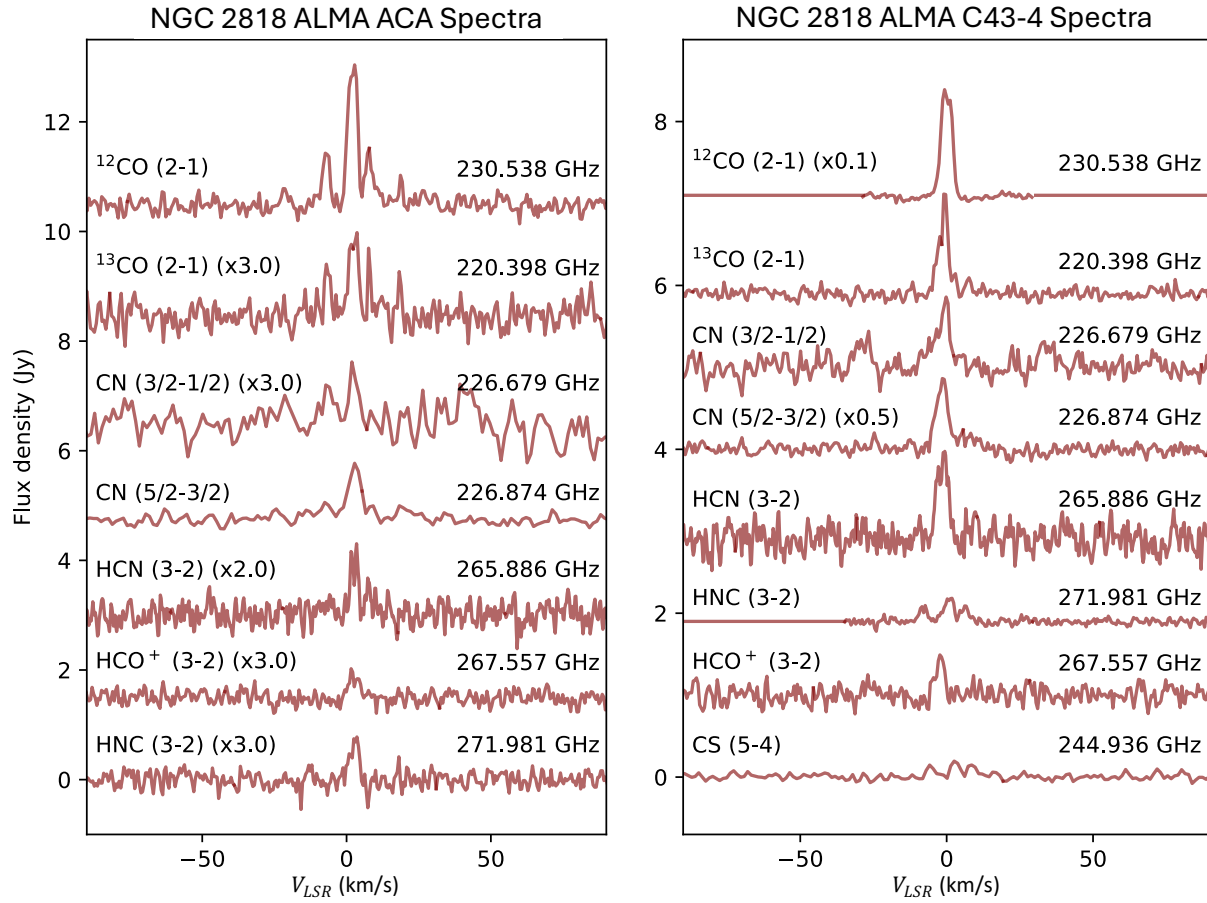


**Figure 27.** *Left panel* spectral profiles of NGC 2818 ALMA Band 6 ACA data. *Right panel* spectral profiles of NGC 2818 ALMA Band 6 12-m (C43-4) data. Magnifications are stated next to the molecule name and transition if applicable.